

**PREPARATION OF SUB-MICROMETRE THICK CuInSe_2
FILMS USING SEQUENTIAL EVAPORATION
TECHNIQUE FOR DEVICE FABRICATION**

Thesis submitted to

Cochin University of Science and Technology

in partial fulfillment of the requirements

for the award of the degree of

DOCTOR OF PHILOSOPHY

In Physics

Under the Faculty of Science

by

Deepa K G

Thin Film Photovoltaic Division
Department of Physics
Cochin University of Science and Technology
Cochin – 682 022, Kerala, India

August 2008

Preparation of sub-micrometre thick CuInSe₂ films using sequential evaporation technique for device fabrication

PhD thesis in the field of Photovoltaics

Author:

Deepa K G
Thin Film Photovoltaic Division
Department of Physics
Cochin University of Science and Technology
Cochin – 682 022, Kerala, India
email: deepakannur@yahoo.co.in

Supervising Guide:

Dr.C Sudha Kartha
Department of Physics
Cochin University of Science and Technology
Cochin – 682 022, Kerala, India
email: csk@cusat.ac.in

Cochin University of Science and Technology
Cochin-682022, Kerala, India

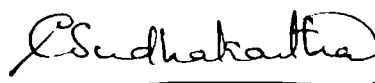
AUGUST 2008

Certificate

Certified that the work presented in this thesis entitled "*Preparation of sub-micrometre thick CuInSe₂ films using sequential evaporation technique for device fabrication*" is based on the authentic record of research done by Ms. Deepa K G under my guidance in the Department of Physics, Cochin University of Science and Technology, Cochin – 682 022 and has not been included in any other thesis submitted for the award of any degree.

Cochin-22

Date: 21/8/08



Dr. C Sudha Kartha

(Supervising Guide)

Declaration

I hereby declare that the work presented in this thesis entitled "*Preparation of sub-micrometre thick CuInSe₂ films using sequential evaporation technique for device fabrication*" is based on the original research work done by me under the supervision and guidance of *Dr.C.Sudha Kartha*, Department of Physics, Cochin University of Science and Technology, Cochin-682022 and has not been included in any other thesis submitted previously for the award of any degree.

Cochin – 22

Date: 21/08/08



Deepa K G

Acknowledgments

With great pleasure, I express my sincere gratitude to my guide, Dr C Sudha kartha for her excellent guidance, inspiration, suggestions and profuse assistance during my research work. Without her sincere help and an expert advice, I am sure my work would not have been completed. Her patience and understanding nature has been a constant encouragement during my work.

I would like to express my heartfelt thanks to Prof K P Vijayakumar for his scientific and technical advice and for helping me to better shape the thesis. I specially thank him for his competent advice, moral support and for his immeasurable help during my course work.

I am indebted to Prof Godfrey Louis, Head, Department of Physics, Prof. Ramesh Babu T and Prof V C Kuriakose former heads of Department of Physics for providing me necessary facilities.

I thank all the faculty members and office staff of the Physics department for their help and encouragement.

I would like to thank Prof. Y Kashiwaba and T Abe, Department of Electrical and Electronics Engineering, Iwate University, Japan for their invaluable experimental support. I thank Dr. Parameshwar Hari, Department of Physics and Engineering Physics, University of Tulsa, USA for his help in carrying out EDAX measurements. I would like to acknowledge The Director, Dr V Ganesan, Dr V Sathae and Dr D M Phase. UGC-DAE, CSR, Indore for their support in carrying out the measurements during the period of my stay at CSR Indore.

Funding for this research work was provided through DRDO project Scheme. I was immensely benefited by the scheme. Financial assistance provided by CUSAT is also gratefully acknowledged.

I wish to express my thanks to Dr P M Ratheesh kumar, Mr K C Wilson and Dr Teny Theresa John for helping me during the initial phase of my work. I am grateful to Dr.S Ramkumar and Dr.M Paulraj for the concern they have shown towards me. I wish to acknowledge my team: Beena, Jayakrishnan, Kishore, Sreekumar, Tina, Meril, Vimal, Anita, Pramitha, Sajeesh, Angel, Rajesh Menon, Rajesh C S, Nimmi, Sreeroop, Rajesh Gopinath, Jafar, Poornima, Subramanyan, Subin and Dhanya for many fruitful discussions and lively moments that I will ever treasure in my life.

I humbly lean my head towards all my teachers who helped me to learn the fundamentals and guided me to achieve this target.

Last but not least, I remember my family and friends who make my life so lovely and meaningful and **I dedicate my work to them...**

Deepa K G

Preface

The mass consumption of fossil fuels, which are getting depleted and also causing pollution, has led to the development of new source of energy called 'Photovoltaic'. Conversion of sunlight directly into electricity using photovoltaic technique of suitable materials is the most elegant energy conversion process. Solar cell technology had undergone enormous development during the last three decades, initially in providing electrical power for spacecraft, and more recently, for terrestrial applications. Cheap but low-grade solar energy may be converted to other forms of higher-grade energy through one of several methods, such as photothermal, photochemical, photoelectrochemical, photobiochemical and photovoltaic. Among these, the cleanest, most direct and efficient mode of conversion to electrical power is photovoltaic (PV) using solar cell devices.

The most widely used solar cells are based on the Silicon technology. However, there are many draw backs for this, leading to considerable cost escalation. Hence with the idea of fabricating cheaper solar cells, thin film technology has emerged. Among the candidates for thin film solar cells, CuInSe_2 is known to be the ideal one as the absorber layer. CuInSe_2 -based solar cells require less semiconductor material and are potentially lighter and thinner than Silicon Solar Cells. No evidence for long or short term device degradation was observed (as in a-Si solar cells) in the case of CuInSe_2 based solar cells. Thin film solar cells, made from Copper Indium Gallium Diselenide (CIGS) absorbers, exhibited great promise in achieving high conversion efficiencies (approaching 20%) and these devices were fabricated using co-evaporation techniques. CuInSe_2 has now entered into the market and the efficiency of CuInSe_2 module has reached 13.4%.

The key issues in the field of CuInSe_2 solar cells are developing simpler techniques for CuInSe_2 preparation, reduction of thickness of absorber layer and replacement of CdS with non-toxic buffer layer. The present work was focusing on these issues.

In this work, sub-micrometre thick CuInSe_2 films were prepared using two different techniques. In the first case, chemical bath deposited Selenium was used and

in the second case, vacuum evaporated Se was used for selenization. These methods are simpler than co-evaporation technique, which is known to be the most suitable one for CuInSe_2 preparation. The films were optimized by varying the composition over a wide range to find optimum properties for device fabrication. Typical absorber layer thickness of today's solar cell ranges from 2-3 μm . Thinning of the absorber layer is one of the challenges to reduce the processing time and material usage, particularly of Indium. Here we made an attempt to fabricate solar cell with absorber layer of thickness $<1\mu\text{m}$. Here In_2S_3 was used as the buffer layer, replacing toxic CdS.

CHAPTER 1 gives general introduction to photovoltaics with a sketch of three generations of developments in the field of solar cells. Working principle of a p-n junction and brief discussion on the materials for photovoltaics is included in this chapter. An exhaustive review on CuInSe_2 thin films is also included here.

CHAPTER 2 specifies the theory as well as experimental setup used for the sample preparation. Details of the characterization techniques used in the present work are also given in this chapter.

CHAPTER 3 focusses on, preparation and characterization of CuInSe_2 thin films from chemical bath deposited Selenium. CuInSe_2 films were deposited using two techniques, viz, stacked elemental layer technique and thermal diffusion of Cu into In_2Se_3 . Structural, compositional, optical and electrical characterizations of the films were carried out with the help of X-Ray Diffraction (XRD), Raman spectroscopy, X-ray Photoelectron Spectroscopy (XPS), Energy Dispersive X-ray Analysis (EDAX), resistivity, photosensitivity, optical absorption and transmission. Surface analysis was done using Atomic Force Microscopy (AFM). Comparison between the two methods was performed and best samples were selected for trial on device fabrication. Even though the films prepared using the two techniques showed similar variation in crystallinity, grain size and band gap with Cu to In ratio, the photosensitivity was found to be higher for those samples prepared using thermal diffusion of Cu into In_2Se_3 . Hence this was considered to be suitable for solar cell applications. The films had good crystallinity with sphalerite structure as confirmed from XRD and Raman studies. Information on stoichiometry of the samples was obtained from EDAX

measurements. These CuInSe_2 films were free from voids and pinholes. Defect analysis was also performed using photoluminescence and temperature dependant conductivity studies.

The main advantage of this technique was that, highly toxic Se vapor or H_2Se gas could be completely avoided. An attempt to device fabrication was also made using vacuum evaporated CdS as buffer layer. But photovoltaic effect could not be observed at the junction. Even though this preparation technique was eco-friendly, it had the disadvantage that, thickness of Se layer was only $0.25\mu\text{m}$. The problems with this lower thickness are reduced absorption of incoming photons and also increased back surface recombination. As techniques like light trapping and back reflectors were not employed in this configuration, slightly increased thickness ($0.5\text{-}1\mu\text{m}$) should be used. In this technique, the overall absorber layer thickness was lower for getting considerable absorption of the photons. Unfortunately the thickness of the absorber layer could not be increased further so as to increase the absorption.

A modified technique of vacuum evaporation was introduced in **CHAPTER 4**, in which CuInSe_2 thin films were prepared using sequential elemental evaporation. In this technique Cu, In and Se were evaporated at moderately low substrate temperatures as an alternative to higher temperature deposition and co-evaporation. This method is simpler and more economically viable than co-evaporation. Moreover control of stoichiometry could easily be achieved. Composition was widely varied to find the suitability in device fabrication. For this, Cu and Se were varied, one at a time, keeping the others constant. Both p- and n-type films could be prepared using this technique. From the structural characterization using XRD and Raman scattering, structure of CuInSe_2 prepared using this method, was identified as “chalcopyrite” which is the most suitable and favourable structure for solar cells. In the earlier method of preparing CuInSe_2 (using chemical bath deposited Se), we could obtain only “sphalerite” structure. The grain size varied from 35 nm to 63 nm in these samples. However this grain size was still lower than the reported values, obtained through other techniques. This lead to increase in the number of grain boundaries which, in some cases, has beneficial effects on CuInSe_2 devices. Interestingly, the crystallinity of these samples was better than that of earlier

samples prepared using chemical bath deposited Se. Again grain size was three times larger than that of the samples prepared using CBD Se.

Band gap varied from 0.93 to 0.99 eV in the samples with variation in elemental concentrations. AFM analysis of the sample showed that geometry of the sample changed from spherical to pyramidal on going from In-rich to Cu-rich. Resistivity varied in the range of 0.002 Ωcm to 7916 Ωcm and hence highly conductive or highly resistive samples could be selected for device fabrication. Sample with resistivity of 0.08 Ωcm can be used as conductive bottom layer and sample with resistivity of 7916 Ωcm can be used as the resistive top layer of device. Photosensitivity of the highly resistive sample was 7.7. Highly stoichiometric film could also be prepared without using ultra high vacuum which is still a major challenge for many researchers working in ternary chalcopyrites. Typical concentration of the stoichiometric sample was Cu: 24.92%, In: 24.98% and Se 50.10%.

CHAPTER 5 describes the attempt for device fabrication using optimized samples. For this In_2S_3 prepared by Chemical Spray Pyrolysis was used as the buffer layer. This is a new buffer layer for CuInSe_2 . CuInSe_2 layer (absorber) had a double layer structure with a highly conductive (p^+) bottom layer and a resistive (p) top layer. Total layer thickness was 0.85 μm . Here the bottom layer acted as an “electron reflector”, thereby reducing back surface recombination. The junction characteristics were studied by varying thickness, In/S ratio and post deposition treatments of In_2S_3 . We could observe only a feeble photovoltaic effect which may be improved by varying further parameters. As a trial of reduction of the absorber layer thickness and replacement of CdS, which remain as a challenge in the development of CuInSe_2 solar cells, in the present study, these two factors were taken into account. In_2S_3 seems to be a good buffer layer instead of CdS for CuInSe_2 solar cells.

CHAPTER 6 is the summary of the entire work. Important points are also included and the future scope of the work is added.

Publications in peer reviewed journals

1. Thermal Diffusion of Cu into In_2Se_3 : A better approach to SEL technique in the fabrication of CuInSe_2 Thin Films: K.G.Deepa, P.M.Ratheesh Kumar, C.Sudha Kartha, K.P.Vijayakumar - Solar Energy Materials and Solar Cells 90 (2006) 3481 – 3490
2. Tuning donor-acceptor and free-bound transitions in CuInSe_2 /Indium Tin Oxide heterostructure: R. Jayakrishnan, K.G.Deepa, C. Sudha Kartha, K. P. Vijayakumar - J. Appl. Phys. 100 (2006) 046104
3. Sub-Micrometre Thick CuInSe_2 Films for Solar Cells Using Sequential Elemental Evaporation: K.G.Deepa, R. Jayakrishnan, K. P. Vijayakumar, C. Sudha kartha, V. Ganesan, (Communicated)
4. Vibrational modes in Sequentially evaporated CuInSe_2 thin films: K G Deepa, V Sathae, C Sudha Kartha, K P Vijayakumar (to be communicated)

Conference Presentations

1. Effect of In Variation in Sequentially Evaporated CuInSe_2 Thin Films: K G Deepa, K P Vijayakumar and C Sudha kartha, International Conference on Solar Cells, IC SOLACE 2008, at Cochin University of Science & Technology, Cochin, 21-23rd Jan 2008
2. Sequentially Evaporated CuInSe_2 Thin Films For Solar Cells: K.G.Deepa, R.Jayakrishnan, V.Sathae, K.P.Vijayakumar, C.Sudha Kartha (22nd European photovoltaic solar energy conference and exhibition(22nd EUPVSEC), Milan, Italy, 3-7th Sept 2007
3. Structural and Electrical Characteristics of Sequentially Evaporated CuInSe_2 Thin Films: K.G.Deepa, C.Sudha Kartha and K.P.Vijayakumar - National Conference on Current Trends in Material Science, Christian College, Chengannur, March 25-27th, 2007.
4. Bilayer CuInSe_2 thin films for solar Cells using Vacuum Evaporation Technique: K.G.Deepa, K.P.Vijayakumar, C.Sudha Kartha - National Conference on SMART materials and recent technologies, S.V.University, Tirupati. Feb.22-23rd, 2007.
5. Raman analysis of Sequentially Evaporated CuInSe_2 Thin Films: K.G.Deepa, R.Jayakrishnan, V.Sathae, D.M.Phase, K.P.Vijayakumar, C.Sudhakartha -

18th Annual General Meeting, Material Research Society of India, National Physical Laboratory, Delhi Feb 12-14th, 2007.

6. p-type and n-type CuInSe₂ thin films by sequential elemental evaporation: K.G.Deepa, K. P.Vijayakumar, C.Sudha Kartha, D.M.Phase, V.K.Ahire - 17th Annual General Meeting, Material Research Society of India, University of Lucknow, Lucknow, Feb 13-15th, 2006
7. Modified Technique for Deposition of CuInSe₂ Thin Films Using Elemental Evaporation: K.G.Deepa, P.M.Ratheesh Kumar, K.P.Vijayakumar, C.Sudha Kartha, D.M.Phase, V.K.Ahire - MRSI Discussion meeting on 'Materials for future Energy', Bhabha Atomic Research Centre, Mumbai, Jan 18-19th, 2006
8. Optimization of Cu/In ratio for device quality CuInSe₂ thin films prepared using Stacked Elemental Layer (SEL) technique: K.G.Deepa, K.P.Vijayakumar, C.Sudha Kartha - 16th Annual General Meeting, Material Research Society of India, National Chemical Laboratory, Pune, Feb 10-12th, 2005

Contents

1. Photovoltaics: Energy for the next generation.....	1
1.1. Introduction.....	1
1.2. Discovery of photovoltaic effect	3
1.3. First solar cells.....	3
1.4. Theory of solar cell.....	3
1.5. Connection to an external load.....	5
1.6. Equivalent circuit of a solar cell.....	5
1.7. Solar cell efficiency factors.....	6
1.7.1. Maximum-power point.....	6
1.7.2. Energy conversion efficiency.....	7
1.7.3. Fill factor.....	7
1.7.4. Quantum efficiency.....	8
1.7.5. Comparison of energy conversion efficiencies.....	8
1.7.6. Peak watt	9
1.8. Solar cells and energy payback.....	9
1.9. Three generations of development.....	9
1.9.1. First.....	9
1.9.2. Second.....	10
1.9.3. Third.....	10
1.10. Current stage of development.....	10
1.11. Important material properties for high efficiency cell.....	12
1.12. Materials for photovoltaic.....	13
1.12.1. Crystalline silicon.....	13
1.12.2. Amorphous Silicon.....	13
1.12.3. Gallium Arsenide.....	14
1.12.4. Indium Phosphide.....	15
1.12.5. Cadmium Telluride.....	15
1.12.6. CuInS_2	15
1.12.7. CuInSe_2 (CIS).....	16

1.13.Properties of CIS.....	16
1.13.1. Tetragonal chalcopyrite structure.....	16
1.13.2. Band gap of 1eV at room temperature.....	17
1.13.3. High absorption co-efficient of 10^5cm^{-1}	17
1.13.4. Large structural tolerance to off-stoichiometry.....	17
1.13.5. Excellent stability and high radiation resistance.....	18
1.13.6. Fabrication on variety of substrates.....	18
1.14.Mile stones in the development of CIS based solar cells.....	18
1.15.Review on CIS thin films.....	19
1.15.1. Vacuum processes.....	19
1.15.2. Non-vacuum processes.....	28
1.15.3. Defect studies.....	36
1.15.4. Effects of Na and O.....	40
References.....	43
2. Theory and Experimental Techniques.....	50
2.1. Techniques for CuInSe_2 (CIS) preparation.....	50
2.1.1. Chemical Bath Deposition (CBD).....	52
2.1.2. Vacuum evaporation	53
2.2. Technique for deposition of In_2S_3 films.....	55
2.3. Sample preparation.....	56
2.3.1. Cleaning of substrates.....	56
2.3.2. Deposition of CIS films using CBD Se layer.....	56
2.3.3. CIS using sequential evaporation of elemental layers.....	59
2.3.4. In_2S_3 using Chemical Spray Pyrolysis.....	59
2.4. Characterization techniques Used.....	60
2.4.1. X-Ray Diffraction (XRD).....	60
2.4.2. Raman Scattering.....	61
2.4.3. Optical absorption studies.....	63
2.4.4. Stylus profilometer.....	64
2.4.5. Photoluminescence (PL).....	65

2.4.6.	Energy Dispersive Analysis using X-rays (EDAX).....	67
2.4.7.	Atomic Force Microscopy (AFM).....	68
2.4.8.	X-ray Photoelectron Spectroscopy (XPS).....	69
2.4.9.	Electrical Characterization.....	70
	References.....	74
3.	CuInSe₂ thin films using Chemical Bath Deposited Selenium.....	76
3.1.	Introduction.....	76
3.2.	Experimental details.....	77
3.3.	Structural characterization.....	78
3.4.	Optical characterization.....	84
3.5.	Electrical characterization.....	86
3.6.	Observations.....	87
3.7.	Compositional analysis.....	88
3.8.	Structural analysis.....	89
3.9.	Raman analysis.....	91
3.10.	AFM analysis.....	93
3.11.	Photoluminescence studies.....	95
3.12.	Temperature dependant conductivity.....	99
3.13.	Characteristics of optimized CdS thin film for solar cell fabrication...	103
3.14.	Device fabrication: Trial	104
3.15.	Conclusion.....	105
	References.....	106
4.	Modified technique for deposition of CuInSe₂ thin films using sequential elemental evaporation and characterizations.....	109
4.1.	Introduction.....	109
4.2.	Experimental details.....	111
4.3.	Optimization of deposition process.....	111
4.4.	Characterization of optimized sample.....	116
4.4.1.	EDAX analysis.....	116

4.4.2.	XPS analysis.....	117
4.4.3.	Thickness measurement.....	119
4.4.4.	Optical absorption.....	119
4.4.5.	Electrical characterization.....	121
4.4.6.	Temperature dependant conductivity measurements.....	121
4.4.7.	Morphological analysis.....	122
4.4.8.	Inference.....	123
4.5.	Effect of variation of Cu.....	124
4.5.1.	Structural characterization.....	124
4.5.2.	Thickness measurements.....	126
4.5.3.	EDAX measurements.....	127
4.5.4.	Optical absorption.....	129
4.5.5.	Electrical characterization.....	130
4.5.6.	Morphological analysis.....	131
4.5.7.	PL measurement.....	132
4.6.	Effect of variation of In concentration.....	136
4.6.1.	Structural Characterization.....	137
4.6.2.	EDAX measurements.....	138
4.6.3.	Optical Absorption.....	138
4.6.4.	Electrical Characterization.....	139
4.6.5.	Discussion.....	140
4.7.	Minute variations of Cu and In concentrations.....	140
4.8.	Optimization for solar cell fabrication.....	141
4.8.1.	Structural Characterization.....	141
4.8.2.	Compositional analysis.....	146
4.8.3.	Optical characterization.....	149
4.8.4.	Electrical characterization.....	150
4.8.5.	Discussion.....	151
4.9.	Variation of Se concentration.....	151
4.9.1.	Structural Characterization.....	151
4.9.2.	EDAX measurements.....	152
4.9.3.	Optical characterization.....	153

4.9.4. Electrical characterization.....	154
4.10. Stoichiometric CuInSe ₂ films.....	155
4.11. Double layer CuInSe ₂	157
4.12. Conclusions.....	159
References.....	161
5. Fabrication of CuInSe₂/In₂S₃ junction.....	163
5.1. Introduction.....	163
5.2. Review of research work on CuInSe ₂ based solar cells.....	163
5.3. Experimental.....	169
5.4. Layer properties for the device fabrication.....	170
5.4.1. Bottom electrode.....	170
5.4.2. Absorber layer.....	171
5.4.3. Buffer layer.....	172
5.4.4. Top electrode.....	173
5.5. Structure of the cell.....	173
5.6. Variations on window layer.....	174
5.6.1. Effect of thickness of the buffer layer.....	174
5.6.2. Effect of variation in In/S ratio.....	180
5.7. In ₂ S ₃ in the ratio 1.2/8 on ITO.....	183
5.8. Variation in the absorber layer.....	185
5.8.1. Junction with Stoichiometric CIS.....	185
5.8.2. Junction with single layer CIS.....	186
5.9. Effect of post deposition annealing.....	186
5.10. Conclusions.....	188
References.....	189
6. Summary and Conclusions.....	192

Photovoltaics: Energy for the Next Generation

1.1 Introduction

Development of clean energy sources has become the most important task assigned to the science and technology in the 21st century and photovoltaics has emerged as the most promising candidate of the future energy technology. The importance of alternative energy sources has increased in significance both for energy supply and ecological conservation reasons. In spite of limitations due to short-term economic considerations, research and development of photovoltaic solar cell has increased and is playing an increasingly practical role all over the world. The industrial revolution started with coal as the main energy source, and later, it was shifted to oil and gas (LPG, LNG), owing to the mass-production technology, ease of transport as well as storage and also the [less] environmental issues in comparison with the coal. Today, electrical energy is identified as the most convenient form of energy and it is non-pollutant also. Everyday the Sun supplies energy to the Earth, which is several thousand times our requirement. The quantity of energy supplied by the Sun is more than five orders of magnitude larger than the present requirement of electric power for the whole world, to keep modern civilization going. Above all, solar photovoltaic power generation is almost maintenance free as well as clean technology.

The data given below (table 1.1) demonstrates the contributions to the global environmental issues by photovoltaics.

Table 1.1: Contributions to the global environmental issues by Photovoltaics

Local	(1) Solar PV power generation	Clean sustainable energy sources
↑	(2) Cleaning of polluted air	Ashing of pollutant gases by glow discharge
	(3) Cleaning of water	Electrochemical processing by PV
Environment	(4) Generation of Hydrogen	Electrolysis of water by PV
↓	(5) Stopping desertification	PV water pumping at plantations
	Global	and
	(6) Greening of deserts	

Table 1.2: Pollutant emission factors for different energy sources

Energy Source	CO ₂	NO ₂	SO ₂
Coal	322.8	1.8	3.400
Oil	258.5	0.88	1.7
Natural gas	178	0.9	0.001
Nuclear	7.8	0.003	0.030
Photovoltaic	5.3	0.007	0.020
Biomass	0.0	0.6	0.140
Geothermal	51.5	Trace	Trace
Wind	6.7	Trace	Trace
Solar thermal	3.3	Trace	Trace
Hydropower	5.9	Trace	Trace

Coal, oil and natural gas were/are still continuing to be the main sources of energy. From table 1.2, it is clear that Photovoltaics is a clean energy source.¹ However, a large barrier impeding the expansion of the photovoltaic systems as a large scale power source has been the high cost of the modules. One of the solutions for the cost reduction is the

development of thin film solar cell, saving both material and energy in the production of cells and modules.

1.2 Discovery of photovoltaic effect

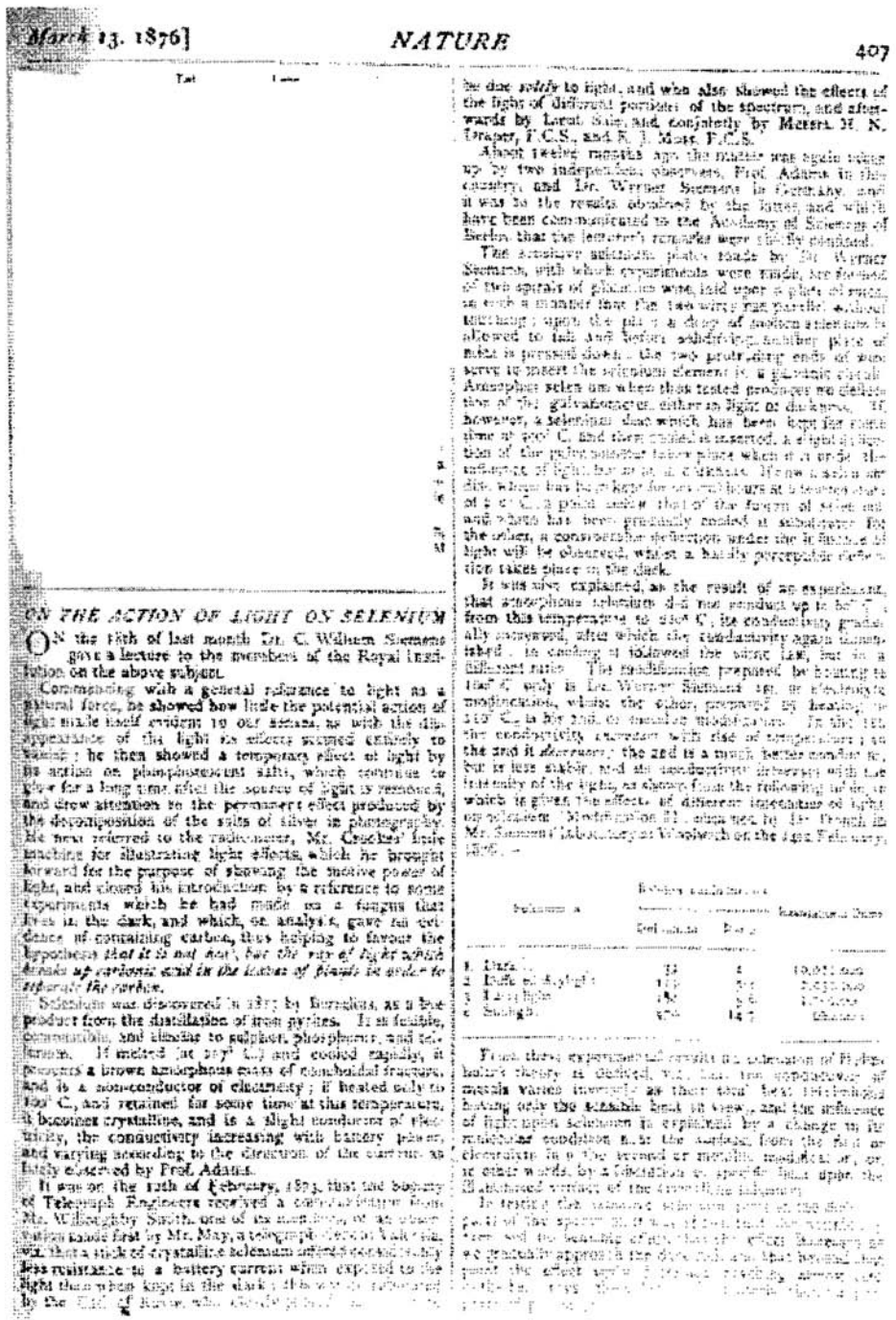
A physical phenomenon allowing light-electricity conversion - photovoltaic effect, was discovered in 1839 by the French physicist *Alexandre Edmond Becquerel*. Experimenting with metal electrodes and electrolyte he discovered that conductance rises with illumination.

1.3 First solar cells

Willoughby Smith discovered photovoltaic effect in Selenium in 1873 (fig 1.1). Later in 1876, with his student R. E. Day, William G. Adams discovered that illuminating a junction between Selenium and Platinum also has a photovoltaic effect. These two discoveries became the foundation for the first Selenium solar cell construction in 1877.

1.4 Theory of solar cell

The p-n junction is the classical model of a solar cell. This junction is created by doping different regions of the same semiconductor differently, so that there forms an interface between p type and n type layers of the same material. Since the work function of the p-type material is larger than the n type, the electrostatic potential must be smaller on the n side than p, and an electric field is established at the junction. Light absorption generates equal numbers of non-equilibrium electron-hole pairs, in concentrations much higher than equilibrium minority-carrier levels, but typically less than the equilibrium majority carrier concentrations. It is these non-equilibrium minority carriers and their potential energy changes that transform the absorbed photon energy into a DC voltage to drive DC current through the metal contacts for power delivery to an external electrical load. It is the majority carriers that finally flow through the two metal contacts to an external circuit. The junction region is always depleted of both electrons and holes and presents a barrier to majority carriers, and a low resistance path to minority carriers. It drives the collection of minority carriers which are photogenerated throughout the p and n layers, and reach the junction by diffusion.



March 13, 1876]

NATURE

407

ON THE ACTION OF LIGHT ON SELENIUM

ON the 13th of last month Dr. C. Wilhelm Siemens gave a lecture to the members of the Royal Institution on the above subject.

Commencing with a general reference to light as a natural force, he showed how inside the potential action of light made itself evident to our senses, as with the disappearance of the light its effects ceased entirely to manifest; he then showed a temporary effect of light by its action on phosphorescent salts, which continue to glow for a long time after the source of light is removed, and drew attention to the permanent effect produced by the decomposition of the salts of silver in photography. He next referred to the radium-rays, Mr. Crookes' little machine for illustrating light effects, which he brought forward for the purpose of showing the motive power of light, and closed his introduction by a reference to some experiments which he had made on a fungus that lives in the dark, and which, on analysis, gave no evidence of containing carbon, thus helping to favour the hypothesis that it is not dead, but the rays of light which break up carbonic acid in the tissues of plants in order to separate the carbon.

Selenium was discovered in 1817 by Berzelius, as a by-product from the distillation of iron pyrites. It is fusible, combustible, and soluble in sulphur, phosphorus, and tellurium. If melted at 257°C and cooled rapidly, it becomes a brown amorphous mass of non-crystalline fracture, and is a non-conductor of electricity; if heated only to 100°C, and retained for some time at this temperature, it becomes crystalline, and is a slight conductor of electricity, the conductivity increasing with battery power, and varying according to the direction of the current, as lately observed by Prof. Adams.

It was on the 12th of February, 1873, that the Society of Telegraph Engineers received a communication from Mr. William Siemens, one of its members, of an observation made first by Mr. May, a telegraphic operator at Viena, viz. that a stick of crystalline selenium offered considerably less resistance to a battery current when exposed to the light than when kept in the dark; this was afterwards confirmed by the Earl of Russell, who accordingly prepared a series of

be due solely to light, and who also showed the effects of the light of different portions of the spectrum, and afterwards by Lucat, Salin, and conjointly by Messrs. H. N. Fowler, F.C.S., and R. J. Meiss, F.C.S.

About twelve months ago the matter was again taken up by two independent observers, Prof. Adams in this country, and Dr. Werner Siemens in Germany, and it was to the results obtained by the latter and which have been communicated to the Academy of Sciences of Berlin, that the lecturer's remarks were chiefly confined.

The sensitive selenium plates made by Dr. Werner Siemens, with which experiments were made, are formed of two spirals of platinum wire laid upon a plate of selen, in such a manner that the two wires run parallel without touching upon the plate, a drop of molten selenium is allowed to fall and before solidifying another plate of selen is pressed down, the two protruding ends of wire serve to insert the selenium element in a galvanic circuit. Amorphous selenium when thus tested produces no deflection of the galvanometer, either in light or darkness. If, however, a selenium disc which has been kept for some time at 100°C, and then cooled as aforesaid, a slight deflection of the galvanometer takes place when it is exposed to the influence of light, but not in darkness. If now a selen or disc, which has been kept for several hours at a temperature of 100°C, is placed under that of the form of selen and photo has been gradually cooled it subsequently to the other, a considerable deflection under the influence of light will be observed, whilst a hardly perceptible deflection takes place in the dark.

It was also explained, as the result of an experiment, that amorphous selenium did not conduct up to 100°C, from this temperature to 250°C, its conductivity gradually increased, after which the conductivity again diminished, in cooling it followed the same law, but in a different ratio. The modification prepared by heating to 100°C only is Dr. Werner Siemens' so-called electrolytic modification, whilst the other prepared by heating to 250°C is his so-called metallic modification. In the first the conductivity increases with rise of temperature up to the end it decreases; the second is a much better conductor, but is less stable, and its conductivity decreases with the intensity of the light, as shown from the following table, in which is given the effect of different intensities of light on selenium. Modification II, announced by Dr. Frank in Mr. Siemens' laboratory at Woolwich on the 22nd February, 1876.

Selenium II	Battery resistance at		Resistance in Ohms
	Darkness	Light	
a. Dark	15	4	10,000 ohms
b. Half of daylight	115	50	2,000 ohms
c. Full daylight	140	50	1,500 ohms
d. Sunlight	250	14.7	Ohms

From these experimental results the extension of Helmholtz's theory is deduced, viz. that the appearance of metals varies inversely as their total heat, Helmholtz having only the sensible heat in view, and the influence of light upon selenium is explained by a change in its resistance condition due to the escape from the heat or electricity in a the second or metallic modification, or, in other words, by a substitution of specific heat upon the diminished contact of the crystalline selenium.

In testing the various selenium plates of the different parts of the spectrum it was found that the maximum effect was produced by the red light, and that the effect of the blue light was so gradually approached the dark red, and that beyond this point the effect was a further reaching amount, and that the rays which were most abundant in the spectrum produced the greatest effect.

Fig 1.1: Article published in nature 1876 by Smith after the discovery of photovoltaic action in Selenium

In a semiconductor, the effective field, existing between the two semiconductors [for separation of carriers] can be generated under the conditions of

- (i) gradient in the vacuum level or work function
- (ii) gradient in the electron affinity
- (iii) gradient in the band gap
- (iv) gradient in the band densities of states

The first three of these are exploited in photovoltaic devices and changes in these three can be achieved at the interface between two different materials (heterojunction) or through gradual changes in the composition of an alloy.^{2,3}

1.5 Connection to an external load

Ohmic metal-semiconductor contacts are made to both the n-type and p-type sides of the solar cell, and the electrodes are connected to an external load. Electrons that are created in the n-type side, or have been collected by the junction and swept onto the n-type side, may travel through the wire, power the load, and continue through the wire until they reach the p-type semiconductor-metal contact. Here, they recombine with a hole that was either created as an electron-hole pair on the p-type side of the solar cell, or swept across the junction from the n-type side after being created there.

1.6 Equivalent circuit of a solar cell

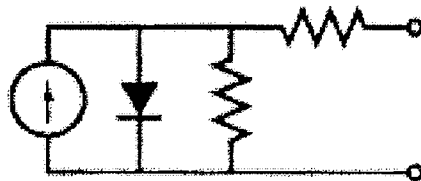


Fig 1.2: Equivalent circuit of a solar cell

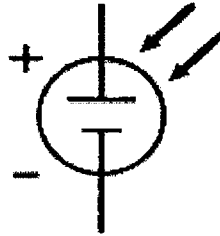


Fig 1.3: Schematic symbol of a solar cell

An ideal solar cell may be modelled as a current source in parallel with a diode. In practice, no solar cell is ideal, and hence, shunt resistance and series resistance components are added to the model. The result is the "equivalent circuit of a solar cell" shown in fig1.2. Also shown (fig1.3) is the schematic representation of a solar cell for use in circuit diagrams.

1.7 Solar cell efficiency factors

1.7.1 Maximum-power point

A solar cell may operate over a wide range of voltage (V) and current (I). By increasing the resistive load on an irradiated cell continuously from zero (short circuit condition) to a very high value (open circuit condition) one can determine the maximum-power point, i.e., the load for which the cell can deliver maximum electrical power at that level of irradiation, $V_m \times I_m = P_m$ in watts.

The quickest way to determine the optimal load for a given constant light condition (i.e. a stable quiescent point) is to measure the "Thevenin Equivalent Voltage" (i.e. open circuit), then using a potentiometer as a load, monitor the voltage across it. When the load voltage is exactly half of the Thevenin equivalent Voltage, disconnect the potentiometer and measure its resistance. By the maximum power theorem, the potentiometer resistance will be the optimal value of the load for maximum power transfer (due to the equal voltage division between internal Thevenin equivalent Resistance and the load).

The maximum power point of a solar cell varies with incident illumination. For systems large enough to justify the extra expense (say, ~1 kiloWatt), a 'power point tracker'

tracks the instantaneous power by continually measuring the voltage and current (and hence, power transfer), and uses this information to dynamically adjust the load so that the maximum power is always transferred, regardless of the variation in irradiation. A photovoltaic device optimally runs at 50% electrical efficiency (the point of maximum power transfer), as it is a now-or-never energy source.

1.7.2 Energy conversion efficiency

The energy conversion efficiency (η) of a solar cell is the percentage of power converted (from absorbed light to electrical energy) and collected, when a solar cell is connected to an electrical circuit. This term is calculated using the ratio of P_m , divided by the input light irradiance under "standard" test conditions (E , in W/m^2) and the surface area of the solar cell (A_c in m^2).

$$\eta = \frac{P_m}{E \times A_c}$$

At solar noon, on a clear March or September equinox day, the solar radiation at the equator is about $1000 W/m^2$. Hence, the "standard" solar radiation [known as the "air mass 1.5 spectrum (AM 1.5)"] has a power density of 1000 watts per square metre. Thus, a 12% efficiency solar cell having $1 m^2$ of surface area in full sunlight at solar noon at the equator during either the March or September equinox will produce approximately 120 watts of peak power.

1.7.3 Fill factor (FF)

Another defining term in the overall behaviour of a solar cell is the 'Fill Factor (FF)'. This is obtained by dividing the maximum power point by the product of open circuit voltage (V_{oc}) and the short circuit current (I_{sc}):

$$FF = \frac{P_m}{V_{oc} \times I_{sc}} = \frac{\eta \times A_c \times E}{V_{oc} \times I_{sc}}$$

1.7.4 Quantum efficiency (QE)

'Quantum efficiency [QE]' refers to the percentage of absorbed photons that produce electron-hole pairs (or charge carriers). External QE includes the effect of optical losses such as reflection and transmission. Internal QE deals with photons, that are not reflected or transmitted out of the cell.

1.7.5 Comparison of energy conversion efficiencies

Solar cell efficiency varies from 6% for amorphous Silicon-based solar cells to 40.7% [which is the efficiency of multiple-junction cells, produced in research labs]. Solar cell energy conversion efficiencies for commercially available micro crystalline Silicon [mc-Si] solar cells are around 14-16%. The highest efficiency cells have not always been the most economical — for example a 30% efficient multijunction cell, based on exotic materials such as Gallium Arsenide or Indium Selenide, and produced in low volume, will have a cost of about one hundred times that of an 8% efficient amorphous Silicon cell [which is having mass production], while only delivering about four times the electrical power.

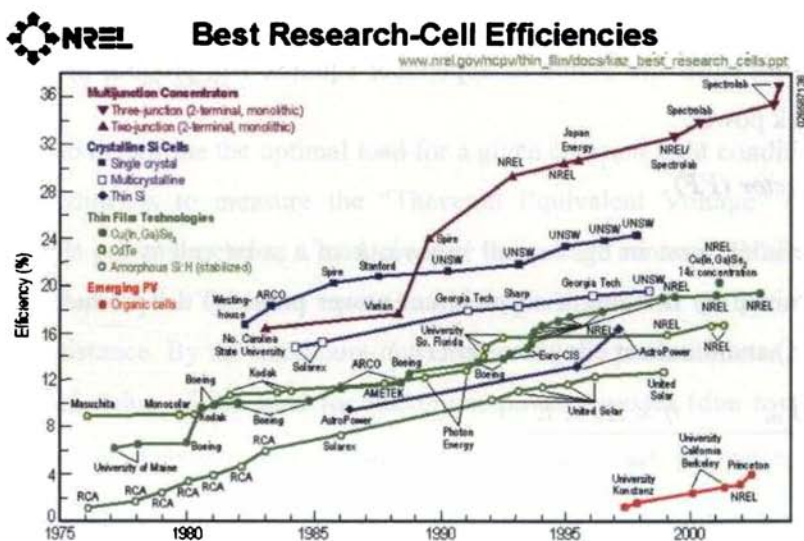


Fig.1.4: Reported timeline of solar cell energy conversion efficiencies (from National Renewable Energy Laboratory, USA)

To make practical use of the solar-generated energy, the electricity is most often fed into the electricity grid using inverters (grid-connected PV systems). In stand alone systems, batteries are used to store the energy that is not needed immediately. Fig 1.4 illustrates the best laboratory efficiencies obtained for various materials and technologies.

1.7.6 Peak watt (or watt peak)

Since solar cell output power depends on multiple factors, such as the sun's incidence angle, for comparison purposes between different cells and panels, the “peak watt (Wp)” is used. It is the output power under the following conditions:

Solar irradiance = 1000 W/m²

Solar reference spectrum = AM1.5

Cell temperature = 25°C

1.8 Solar cells and energy payback

It is a fact that we have to spend energy for the production as well as transportation of solar cells. There is a controversy whether a solar cell can produce energy more than this. The energy payback time of a solar panel, [assuming the working lifetime to be around 40 years], is anywhere from 1 to 20 years (usually less than five) depending on the type and usage. This means that solar cells can be net energy producers only if they generate more energy during their lifetime, than the energy expended in producing them. According to some experts, studying this question, solar cells do generate positive net energy, when the energy consumption for manufacturing and distribution is taken into account.

1.9 Three generations of development

Photovoltaic devices have undergone three generations of development.

1.9.1 The First

The first generation of photovoltaic devices consists of a large-area, single layer p-n junction diode, which is capable of generating usable electrical energy from light source

having the wavelengths of sunlight. These cells are typically made of Silicon wafer. First generation photovoltaic cells (also known as Silicon wafer-based solar cells) are still the dominant technology in the commercial production, accounting for more than 86% of the solar cell market.

1.9.2 The Second

The second generation of devices is based on the thin-films of semiconductors. These devices were initially designed to be highly efficient multiple junction photovoltaic cells. Later, as the major advantage of using a thin-film of materials was noted to be reducing the mass of material required for cell design, leading to reduction of cost as well as weight of the cells, there developed different technologies/semiconductor materials suitable for mass production, such as amorphous Silicon, poly-crystalline Silicon, micro-crystalline Silicon, Cadmium Telluride and Copper Indium Selenide/Sulfide. Even though the efficiencies of thin-film solar cells are lower than that of crystalline Silicon (wafer-based) solar cells, the manufacturing costs are much lower and hence lower cost per watt can be achieved. Another advantage of the reduced mass is that less support is needed for placing panels on rooftops and this allows fitting the panels on even flexible materials.

1.9.3 The Third

Third generation photovoltaic devices are very different from the other two, and are broadly defined as semiconductor devices which do not rely on a traditional p-n junction to separate photogenerated charge carriers. These new devices mainly include photoelectrochemical cells, polymer solar cells and nanocrystal/ defect material solar cells.

1.10 Current stage of development

24.7% efficient crystalline Silicon solar cell was developed at University of New South Wales, Australia.⁴ NREL has developed a record-efficiency $\text{Cu}(\text{In,Ga})\text{Se}_2/\text{CdS}$ cell, which possess the maximum among single junction, thin film solar cell of 19.9%.⁵

Spectrolab fabricated 40.7% tandem cell with GaInP/GaInAs/Ge triple-junction. The efficiency was measured under the standard spectrum for terrestrial concentrator solar cell at 240 suns ($24\text{W}/\text{cm}^2$).⁶ Organic solar cells have now reached an efficiency of 6%⁷ and Dye sensitized cell an efficiency of 11.1%.⁸

Most widely used cells are made of crystalline Silicon, which require larger thickness because of the indirect band gap. Moreover, Silicon extraction process requires sophisticated technologies which increase the cost of Silicon solar cells. As an alternative to this, the Second Generation Technology, [i.e. Thin Film Technology] gained prominence. Thin film solar cells use layers of semiconductor materials having only a few micrometres thick.

Thin film technology has many advantages like,

1. A variety of techniques are available for depositing thin films of same material
2. Reduction in material costs
3. Fewer processing steps
4. Simpler device processing and manufacturing technology for large area modules and arrays
5. Higher power to mass ratio
6. A wide variety of shapes, sizes, areas and substrates are possible
7. Different types of electronic junctions, single and tandem junctions are feasible
8. Graded band gap, graded composition, graded lattice constants can be obtained to meet requirements for a designer solar cell
9. Surface and grain boundaries can be passivated with suitable materials
10. Weight of the modules becomes less

Thin film technology has made it possible to have solar cells functioning as rooftop shingles, roof tiles and building facades. The solar cell version of items such as shingles offer the same protection and durability as ordinary asphalt shingles.

1.11 Important material properties for high efficiency cell

1. The band gap of the absorbing material must be small enough to allow absorption of an appreciable portion of a solar spectrum and at the same time large enough to minimize the reverse saturation current density J_0
2. The diffusion length of minority carriers must be as large as possible so that carriers excited by light, even at some distance from the actual semiconductor junction, will be able to diffuse to the junction and be collected before they recombine with the carriers of opposite sign. The diffusion length of minority carriers L_{\min} is given by

$$L_{\min} = (D_{\min} \tau_{\min})^{1/2} = \left[\left(\frac{kT}{q} \right) (\mu \tau)_{\min} \right]^{1/2}$$

where D_{\min} is the diffusion constant, τ_{\min} is the life time, μ_{\min} is the mobility for minority carriers, q is the electronic charge and k is the Boltzmann constant. Hence it is desired to have a material in which the minority carriers have large mobility and life time.

3. The actual junction structure and composition determines the magnitude of the junction transport current density, J_0 and the ideality factor, A . Formation of semiconductor junction must be carefully controlled to produce junctions with a junction current as low as possible
4. In an ideal solar cell, series resistance R_s should be equal to zero and shunt resistance R_{sh} equal to infinity. But in real solar cells, finite values of these resistances will be present and can be a major factor, particularly, in determining the effective values of the fill factor [FF]. Contributions to the series resistance can arise from the resistance of the semiconductor bulk and from contact resistance to the semiconductor to complete the circuit. The parallel resistance can be reduced by grain boundaries or other defects that enhance forward junction current and contributes to an increase in J_0 and a decrease in the voltage Φ_{oc} . In polycrystalline thin film solar cells, grain boundaries at the junction interface can critically affect junction transport properties.

5. Solar cells are used in exposed areas for long periods of time without failure which means that a variety of phenomena that might lead to the decrease in cell efficiency with time of exposure must be carefully considered.

All these factors must be carefully considered while making a thin film solar cell so as to maximize the efficiency.⁹

1.12 Materials for photovoltaic devices

1.12.1 Crystalline Silicon (c-Si)

Crystalline Si has almost an ideal band gap for solar energy conversion. It is one of the abundant materials on the earth's crust and hence it has a dominant role in the development of solar cells over the last 50 years. In 1981, the Si p-n homojunction cell was the only widely available solar cell. Monocrystalline Si with a grain size greater than 10cm and polycrystalline Si with grain size in the range of 1 μ m to 1mm are available. The cost of single crystal Si solar cells is greater than thin film multicrystalline Si solar cells. Single crystal Si solar cells require very high material quality, surfaces must be effectively passivated to reduce recombination there and the bulk properties must also be of high quality because of the long optical penetration distances associated with the indirect band gap of Si. Most of the solar cells exhibited in various simple demonstrations or applications are actually multicrystalline Si cells. Multicrystalline Si solar cells have been produced with efficiencies of ~ 17% and may be expensively produced from somewhat less pure starting materials using less expensive manufacturing methods.¹⁰

1.12.2 Amorphous Silicon (a-Si)

Amorphous Silicon (a-Si) PV modules were the first thin-film PV modules to be commercially produced. a-Si has a high density of co-ordination defects(dangling bonds) corresponding to departures from the local tetrahedral coordination between four Si atoms. They act as recombination centres to greatly reduce the carrier lifetime, carrier diffusion and drift lengths. This also helps to pin the Fermi energy in such a way that the material can not be effectively doped as p or n type. But now it has been observed that

incorporation of 10% of Hydrogen reduces the density of defects from 10^{19} cm^{-3} to 10^{16} cm^{-3} . Hydrogenated amorphous Si alloy [a-Si: H] has a higher energy absorption edge and larger optical absorption constant for solar radiation than crystalline Silicon. Only 1 - 2 μm thickness of a-Si:H is required to absorb virtually all of the light above the absorption edge. However, the efficiencies of these modules have not yet reached levels that were predicted in the 1980's. To a significant degree this is due to the intrinsic degradation of a-Si under illumination. The use of multi-band gap multijunction devices (allowing the use of thinner absorber layers in the component cells) and the use of light-trapping appear to be the most powerful device design techniques to improve stabilized device performance. Presently, champion cells have stabilized efficiencies of 12% and champion modules (1 square foot) have stabilized efficiencies of over 10%. The use of multi-band gap multijunction devices (allowing the use of thinner absorber layers in the component cells) and the use of light-trapping appear to be the most powerful device design techniques to improve stabilized device performance.

1.12.3 Gallium Arsenide (GaAs)

The direct band gap of GaAs (1.43eV) is near the optimum for solar energy conversion and it leads to 97% absorption of AM1.5 radiation in a thickness of about 2 μm . The carrier mobility of this material is higher than that of Si and it forms a variety of lattice-matched ternary compounds allowing for controlled variations of properties. Common dopants include S, Se, Te, Sn, Si, C and Ge as shallow donors and Zn, Be, Mg, Cd, Si, Ge and C as shallow acceptors. The dopants from column IV-C, Si, Ge and Sn are amphoteric in GaAs, behaving as donors or acceptors depending on whether they go onto Ga or As sub lattice and their electrical behaviour depends on the condition of the growth. Efficiencies of GaAs based solar cells are among the highest of any solar cells, lying between 20-30%. One of the major advantages of GaAs solar cell is its insensitivity to increase in temperature. Measurements indicate that there is only 0.033% decrease in efficiency per degree Centegrade. GaAs has better radiation hardness than Si. These factors mean that GaAs cells have been developed primarily for use in space. The most likely terrestrial application is for power generation under concentrated light. The

multijunction solar cell with GaInP/GaInAs/Ge structure has achieved a record efficiency of 40.7% at 240suns, under the standard spectrum for terrestrial concentrator solar cells (fabricated at Spectrolab, USA).

1.12.4 Indium Phosphide (InP)

Similar to GaAs, Indium Phosphide is a direct band gap material with an E_g of 1.34eV. Also like GaAs, homojunction cells are limited by surface recombination at the incident surface, but heterojunctions with good lattice matching. But 'heteroface junctions' are much more efficient. InP based cells are more radiation resistant than GaAs cells. Hydrogenation of $n^+ - p$ InP solar cells has been shown to be increasing the efficiency to 17.5% at AM0 because of reduction in carrier concentration in the near -surface layer due to the formation of an acceptor-hydrogen complex. Due to the high cost of InP, only thin films with thickness $< 2\mu\text{m}$ were made. CdS/InP junction prepared on polycrystalline InP have shown an efficiency of 5.7%.

1.12.5 Cadmium Telluride (CdTe)

CdTe is again a direct band gap material, having an E_g of 1.44eV, strongly absorbing the solar spectrum within a few micrometres thickness. CdTe has a strong tendency to grow as highly stoichiometric, but p-type semiconductor film and can form a p-n heterojunction with CdS. CdTe have now reached up to an efficiency of 16.5%. Efficiencies up to 18% can be expected for the CdTe cell made under a mature technology. The maximum theoretical efficiency of CdTe solar cells is 27.5%.

1.12.6 Copper Indium Sulfide (CuInS₂)

CuInS₂ is particularly a promising candidate because of its optimum direct band gap of 1.5eV for solar energy conversion. The conductivity type can be changed. This is one of the I-III-VI₂ type semiconductors that crystallize in chalcopyrite structure. Wider band gap of CuInS₂ compared to other widely used chalcopyrites, such as CuInSe₂, has an advantage of potentially higher open circuit voltages. Theoretically predicted efficiency of the homojunction of this material ranges between 27 and 32%. Recently CuInS₂ based cells has reached an efficiency of 11.4%.

1.12.7 Copper Indium Selenide (CuInSe_2 -CIS)

With an efficiency of 19.9% on the laboratory scale and 13.4% for the power modules, CuInSe_2 has become the most efficient thin film technology today. The favourable properties of this material are listed below

1.13 Properties of CuInSe_2

1.13.1 Tetragonal chalcopyrite structure

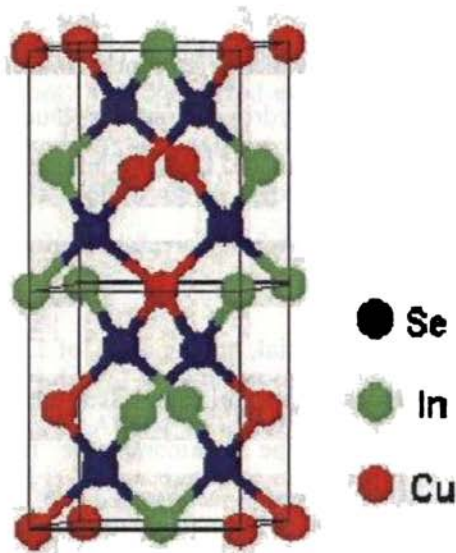


Fig.1.5: Structure of CuInSe_2

Stable crystal structure of CIS is a subset of adamantine class and is named after the mineral chalcopyrite, CuFeS_2 . Characteristic feature of the adamantine structure is the tetragonal arrangement of atoms in which each atom has four nearest neighbours. CIS crystallizes in this form at room temperature and reverts to the sphalerite structure (δ phase) above 1073K. Bonding is mainly covalent because of the tetrahedral coordination. In general, various compound crystal structures are derived from the basic diamond close-packed structure. It has a sub lattice of anion in cubic close packing (as in the Zinc Blend (sphalerite) structure) or in hexagonal close packed type (as in the Wurtzite structure). CIS is obtained from the cubic Zinc blende structure of II-VI

materials like ZnSe by occupying the Zn sites alternately with Cu and In atoms. Each I(Cu) and III(In) atom has four bonds to the VI (Se) atom. In turn, each Se atom has two bonds to Cu and two to In. Because the strengths of the I-VI and III-VI bonds are in general different, the ratio of the lattice constants c/a is not exactly two. Instead, the quantity $2-c/a$ is a measure of tetragonal distortion in chalcopyrite materials.

1.13.2 Band gap of 1eV at room temperature

CIS has a relatively small band gap of 1.04 eV, which enables it to absorb a large portion of the solar spectrum. It also has a direct band structure thereby minimizing the requirements for large minority carrier diffusion length, since carriers are photoexcited close to the collecting junction. By partial substitution of In with Ga or Al [ie. $\text{Cu}(\text{In,Ga})\text{Se}_2$, or $\text{Cu}(\text{In,Al})\text{Se}_2$] and Se by S [$\text{CuIn}(\text{S,Se}_2)$], the band gap value can be systematically shifted between 1.04 eV and 1.68 eV. This phenomenon allows for an optimum match with the solar spectrum.

1.13.3 High absorption co-efficient of 10^5 cm^{-1}

CIS has an absorption co-efficient ($\alpha > 10^5 \text{ cm}^{-1}$) which implies that 99% of the incoming photons are absorbed within the first micrometre of the material. As a result, only 1-2 μm of this material is sufficient to effectively absorb the incoming photons compared to bulk Si, where at least 300 μm of material is required.

1.13.4 Large structural tolerance to off-stoichiometry

A noticeable feature of CuInSe_2 , deposited by evaporation and several other techniques is the tendency to have average compositions to lie along a pseudo-binary composition line connecting the compounds Cu_2Se and In_2Se_3 on the Cu-In-Se ternary phase diagram. However, the deposited layers are found to be predominantly single phase when stoichiometric or slightly In-rich, while two phase $\text{CuInSe}_2 + \text{Cu}_2\text{Se}$ has been reported for Cu-rich material.¹¹

1.13.5 Excellent stability and high radiation resistance

CIS-based solar cell devices have demonstrated good thermal, environmental and electrical stability. Preliminary test have indicated that the radiation tolerance of CIS thin films is superior to that of single-crystalline Si or GaAs devices when tested under high energy electron and proton radiation

1.13.6 Fabrication on variety of substrates

CuInSe₂ thin films are now prepared on light weight flexible substrates which improves its suitability in space applications. CIS cells were already fabricated successfully on Molybdenum foil, Polymeric, metallic foils of Aluminium, Titanium, Stainless steel and Ni-alloys, Plastic and Polyimide foils.¹²⁻¹⁶

1.14 Mile stones in the development of CIS based solar cells

1953: CIS was synthesized for the first time by Hahn

1974: CIS was proposed as a photovoltaic material with a power conversion efficiency of 12% for a single crystal solar cell

1976: L.L. Kazmerski et al. reported 5.7% efficiency polycrystalline solar cells

1983-84: Boeing Corp. reported efficiencies in excess of 10% from thin polycrystalline films obtained from a three source co-evaporation process

1987: Arco solar achieved a long-standing record efficiency of 14.1% for a thin film solar cell

1998: The first commercial Cu(In,Ga)Se₂ solar modules were available

1999: Conversion efficiency reached 18.8% (NREL, USA)

2003: Conversion efficiency reached 19.2% (NREL)

2008: Conversion efficiency reached 19.9% (NREL) on the laboratory scale and 13.4% on the commercial scale

1.15 Review on CIS thin films

CIS can be prepared using both vacuum and non-vacuum processes.

1.15.1 Vacuum processes

Vacuum processes include thermal, flash and electron beam gun evaporations, sputtering, laser ablation, rapid thermal processing (RTP) and molecular beam epitaxy (MBE).

(i) Evaporation

Vacuum evaporation is a commonly used technique in the deposition of CIS thin films which includes thermal evaporation, flash evaporation and electron beam evaporation. The record-breaking 19.9% CIGS cell was prepared using thermal evaporation (co-evaporation). The development of this method dates back to 1972 and currently it has become, one of the feasible methods for CIS preparation.

Neumann et al. prepared CIS epitaxial layers by single-source evaporation and found that source temperatures above 1400K were necessary for the deposition of single-phase and nearly stoichiometric CuInSe_2 films.¹⁷ Neelkanth et al. prepared CIS films using co-evaporation of constituent elements at a substrate temperature of 350°C. The band gap varied in the range 1.02-1.04eV. Thickness was in the range 0.15-1 μm .¹⁸ Varela et al prepared CIS thin films using co-evaporation of Cu, In and Se. The films were deposited at different temperatures in the range 175-400°C.¹⁹ Mikihiro Nishitani et al. prepared CIS by co-evaporation of the elements under an ultrahigh vacuum by a molecular-beam deposition method. The process was found to be suitable for the fabrication of stoichiometric or slightly In rich films.²⁰ S. T. Lakshmikummar demonstrated gas phase selenization of vacuum deposited Cu and In thin films employing an elemental Se vapour source for the deposition of CIS thin films. The selenization reaction readily occurred at Cu and In films kept at 340–400°C. Lower selenization temperatures invariably led to the formation of Cu and In selenides with well defined crystalline microstructures.²¹ Guillen et al prepared CIS by sequential evaporation of stacked Cu and In layers and subsequent chalcopyrite formation using elemental Se within a closed-space graphite container

placed into a newly developed vacuum environment at 400°C in nitrogen atmosphere.²² These films showed smoother surface, higher grain size and uniformity when reactor pressure was increased during the selenization process. C Calderon et al. prepared CIS using sequential evaporation of Cu, In₂Se₃ and Se.²³ Mario Gossila et al. developed a new five-source PVD for the deposition of Cu(In_{1-x}Ga_x)(Se_{1-y}S_y)₂ absorber layers. By varying the sulfur contents (in Cu-poor samples), the band gap could be increased to 1.5eV and best cell showed an efficiency of 10%.²⁴ Sung Chan Park et al. studied the electrical properties of CIS films prepared by evaporation of Cu₂Se and In₂Se₃ compounds. CIS film grown at 680°C had a smooth and dense microstructure with the grain size of 2 -3 μm. H₂ post annealing was conducted to control the electrical resistivity and composition of CIS films. In H₂ atmosphere, the resistivity increased to about 100Ωcm by annealing at 350°C for 1 h. The resistivity decreased again when the annealing temperature was above 350°C.²⁵

T Schlenker et al. reported the initial growth behaviour of Cu(InGa)Se₂ prepared using co-evaporation on Molybdenum substrates. It was observed that the growth on polycrystalline Mo substrates fabricated by sputter process, a power law dependence between the island density and the deposition rate and an exponential dependence of the island density on substrate temperature. On electron gun evaporated Mo, the nucleation mechanism deviated from the model of homogeneous nucleation and strong island density fluctuations occurred.²⁶ M J Romero et al. studied the surface widening in CuInGaSe₂ thin films prepared using three stage physical vapour deposition. This widening of the surface was confirmed using transmission electron microscopy and cathodoluminescence spectroscopy.²⁷ Akhlesh Gupta et al. carried out studies on Cu-In precursor for the preparation of CIS thin films by the selenization technique. The effect of temperature on the degree of alloy formation between Cu and In layers was studied. The mechanism of alloy formation was different in bilayers annealed at temperatures lower and higher than the melting point of In, or prepared by deposition of Cu and In at 200°C and 150°C, respectively. While the annealing of the precursor up to 200°C

produced an alloy in the interface region of Cu and In layers, annealing at 500°C completely changed its morphology.²⁸

A Moharram et al. studied the optical and structural changes of thermally co-evaporated CIS films. Increasing In content on the expense of Se atoms, decreased the amount of Se phase which had higher energy band gap. Tetragonal CIS and hexagonal Cu₂Se crystalline phases were resulted from thermal annealing.³⁰ O Rodriguez et al, performed the chemical analysis of CIS prepared using evaporation through a multistage process. It was observed that the samples prepared using two stage processes are Cu-rich and that prepared using three stage process was Cu-poor. It was found that the films from three stage process were suitable for solar cell fabrication.³¹ A. Ashour et al. studied polycrystalline CIS thin film formation on glass substrates by preparing stacked elemental layers (SELS) of Cu, In and Se followed by annealing at 200, 250, 300 and 400°C for different times (from 15 to 240 min). It was concluded that a single phase of CIS film was obtained at a reaction temperature of 300°C for a heating time ≥ 1 h.³² C. Guillén et al. studied the Structure, morphology and photoelectrochemical activity of CIS thin films grown by the sequential evaporation of Cu and In layers, and subsequent reaction at 400°C with elemental selenium vapour. An improvement in the CIS quantum efficiency, related mainly to the increased homogeneity and smoothing of the sample surface, could be gained by using as precursors multiple stacked Cu–In bilayers evaporated onto unheated substrates.³³ C. F. Kurdesau et al. performed in situ resistivity measurements during selenization of co-evaporated Cu–In layers in Se/N₂ gas mixture at atmospheric pressure. For selenization processes and in situ measurements a special container (a quasi-closed system) with mechanical contacts to the selenized film was constructed. The total resistance of the metallic layers and the contact system was approximately 10 Ω before the reaction starts. During the selenization processes it increased to more than 10 k Ω , indicating the conversion of metals into CIS. The resistivity curve indicated the start and end point of the chemical reactions and identified three different stages of conversion.³⁴ A. G. Chowles et al. carried out in situ RBS analysis of CIS prepared by sequential evaporation of the constituent elements onto Mo-

coated glass substrates and the layers were subsequently selenized in a closed graphite box at 400°C. For the Cu/In/Se structure, XRD performed after various anneals revealed that the Cu–In layer mixed with the Se layer to form a number of binary phases. For Cu/Se/In it was found that the Cu and Se had intermixed at room temperature. In both the structures the Cu–Se and In–Se binary phases formed below 200°C and upon annealing above this temperature interdiffused to form chalcopyrite CIS.³⁵ A. Brummer et al. studied the formation of CIS by the annealing of stacked elemental layers. CIS crystallized from the direct precursors Cu₂Se (Cu_{2-x}Se, respectively) and InSe within a melt rich in selenium. Both, Na and Ga promoted the crystallization of Cu₂Se, the direct precursor phase for CIS. A comparison of the crystallographic structures of Cu₂Se and InSe showed that epitaxial growth of InSe (0001) on Cu₂Se (111) lattice planes was feasible.³⁶ R. Caballero studied CIS formation by selenization of sequentially evaporated metallic layers. The selenization procedure was carried out within a partially closed graphite container. The CIS films showed single-phase chalcopyrite structure with preferential orientation in the (1 1 2) direction after 500°C selenization. The CIS surface morphology depended on the sequence used. The In/Cu/In seemed to be the best. An energy band gap above 0.95 eV and an absorption coefficient near 10⁵ cm⁻¹ were obtained and similar optical properties were observed for all the prepared sequences.³⁷ In the highest efficiency cell (Contreras et al.), CIGS was prepared by thermal co-evaporation which includes three stages. At the first stage, the composition was made Cu-rich, which aided the formation of high-quality, large-grained polycrystalline material. The second stage includes evaporation of In, Ga and Se to titrate the excess (Cu,Se) from the film aggregate. At the third stage, a small quantity In and Ga were added which assist the formation of a smooth surface and to facilitate the formation of a Cu-poor defect chalcopyrite that exist at the surface of CIS films.³⁸

Flash evaporation and electron beam gun evaporation were also used to deposit CuInSe₂ films. Joseph et al. prepared CIS using flash evaporation and samples were p-type. Activation energy of 75meV was obtained for room temperature deposited (non-annealed) film, which was attributed to Se interstitials acting like acceptors. Activation

energy of 15 meV observed in film annealed at 50°C, was attributed to In_{Cu} defect level while value of around 30meV observed in other films annealed up to 200°C, was attributed to Cu_{In} defect level.³⁹ Akl et al performed structural study of flash evaporated CIS thin films.⁴⁰ M. Klenk et al. studied the properties of flash evaporated chalcopyrite absorber films and solar cells.⁴¹ C.Guillen et al studied structure, morphology and photoelectrochemical activity of CIS thin films as determined by the characteristics of evaporated metallic precursors. An improvement in the quantum efficiency, related mainly to the increased homogeneity and smoothing of the sample surface, could be gained by using multiple stacked Cu-In bilayers evaporated onto unheated substrate as precursors.⁴²

(ii) Sputtering

I Martil et al. prepared CIS films by rf sputtering in Ar/H₂ atmosphere. Measurements of resistivity at various temperatures indicated a hopping conduction mechanism through gap states for films grown at low temperature (100-250°C), the existence of three acceptor levels at about 0.046, 0.098 and 0.144eV above valence band for films grown at intermediate temperature (250-350°C) and a pseudo-metallic behaviour for films grown at high temperatures (350-450 °C).⁴³ P Menna et al. performed the study of Selenium incorporation in sputtered Cu-In alloys. Selenium incorporated in the ternary compound assumed a constant value around 48% while the Cu/In ratio ranged between 0.8 and 1.2. As the copper content was further lowered, Selenium decisively increased up to almost 51% when Cu/In is 0.6. The inversion point in the Se-Cu/In diagram was correlated to the formation of a secondary phase identified as the chalcopyrite vacancy-variant compound $\text{CuIn}_3\text{Se}_5(\text{OVC})$.⁴⁴ Sang Deok Kim characterized CIS thin films grown by selenization of co-sputtered Cu-In alloy layers, which consisted of only two phases, CuIn_2 and $\text{Cu}_{11}\text{In}_9$. The CIS films selenized in vacuum had large grain sizes, smooth surfaces and dense microstructures.⁴⁵ J. Schmidt et al. prepared thin films of CIS by selenizing co-sputtered Cu-In films with selenium vapour. The conductivity types were p-type for Cu-rich and n-type for near-stoichiometric and In-rich films. All samples showed a thermally activated conductivity for higher temperatures and the

variable-range hopping conduction mechanism in the lower temperature range. The dependence of the absorption coefficient on incident photon energy indicated allowed direct transitions with energies in the range 0.96–1.01 eV.⁴⁶ F. O. Adurodija et al. carried out the characterization of co-sputtered Cu-In alloy precursors for CIS thin films fabrication by close-spaced selenization. The co-sputtering technique for producing Cu-In alloy films and selenization within a close-spaced graphite box resulting in quality CIS films was developed. Very In-rich films yielded the ODC compound with small crystal sizes whilst slightly In-rich or Cu-rich alloys yielded single phase CIS films with dense crystals and sizes of about 5 μm . Film resistivity varied from 10^{-2} – $10^8 \Omega \text{ cm}$. The films had compositions with Cu/In of 0.40–2.3 and Se/(Cu+In) of 0.74–1.35. All CIS films with the exception of very Cu-rich ones contained high amount of Se (>50%).⁴⁷ Tooru Tanaka et al. studied the effect of substrate temperature on properties of thin films prepared by RF sputtering from CIS target with Na_2Se . The copper content was found to decrease with increasing the substrate temperature, and the band gap of the thin films became large, suggesting the formation of CuIn_3Se_5 structure. The reduction of copper content was presumed to be due to the surface reaction during the growth. The effect of 8 MeV electron irradiation on electrical properties of CIS thin films were also studied. The n-type CIS films in which the carrier concentration was about $3 \times 10^{16} \text{ cm}^{-3}$, were epitaxially grown on a GaAs(0 0 1) substrate by RF diode sputtering. No significant change in the electrical properties was observed under the electron fluence $< 3 \times 10^{16} \text{ e cm}^{-2}$. As the electron fluence exceeded $10^{17} \text{ e cm}^{-2}$, both the carrier concentration and Hall mobility slightly decreased. The carrier removal rate was estimated to be about 0.8 cm^{-1} , which was slightly lower than that of III–V compound materials.^{48,49} J. Müller et al. studied the composition, structure and optical properties of sputtered thin films of CIS. Results of EDAX analysis revealed that the sputtered films were near to stoichiometry for substrate temperatures T_{Sub} not exceeding 200°C . XRD patterns indicated that the films exhibited some pattern similar to that of bulk crystals of tetragonal chalcopyrite, predominantly (112) oriented. The band gap E_g , estimated from optical absorption data, was between 0.6–1.08 eV, depending on sputtering conditions

such as substrate temperature and bias voltage. High optical absorption coefficients ($> 10^4 \text{ cm}^{-1}$) were found.⁵⁰

(iii) Laser ablation

Yoshida et al. prepared CIS thin films with large grain by XeCl excimer laser ablation on glass substrates. The deposition was carried out at 550°C and the target-substrate distance was changed from 15 to 60 mm. All films showed the single-phase and stoichiometric chalcopyrite structure, independent of the distance. The deposition rate was large with the small distance. The electrical conductivity measurements gave p-type conduction, and the mobility was improved with the smaller distance.⁵¹ V. V. Kindyak et al. studied the optical transitions in laser-evaporated CIS thin films. The optical absorption coefficients of highly oriented laser-evaporated thin films were determined from the measured reflectance $R(\lambda)$ and transmittance $T(\lambda)$ in the wavelength range 400–1700 nm. The optical absorption spectrum of CIS thin films showed three energy gaps, which were associated with the fundamental edge and valence band splitting by the tetragonal crystal-field and spin-orbit effects, and four optical transitions from the Copper d levels to the conduction bands.⁵² S. Kuranouchi et al. studied the annealing effects of CIS films prepared by pulsed laser deposition. The composition of annealed films was Cu-rich and no significant loss of Selenium was observed. The liquid (Cu_xSe)-solid (CIS) growth mechanism was suggested and the CIS grain growth was enhanced.⁵³ A. Tverjanovich et al. prepared CIS thin films by UV laser ablation.⁵⁴

(iv) Rapid Thermal Processing (RTP)

W Riedl et al. analyzed the surface microstructure of CIS thin films produced by rapid thermal processing by scanning tunneling microscopy and spectroscopy in ambient air. Although the bulk material of all samples investigated was p-conductive, abrupt changes of the conductivity type of the surfaces from p- to n-type were observed as a function of the overall Cu/In ratio. The dominant current flow direction in slightly Cu-rich thin film bulk material was associated with p-type conduction, whereas In-rich samples exhibited largely n-type conductivity at the surface.⁵⁵ V Alberts et al. studied the material

properties of CIS prepared by rapid thermal treatment of metallic alloys in H₂Se/Ar. Selenization at temperatures around 400°C resulted in a sharp increase in Cu/In atomic ratio due to the loss of Indium from the samples. Homogeneous and dense films were formed without Cu-rich binary phases in the case of samples which were rapidly heated and selenized at temperatures around 400°C.⁵⁶ J. Keranen et al. studied the effect of sulfurization on the microstructure of chalcopyrite thin-film absorbers. Rapid thermal processing in H₂S atmosphere with processing temperatures ranging from 350 to 550°C was used to sulfurize the absorber. A non-uniform and porous surface reaction layer was evident in the CIS and CIGS structures after the RTP. The CIGS structure had a tendency towards a phase separation, whereas, the CIS films exhibited mixed sulfoselenides, CuIn(Se_{1-x}S_x)₂, where x varies. In order to improve the device performance, the formation of two distinct phases should be avoided during the sulfurization processing.⁵⁷

(v) *Monocrystalline CIS*

CIS single crystals were also well studied. S Niki et al. studied the effects of annealing on CIS films grown by molecular beam epitaxy on GaAs (0 0 1) at substrate temperatures of T_s = 450–500°C and the effects of annealing under various atmospheres. An epitaxially grown In₂O₃ phase was found both in Cu-rich and In-rich films annealed at T_A = 350°C, which was not observed in the films annealed in Ar atmosphere. Thermodynamic calculations based on the Cu-In-Se-O-N system showed In₂O₃ to be the most stable phase in good agreement with the experimental results.⁵⁸ K. Yoshino et al. studied the temperature dependence of photoacoustic spectra in CIS thin films grown on (0 0 1)-oriented GaAs substrate by molecular beam epitaxy (MBE) at substrate temperature of T_s = 450°C. The samples were characterized by means of piezoelectric photoacoustic (PPA) measurements between liquid helium (4.2 K) and room temperature (300 K). Two distinct PPA signals due to band gap of CIS and GaAs were observed in the whole temperature range from 4.2 to 300 K and the PPA signals of CIS decreased at the temperature range. Since the PPA signals of CIS thin films could be obtained up to room temperature, the PPA measurements were quite effective to obtain the optical characterizations, especially for the non-radiative recombination processes.⁵⁹ A. N.

Tiwari et al. carried out a review on heteroepitaxy of CuIn_xSe_y . Molecular beam epitaxy has been used to grow heteroepitaxial CuIn_xSe_y layers on Si and GaAs substrates. Layers of different Cu/In ratios have been grown to study the formation of different phases such as CIS chalcopyrite (α -phase) and defect-chalcopyrite/stannite phases (β -phase) in this material system. An interfacial CuSe_xSi_y layer is formed during the growth of CuIn_xSe_y on Si. In the case of GaAs substrates, Ga from the substrate diffuses into the CuIn_xSe_y and a quaternary compound $\text{Cu}(\text{In,Ga})_x\text{Se}_y$ is formed at the interface.⁶⁰ James H. Ely et al. characterized epitaxial Cu–In–Se thin films using Raman spectroscopy. Epitaxial chalcopyrite alloys (CIS (001) and CuIn_3Se_5 (001)) were fabricated with varying compositions and thicknesses on GaAs (001) substrates using a simple physical vapour deposition method. All of the spectra were dominated by the $A_1(\Gamma_1^{(1)} [W_1])$ non-polar optical mode at 172 cm^{-1} for CIS and 152 cm^{-1} for the CuIn_3Se_5 phase. In addition, Raman spectra for the thinner layers indicated that these films were under compressive stress due to the lattice mismatch between the films and the substrate.⁶¹ Tooru Tanaka et al. prepared CIS by epitaxial growth and studied the effect chlorine ion implantation on electrical properties. The conductivity type in all implanted films was n-type and the carrier concentration was increased with increasing Cl concentration in the films. Cl acts as a donor in CIS.⁶²

A. Zegadi et al. performed photoacoustic study on the effect of Se content on defect levels in CIS single crystals.⁶³ Champness et al. prepared monocrystalline CIS by vertical Bridgman technique with non-stoichiometric proportions of the starting elements Cu, In and Se. With stoichiometry or an excess of Se the ingots were p-type. With a deficiency of Se, n-type conductivity was obtained but with binary phases such as InSe present in the last zone of the ingot.⁶⁴ H. P. Wang et al. reported studies on monocrystalline CIS and CuIn_3Se_5 in photovoltaic cells using monocrystalline CIS as a substrate. Pre-annealing the substrate in argon at 350°C for about 2 h improved photovoltaic performance. Measurements of Auger profiles in the first 200\AA or so of annealed and unannealed monocrystalline samples indicated no evidence of the formation of an OVC near the surface during the heat-treatment process.⁶⁵ Champness et al. also studied the effect of

annealing of monocrystalline CIS samples. In monocrystalline p-type CIS samples, with a room temperature hole concentration of approximately 10^{17} cm^{-3} , partial type-conversion was observed to take place after heat-treatment at 500°C in argon at atmospheric pressure. The depth of the outer n-layer in the original p-type material, as determined by hot probing and etching, increased approximately as the square root of the annealing time.⁶⁶ K. Timmo et al. studied CIS monograin growth in the liquid phase of potassium iodide. All the grown powder materials with narrow-disperse granularity were chalcopyrite CIS. The grown crystallites had tetrahedral shapes and homogeneous composition. Particle size distribution was used to describe the growth process. The activation energy of linear growth of crystals was $E_d = 0.25 \pm 0.05 \text{ eV}$, and the power of time dependence of the crystal growth was $1/n = 0.26 \pm 0.06$. The solubility of CIS in KI at 990 K was $0.17 \pm 0.05 \text{ wt. \%}$. The solubility of potassium and iodine in CIS at 990 K was 0.094 wt. \% , and 0.0086 wt. \% , respectively. As a result, homogeneous p-type CIS monograin materials were synthesized in KI solvent.⁶⁷

1.15.2 Non-vacuum processes

Non-vacuum processes are attractive for reducing the high initial cost of physical vapour deposition processes. CBD, electroless deposition, ink coating, CSP, MOCVD and SILAR are considered as the non-vacuum processes in CIS deposition.

(i) Chemical Bath Deposition (CBD)

P.K.Vidyadharan Pillai fabricated CIS/CdS solar cell completely by CBD and characterization was performed. An efficiency of 3.1% was obtained for this CBD cell.⁶⁸ Bindu et al. prepared CIS thin films combining CBD and PVD in which Se was deposited using CBD and Cu and In using PVD. In this work, Se precipitate remaining in the bath after deposition of Se film was recovered for the use as starting material for further deposition process.⁶⁹

(ii) Electrodeposition

Pankaj Garg et al. studied the growth and characterization of electrodeposited CIS thin films from seleno-sulphate solution. The films deposited at a deposition current density

of $J = 1.1 \text{ mA/cm}^2$ with InCl₃ (15.12 mM) content in the bath mixture and at $J = 0.8 \text{ mA/cm}^2$ with InCl₃ (18.6 mM) content have a stoichiometric chalcopyrite structure with $c/a = 1.97$. Electrical measurements showed that deposited films were p-type and had a resistivity of about $5 \times 10^3 \text{ } \Omega \text{ cm}$.⁷⁰ N. Khare et al. studied the photoelectrochemical, electrolyte, electroreflectance and topological characterization of electrodeposited CIS films. n-type CIS thin films were obtained by electrodeposition from a chloride bath containing SeO₂ and annealed at different temperatures in N₂ plus either 5% H₂ or a few parts per million O₂. When the heat treatment temperature was increased, the band gap decreased from about 1.07 to 0.98 eV.⁷¹ S. R. Kumar et al. developed a nonaqueous method to electrodeposit Cu-In alloy precursor for n-CIS films. Flash annealing of the stacked Cu-In alloy/Se layers had been used to prepare CIS films and the flashed n-CIS films had a chalcopyrite structure with strongly oriented (112) planes.⁷² A. N. Molin et al. prepared CIS thin films by electrodeposition from citric aqueous solutions containing Cu, In and Se. It was shown that the chemical reaction determining the common rate of electrodeposition was SeO₃²⁻ reduction by metallic copper.⁷³ H. P. Fritz et al. developed a novel method for the electrodeposition of the metallic grey hexagonal modification of selenium using the system. Se[(EtO)₂PS₂]₂/n-Bu₄NBF₄/chlorobenzene with simultaneous illumination of the cathode.⁷⁴ R. Pal examined the variation of trap state density and barrier height with Cu/In ratio in CIS films. The density of trap states in the intercrystalline region of the films was found to increase with increasing Cu/In ratio. The effect of illumination on the grain boundary barrier height was studied and this indicated that the grain boundary charges are depleted by sub-band gap photons resulting in the reduction of the barrier height with increase of illumination level.⁷⁵ S. Jost et al. studied the formation of CIS thin-film solar cell absorbers by laser annealing of electrodeposited precursors. All absorbers processed with laser or furnace annealing consisted of crystalline CIS in the chalcopyrite crystal structure with a high degree of cation disorder. Laser annealing did not lead to unintentional selenium loss during the semiconductor formation process.⁷⁶ S. Nakamura et al. studied the electrodeposition of Cu-In-Se films

with an aqueous solution containing CuCl_2 , InCl_3 and SeO_2 , in terms of composition control of deposited films for the preparation of CIS.⁷⁷

Shalini et al. developed a novel approach to prepare CIS-based thin-film photovoltaic cells. Cells were constructed using n-type CIS with a concentrated effort on the synthesis of n-CIS thin-film absorber. They also aimed at the electrochemical conversion of CIS surface to a semi-insulating, lattice-matched $\text{CuIn}_x\text{Se}_y\text{I}_z$ transition layer and a semi-conducting p-CuISe₃ window.⁷⁸ C. Guillen et al. analyzed the improvement of the optical properties of electrodeposited CIS thin films by thermal and chemical treatments. In order to eliminate the semi metallic phases and to improve the semiconductor behaviour of the electrodeposited material, thermal and chemical treatments were performed. After heat-treatment of the samples at 400°C in flowing argon, elemental Selenium loss has been detected together with an enhancement of the allowed direct optical transition. The subsequent chemical etching of the layers in a KCN solution showed to be successful in eliminating the copper selenide phases which were responsible of the remaining sub-band gap absorption.⁷⁹ P.P. Prosini et al. carried out electrodeposition of Copper-Indium alloy under diffusion-limiting current control. The relationship between the ratio of Cu^{2+} to In^{3+} in the solution and the metal ratio in the deposited film was investigated. In order to avoid the use of complexing agents, the stoichiometry of the Copper-Indium alloys was controlled by electrodepositing them under diffusion-limiting current.⁸⁰ S.N. Qiu et al. carried out the diffusion length measurements on electrodeposited CIS cells. The diffusion length of the CIS with an acceptor concentration less than $2 \times 10^{16} \text{ cm}^{-3}$ was not very sensitive to the variation of concentration. The diffusion length of the order of 0.52 μm was obtained at 1.2 μm wavelength which was closer to the value 0.6 μm for evaporated CIS.⁸¹ A. M. Fernandez et al., performed the characterization of co-electrodeposited and selenized CIS (CIS) thin films. As-deposited as well as selenized films exhibited a compact or a granular morphology depending on the composition. The film stoichiometry was improved after selenization at 550 °C in a tubular furnace.⁸² A.M.Fernandez et al characterized co-electrodeposited and selenized CIS thin films. The films were formed with a mixed composition of binary as well as ternary phases.⁸³ E.

Tzvetkova et al. prepared CIS thin films by one-step electrodeposition process. The deposition was done in potentiostatic regime from an original electrolyte containing Cu^+ , In^{3+} , Se^{4+} ions and thiocyanate as a complexing agent. It was established that Se treatment was more effective than the annealing in Ar in addition to crystallite size.⁸⁴ N. Stratieva et al. prepared CIS by electrodeposition from a thiocyanate electrolyte with a complexing agent. The annealing in Ar ambient did not influence the composition of the layers considerably but improved the crystalline structure.⁸⁵ R. P. Raffaele et al. carried out scanning tunneling microscopic analysis of electrodeposited CIS nanoscale multilayers. Alternating layers of two different compositions based on the $\text{Cu}_x\text{In}_{2-x}\text{Se}_2$ system were potentiostatically deposited. These nanometer-scale layers were used to form reduced-dimensionality structures such as superlattices that could be used in concentrator solar cells.⁸⁶ A. M. Fernandez et al. on the characterization of electrodeposited and selenized CIS thin films. The selenization process was carried out using chemical vapour transport by gas (CVTG). The film stoichiometry improved after selenization at 550°C .⁸⁷ A.A.I. Al-Bassam prepared CIS by electrodeposition. A structural transition from chalcopyrite to sphalerite was observed on the electrodeposited CIS, when the composition of the thin films was varied from a quasi-stoichiometry to In rich. Quasi-stoichiometric CIS thin films were obtained in the chalcopyrite structure with grain sizes of the matter of $0.06\mu\text{m}$.⁸⁸ L. Zhang et al. studied the formation of CIS and $\text{Cu}(\text{In,Ga})\text{Se}_2$ films by electrodeposition and vacuum annealing treatment. All the as-deposited films were annealed in vacuum at 450°C for a short time to improve the crystalline properties. The crystallization of the films was greatly improved after annealing. Further more, a CIGS film with 23 at% Ga was obtained.⁸⁹

J.L.Xu et al studied influence of vacuum annealing process on electrodeposited CIS films. Crystallization of the films was greatly improved by fast annealing process without significant change in composition. The samples were p-type. Annealing after electrodeposition was proved to be useful method to prepare polycrystalline CIS films for solar cell application.⁹⁰ M. E. Calixto et al. performed the Depth profile analysis of CIS thin films grown by the electrodeposition technique. The electrodeposited CIS film had a

Cu-rich bulk region and an In rich surface, which led to the formation of an n-layer ($\text{CuIn}_2\text{Se}_{3.5}$) on the top of the p-type CIS phase.⁹¹ R. Ugarte prepared CIS polycrystalline thin films by electrodeposition on titanium and conducting glass substrates from an aqueous solution containing CuCl_2 , InCl_3 , SeO_2 in a glycine acid medium, pH around 2 adjusted with HCl.⁹² M. C. F. Oliveira et al. performed a voltammetric study of the electrodeposition of CIS in a citrate electrolyte. The electrode reactions occurring on a Mo surface and on a Mo-modified surface, i.e. presenting indium-compound nucleation sites ($\text{Cu}_x\text{In}_y\text{Se}$ or In_ySe) were not the same. The presence of these nucleation sites was responsible for the non-reduction of Cu_xSe on the electrode. The effect of the CIS substrate on the reduction potential of Cu^{2+} , In^{3+} and Se^{4+} in separate citrate solutions was examined. Evidence was given for the copper and indium deposition by a surface-induced deposition mechanism and for the Cu_xSe formation by a co-deposition mechanism.⁹³ J. L. Xu et al. studied the influence of the vacuum annealing process on electrodeposited CIS films. The crystallization of the films was greatly improved by the short time vacuum annealing process without significant change in composition. The capacitance–voltage measurement showed characteristic p-type behaviours. This annealing process after electrodeposition was proved to be a useful method to prepare the polycrystalline CIS films for solar cell application.⁹⁴ M. E. Calixto et al. studied the compositional and optoelectronic properties of CIS and CIGS thin films formed by electrodeposition. As-deposited as well as selenized films exhibited a compact or a granular morphology depending on the composition. The film stoichiometry was improved after selenization at 550°C in a tubular furnace. The films were formed with a mixed phase composition of CIS and $\text{CuIn}_2\text{Se}_{3.5}$ ternary phases.⁹⁵ J. Huang et al. studied the Formation of CIS thin films on flexible substrates by electrodeposition (ED) technique. Ternary compounds were co-deposited on Au coated plastic substrate from an aqueous acidic solution containing 1 mM CuCl_2 , 5 mM InCl_3 and 1 mM SeO_2 adjusted to $\text{pH}=1.65$. It was found that the film stoichiometry improves when the growth solution consisted of 1 M triethanolamine (TEA) and 0.1 M Na-citrate. The optimal ED-CIS film was obtained after annealing at 150°C for 1 h in a nitrogen (N_2) atmosphere. Optical

absorption study showed that the energy gap of the annealed material was 1.18 eV. Good and reliable quality ED-CIS film was grown with the potential use in fabricating flexible solar cells.⁹⁶ K. T. L. De Silva et al. carried out electrodeposition and characterization of CIS for applications in thin film solar cells. Cu composition remained the same within the deposition potentials used in this investigation. The deposited layers were polycrystalline and annealing at 350°C for 30 min improves the crystallinity. The film quality deteriorated due to dissociation when annealed at temperatures above 350°C. Excessive annealing resulted in a surface which was depleted in Cu and rich in In and Se.⁹⁷ C. Guillen et al. studied the recrystallization and components redistribution processes in electrodeposited CIS thin films. The obtained data reveal the importance of oxygen interaction with CIS layers at temperatures above 400°C, by resulting in a crystalline In₂O₃ phase which remains in the film near-surface region and a poor crystalline Cu_xSe which migrates towards the bulk. Such components redistribution allows overall stoichiometric layers to approach the characteristics of global Cu-rich ones and achieve the highest CIS recrystallization.⁹⁸ J. Kois et al. carried out Electrodeposition of CIS thin films onto Mo-glass substrates. It was found that the value of indium and copper ratio (In/Cu) in the films electrodeposited in the potentials area from -0.2 to -0.6 V (vs. SCE) was independent of the concentration ratio of Cu²⁺/In³⁺. At the same time, the concentration of Indium in the films obtained was determined both by the deposition potential and the ratio of Se(IV)/Cu²⁺ in the solution.⁹⁹

(iii) Electroless deposition

P. J. Sebastian et al. studied the Formation of CIS thin films by selenization, employing CVTG, of electroless deposited Cu-In alloy. This process consisted of Cu-In alloy deposition by electroless followed by high temperature selenization of the alloy employing CVTG. The alloy phase consisted mainly of Cu₁₁In₉ alloy. Selenization of the alloy at 400°C resulted in the formation of cubic CIS with alpha-Cu₂Se as the secondary phase.¹⁰⁰ Philip A. Jones et al. carried out the plasma enhanced chemical vapour deposition of CIS. Thin films with compositions around the Cu:In:Se stoichiometric ratio 1:12 were grown using a glow discharge enhanced CVD process.¹⁰¹ B Ghosh et al.

introduced a novel back-contacting technology for CIS thin films. Electroless deposition of a Nickel-Molybdenum alloy on chromium-coated glass substrates was carried out.¹⁰² Manjunatha Pattabi et al. carried out preparation and characterization of CIS films by electroless deposition. The deposition bath consisted of aqueous solutions of copper chloride, indium chloride, selenous acid and lithium chloride. The pH of the bath was adjusted to 2.2 by adding dilute HCl. The Mo substrate was short-circuited with the aluminum counter electrode for the electroless deposition.¹⁰³

(iv) Ink coating

G. Norsworthy et al. prepared CIS film by metallic ink coating and selenization. The technique used an ink formulation containing sub-micron size particles of Cu-In alloys. A metallic precursor layer was first formed by coating this ink onto the substrate by spraying. The precursor film was then made to react with Se to form the CIS compound.¹⁰⁴ M. Kaelin et al. prepared CIS and CIGS layers from selenized nanoparticle precursors. The chemical conversion (selenization) of nanosized precursor materials into CIS and Cu(In,Ga)Se₂ compounds and microstructural properties of these layers were investigated. Three categories of nanoparticles, namely metal-oxides, metal-selenides and elemental metal particles were selenized in selenium vapour. Using two different reactor designs, the influence of the selenium vapour pressure was investigated. While oxide and selenide precursors showed limited sintering and chemical conversion, dense CIS layers with large grains (1–2 μm) were obtained with metal precursors.¹⁰⁵

(v) Chemical Spray Pyrolysis (CSP)

Tomoaki Terasako et al. studied the structural and optical properties of In-rich Cu-In-Se polycrystalline thin films prepared by chemical spray pyrolysis. Structural and optical properties of In-rich Cu-In-Se polycrystalline thin films ($0.54 < \text{In}/(\text{Cu}+\text{In}) < 0.78$) prepared by chemical spray pyrolysis (CSP) on glass substrate were systematically studied in terms of In/(Cu+In) ratio. Lattice constants *a* and *c* of the films decreased with increase of In/(Cu+In) ratio. The films exhibited a characteristic Raman peak shifting higher frequencies as the In/(Cu+In) ratio increases. Optical band gap energy was

approximately 1.22 eV for $0.54 < \text{In}/(\text{Cu}+\text{In}) < 0.67$, but increased from 1.22 to 1.36 eV when the $\text{In}/(\text{Cu}+\text{In})$ ratio increased from 0.67 to 0.78. Photo acoustic measurements revealed the existence of high concentration of non-radiative centers introduced by the deviation from the stoichiometric composition.¹⁰⁶ Tomoaki Terasako analyzed the three-stage growth of Cu–In–Se polycrystalline thin films by chemical spray pyrolysis. The films grown at substrate temperature (T_s) of 420 °C exhibited larger grains in comparison with the Cu–In–Se films grown by the usual CSP method. Optical gap energy was approximately 1.06 eV for 360 °C and 420 °C, but increased dramatically from 1.06 to 1.35 eV when the substrate temperature rose from 420 to 500 °C. Conductivity type was p for $T_s < 420$ °C, but n for $T_s > 420$ °C.¹⁰⁷ It is obvious that, in this technique band gap can be increased upto 1.36eV without alloying Al, Ga or Sulfur.

(vi) Metal Organic Chemical Vapour Deposition (MOCVD)

Seok Hwan Yoon et al. prepared CIS thin films through MOCVD using di- μ -methylselenobis(dimethylindium) and bis(ethylisobutyrylacetato) copper(II) precursors. First, phase pure InSe thin film was prepared on molybdenum substrate by using a single-source precursor, di- μ -methylselenobis(dimethylindium). Second, on this InSe/Mo film, bis(ethylisobutyrylacetato) copper(II) designated as $\text{Cu}(\text{eiac})_2$ was treated by MOCVD to produce CIS films. The thickness and stoichiometry of the product films were found to be easily controlled in this method by adjusting the process conditions. Also, there were no appreciable amounts of carbon and oxygen impurities in the prepared CIS films.¹⁰⁸

(vii) Successive Ionic Layer Absorption and Reaction (SILAR)

Yong Shi et al. studied the effects of post-heat treatment on the characteristics of chalcopyrite CIS film deposited by SILAR method. XRD results showed that the proper post-annealing process can lead to a complete formation of chalcopyrite structure CIS with high degree of preferred orientation towards (112) reflection. After annealing process, the composition of annealed films was close to the standard stoichiometry and O, Cl impurities decreased. The direct band gap increased from 0.94 to 0.98 eV and resistivity showed a big decrease with the increase of annealing temperature.¹⁰⁹ Jingxia

Yang et al. investigated the effect of cationic precursor solutions on formation of CIS thin films by SILAR method. SILAR deposition of CIS films was performed by using Cu^{2+} -TEAH₃ (Cupric chloride and triethanolamine) and In^{3+} -CitNa (Indium chloride and sodium citrate) chelating solutions with weak basic pH as well as Na_2SeSO_3 solution at 70 °C. Well-crystallized, smoothly and distinctly particular CIS films could be obtained after annealing in Ar at 400 °C for 1 h by using the mixed cationic solution mode.¹¹⁰

1.15.3 Defect studies

Defect plays an important role in governing the opto-electronic properties of CIS. Defect analysis was mainly done using Photoluminescence and temperature dependant conductivity studies.

C.Rincon et al. made studies on luminescence and impurity states in n-type CIS and three peaks were observed at 0.98eV, 0.99eV and 1.013eV. The main peak at 0.98eV was due to the donor-acceptor pair recombination. Peak at 1.013eV was due to Se vacancy and at 0.99eV due to In vacancy. Acceptor ionization energy was 33 ± 2 meV and donor ionization energy was 10 ± 2 meV.¹¹¹ S Zott et al. identified the observed luminescence as due to the donor-acceptor pair transition including the acceptor V_{Cu} and two donors V_{Se} and In_{Cu} from excitation-intensity and temperature dependant measurements.¹¹² J. H. Schön et al. demonstrated sharp transitions for Cu-rich films compared to broad emission lines for In-rich materials. Cu-rich materials were characterized by four relatively sharp emission lines at 1.036 eV, 0.993 eV, 0.971 eV and 0.942 eV at 6 K. As the composition was gradually changed from Cu rich to stoichiometric compositions only one broad emission line could be observed at 0.964 eV, which corresponds to a donor-acceptor pair transition. In the case of In-rich material (Cu/In atomic ratio=0.3–0.6), three dominant transitions were observed at 1.10 eV, 0.975 eV, and 0.89 eV. The observed spectra are explained by considering the formation energies of the defects and the composition of the specific film.¹¹³ O. Ka et al. investigated post-growth Cu-diffusion in In-rich CIS films through photoluminescence and explained a transition from the commonly observed broad band around 0.94 eV to a much sharper peak around 0.985 eV under low excitation

density. This recombination appeared at a slightly but definitely larger energy than the recombination usually reported around 0.96 eV. The excitation power dependence led to ascribe the peak observed to a donor–acceptor be $[\text{Cu}_{\text{In}}-\text{Cu}_i]$ pair band, as evidenced by the 2.5 meV/decade shift of the peak-energy and the temperature-dependence of the photoluminescence signal.¹¹⁴ S. Niki et al. studied the anion vacancies in CIS. The presence of the Cu–Se surface phase, the post-growth air-annealing and the Na incorporation all provided significant changes in photoluminescence spectra. Decrease in positron lifetime and reduction of twin density were found to occur simultaneously, along with the changes in photoluminescence spectra. Change in photoluminescence spectra and the corresponding decrease in positron lifetime indicated the annihilation of Se-vacancies; the control of Se-vacancy is a key issue to be addressed for improving the electrical, optical and structural properties of CIS films.¹¹⁵

Shigeru Niki et al. measured the photoluminescence of CIS film prepared using molecular beam epitaxy. PL spectra of Cu-rich CIS epitaxial films showed well-defined emission lines. A broad peak at $\lambda = 1.45 \mu\text{m}$ became dominant in In-rich films, and excitation power dependence of such a broad emission indicated a pair-type radiative recombination, most likely the emission due to donor-acceptor pair or their complex.¹¹⁶

K. Timmo et al. studied the effect of sodium doping to CIS monograin powder properties. Sodium was added in controlled amounts from $5 \times 10^{16} \text{ cm}^{-3}$ to $1 \times 10^{20} \text{ cm}^{-3}$. The photoluminescence spectra of Na-doped stoichiometric CIS powders had two bands with peak positions at 0.97 and 0.99 eV. The photoluminescence bands showed the shift of peak positions depending on the Na doping level. Peak positions with maximum energy were observed if added sodium concentration was $1 \times 10^{19} \text{ cm}^{-3}$. This material had the highest carrier concentration $2 \times 10^{17} \text{ cm}^{-3}$. In the case of stoichiometric CIS (Cu:In:Se = 25.7:25.3:49.0), Na doping at concentrations of $3 \times 10^{17} \text{ cm}^{-3}$ and higher avoided the precipitation of Cu–Se phase. Solar cells output parameters were dependent on the Na doping level. Sodium concentration $3 \times 10^{18} \text{ cm}^{-3}$ resulted in the best open-circuit voltage.¹¹⁷ K. Puech et al determined minority carrier lifetimes in CIS thin films. Luminescence at two distinct spectral positions was observed: A high energy emission.

attributed to free carrier or free exciton recombination (depending on composition), that decayed extremely fast with a lifetime of tens of picoseconds to a few nanoseconds; a lower energy emission from defect related recombination that decayed much more slowly, with typical lifetimes greater than tens of nanoseconds.¹¹⁸

R. Trykozko studied photoelectrical properties of CIS thin films prepared using flash evaporation and beam evaporation. Films showed p-type conductivity. Activation energy of photoconductivity did not exceed 30 meV. But in the dark conductivity curve, there were two regions with activation energies of 81 and 190 meV respectively. These were attributed to an acceptor level due to In vacancies or interstitial Se.¹¹⁹ Wasim et al. prepared CIS from vacuum fusion of the stoichiometric mixture of highly pure elements. Both n and p-type samples were prepared. Three donor levels at 8, 80 and 180 meV were attributed to In_{Cu} , V_{Se} and In_i respectively. The acceptor levels around 30, 80 and 400 meV were due to V_{Cu} , V_{In} or Cu_{In} and $\text{Fe}^{2+}_{\text{In}}$ respectively.¹²⁰ Datta et al. calculated activation energies from TSC measurements. They obtained three energy levels 35, 45 and 100 meV and were associated with intrinsic defects. Room temperature resistivity was $10^5 \Omega\text{cm}$.¹²¹ Masayuki et al. studied photoluminescence of CIS films prepared using selenization technique with solid or vapour-phase selenium. PL spectra could be explained by the levels: the donor level of Se vacancy (V_{Se}), 70 meV below the conduction band, the acceptor levels of the copper vacancy (V_{Cu}), 40 meV and 85 meV above the valence band, the In vacancy (V_{In}) 40 meV above the valence band and copper on the antisite at indium (Cu), 40 meV above the valence band.¹²² J. H. Schön et al. carried out a comparison of point defects in CIS and CuGaSe_2 single crystals grown by chemical vapour transport. V_{Cu} and V_{Se} showed similar properties and activation energies in both materials. Ga_{Cu} levels in CuGaSe_2 are much deeper than In_{Cu} in CIS, and furthermore, the formation of In_{Cu} is much easier compared to Ga_{Cu} .¹²³ A. V. Mudryi et al. carried out optical characterization of high-quality CIS thin films synthesized by two-stage selenization process. For near stoichiometric films, intense band-to-band recombination generated a room temperature PL peak at 1.028 eV with full width at half maximum (FWHM) of approximately 50 meV. At 78 K, the A and B free exciton peaks

appeared, in both PL and OA spectra, merged into a band at approximately 1.044 eV. The 4.2 K-PL spectrum contains a number of features. The A and B excitonic peaks shift to 1.0409 eV (A) and 1.0444 eV (B) and were well resolved in both the PL and OA spectra, with their FWHM reduced to 2.5 meV. Their spectral positions and FWHM are approaching those in high quality CIS single crystals.¹²⁴

M. V. Yakushev et al. studied the effects of deviation from stoichiometry on excitons in CIS single crystals. The Cu/In ratio of the crystals varied from 0.8 to 1.2. At 4.2 K free-exciton peaks A and B as well as a number of bound-exciton peaks were observed well resolved in the PL spectra. Deviations from Cu/In=1 resulted in shifts of the free-exciton peaks to lower energy and an increase in their full width at half maximum. The A-B separation energy was found to be strongly influenced by the Cu/In ratio and temperature suggesting that the valence band B is less sensitive to the tetragonal distortion in the lattice than the uppermost valence band A.¹²⁵ N. Rega et al. analyzed the defect spectra in epitaxial CIS grown by MOVPE on GaAs (0 0 1) wafers. The photoluminescence spectra for p-type Cu-rich ([Cu]/[In]>1.05) CIS were dominated by one donor acceptor pair transition at 0.972 eV. For slightly Cu-poor and stoichiometric samples a free to bound transition at 0.992 eV is observed. Also an exciton emission could be detected at $E_{FX}=1.032$ eV indicating a band gap of $E_g=1.038$ eV at 10 K. These results could be combined in a defect model for CIS containing two acceptors states with 40 and 60 meV and a compensating 6 meV donor state.¹²⁶ A. V. Mudryi et al. studied the free and bound exciton emission in CIS. New values were determined for the band gap energy $E_g=1.0459$ eV and for the excitonic binding energy 5.1 meV in CIS at 4.2 K.¹²⁷ Zeenath et al. studied the trap levels of p-type CIS samples. As prepared samples had two trap levels of activation energies 70.72 meV and 40.5 meV due to presence of Se vacancy and Cu vacancy. For vacuum annealed samples, activation energies of 70.29 meV and 414 meV were obtained due to the existence of Se vacancy and Fe impurity. In the case of air annealed samples 40.5 meV and 103 meV were obtained due to Cu vacancy.¹²⁸ Joehen Klais et al. performed calculation and experimental characterization of the defect physics

in CIS. This led to the assumption that the single defects V_{Se} , V_{Cu} , Cu_{In} and the defect pair ($2V_{Cu}-In_{Cu}$) occur in the investigated specimens in considerable concentrations.¹²⁹

Table 1.4: Defect activation energies

Defect	Activation energy (meV)
V_{In}	33, 40
In_{Cu}	8
V_{Se}	80, 70
In_i	180
V_{Cu}	30, 40, 85
Cu_{In}	80
Fe^{2+}_{In}	400

Table 1.4 gives a summary of the activation energy of the defects mainly observed in $CuInSe_2$ thin films, derived from the above review.

1.15.4 Effects of Na and O

Incorporation of Na and O was found to produce beneficial effects in CIS solar cells, by passivating grain boundaries and increasing conductivity. Hence the effect of Na and O on CIS has been the subject of study of many researchers.

Su-Huai Wei et al. studied the effect of Na on the electrical and structural properties of CIS. It was showed that the main effect of sodium, either via direct substitution $Na_{In_{Cu}}$ or via the release of oxygen radicals and the subsequent $O_{V_{Se}}$ occupation, was to reduce intrinsic donor defects in CIS. When Na concentration was small, Na first eliminated In_{Cu} defects, thus increased the effective hole densities. As the Na concentration increases to the level that most of the In_{Cu} defects have already been eliminated, it will start to remove the acceptor V_{Cu} , therefore reduces the hole density.¹³⁰ David W Niles et al., observed the Na and O impurities at grain surfaces of CIS. It was proved that Na and O reside at grain surfaces and not in the grain interiors of CIS and improved the efficiency of CIS solar

cells.¹³¹ Ryuhei Kimura et al. studied the photoluminescence properties of sodium incorporation in CIS and CuIn_3Se_5 thin films. Enhanced grain growth and preferred (1 1 2) grain orientation as well as a decrease in resistivity with respect to undoped films were observed with sodium incorporation. Compensation was reduced due to the suppression of donor-type defects by the presence of Na.¹³² Yoshinori Nagoya, studied the role of sulfur incorporation into the surface of $\text{Cu}(\text{InGa})\text{Se}_2$ thin film absorber. The incorporated S was concluded to be elective to improve the p-n heterojunction quality due to the passivation of surface and grain boundary of CIGS absorber through the formation of a thin CIGSS surface layer.¹³³

Table1.5: Properties of CIS.¹¹

Formula	CuInSe_2
Molecular weight	336.28
Density	5.77g/cm^3
Colour	Grey
Transition to sphalerite structure	810°C
Melting temperature	986°C
Symmetry	Chalcopyrite
Space group	$I42d - D_{2d}^{12}$
Lattice parameters	
a	5.789\AA
c	11.62\AA
Thermal expansion co-efficient(at 273K)	
(a axis)	$8.32 \times 10^{-6} \text{K}^{-1}$
(c axis)	$7.89 \times 10^{-6} \text{K}^{-1}$
Thermal conductivity	$0.086 \text{ W cm}^{-1}\text{K}^{-1}$
Specific heat	
C1	$7.67 \times 10^{-1} \text{K}^{-1}$

C2	$4.06 \times 10^{-6} \text{ K}^{-2}$
C3	$4.3 \times 10^{-9} \text{ K}^{-3}$
Debye temperature	221.9 K
Microhardness(112 face)	$3.2 \times 10^9 \text{ N/m}^2$
Compressibility	$1.4 \times 10^{-11} \text{ m}^2 \text{ N}^{-1}$
Dielectric constant	
Low frequency	13.6 ± 2.4
High frequency	8.1 ± 1.4
Sound velocity (longitudinal)	$2.2 \times 10^5 \text{ cms}^{-1}$
Electrical resistivity(polycrystalline films)	
Cu-rich	$0.001 \Omega \text{ cm}$
In-rich	$> 100 \Omega \text{ cm}$
Mobility	
Electrons ($n = 10^{14} - 10^{17} \text{ cm}^{-3}$)	$100-1000(\text{at } 300\text{K}) \text{ cm}^2 \text{ V}^{-1} \text{ s}^{-1}$
Holes ($p = 8 \times 10^{15} - 6 \times 10^{16} \text{ cm}^{-3}$)	$50-180 (\text{at } 300\text{K}) \text{ cm}^2 \text{ V}^{-1} \text{ s}^{-1}$
Effective mass	
Electrons	$0.09 m_e$
Holes (heavy)	$0.71 m_e$
(light)	$0.092 m_e$
Energy gap (In-rich polycrystalline films)	1.02 eV
Temperature dependence of gap dE_g/dT (77-300 K)	$-2 \pm 1 \times 10^{-4} \text{ eV K}^{-1}$
Pressure dependence of gap dE_g/dP	$2.8 \times 10^{-11} \text{ eV Pa}^{-1}$

References

- 1 Thin Film Solar Cells, Kasturi Lal Chopra and Suhit Ranjan Das, Plenum press, New York, (1983)
- 2 Physics of Solar Cells, Jenny Nelson, Imperial College Press, London (2003)
- 3 Solar Cells and Their Applications, Larry D Partain, Wiley Interscience, New York (1996)
- 4 Martin A. Green, Keith Emery, Yoshihiro Hishikawa, Wilhelm Warta, *Prog. Photovolt: Res. Appl.* **16** (2008)435
- 5 www.nrel.gov.in
- 6 R R King, D C Law, K M Edmondson, C M Fetzer, G S Kinsey, H Yoon, R A Sherif, N H Karam, *Applied Physics Letters* **90** (2007)183516
- 7 Kyong Kon Kim, Jiwen Liu, Manoj Namboothiry, David L. Carroll, *Appl. Phys. Lett.* **90**, 163511 (2007).
- 8 Yu Ba, Yiming Cao, Jing Zhang, Mingkui Wang, Renzhi Li, Peng Wang, Shaik M. Zakeeruddin & Michael Grätzel, *Nature Materials*, doi:10.1038/nmat2224 (2008)
- 9 Photovoltaic Materials, Richard H Bube, Imperial College Press, London (1998)
- 10 Practical Hand Book of Photovoltaics, Tom Makvart and Luis Castaner, Elsevier, UK, 2003
- 11 A. Rockett, FL W. Birkmire, *J. Appl. Phys.* **70** (7) (1991) R81
- 12 Bülent M. Basol, Vijay K. Kapur, Arvind Halani, Craig Leidholm, *Solar Energy Materials and Solar Cells*, **29**(2) (1993)163
- 13 Bülent M. Basol, Vijay K. Kapur, Craig R. Leidholm, Arvind Halani, Kristen Gledhill, *Solar Energy Materials and Solar Cells*, **43**(1) (1996) 93
- 14 M. A. Martínez, C. Guillén, A. Morales, J. Herrero, *Surface and Coatings Technology*, **148**(1) (2001) 61
- 15 C. J. Huang, T. H. Meen, M. Y. Lai, W. R. Chen, *Solar Energy Materials and Solar Cells*, **82**(4) (2004) 553
- 16 D. Spemann, R. Deltschew, M. Lorenz, T. Butz, *Nuclear Instruments and Methods in Physics Research Section B: Beam Interactions with Materials and Atoms*, **219-220** (2004) 693
- 17 H. Neumann, E. Nowak, B. Schumann, G. Kuhn. *Thin Solid Films*, **74** (1980) 197
- 18 Neelkanth.G.Dhere, M.Cristina Lorenzo, Ramesh G.Dhere, Lawrence L.Kazmerski, *solar cells*, **13** (1984) 59
- 19 M.Varela, J.L.Morenza, J.Esteve, J.M.Codina, *J.Phys.D: Appl.Phys.***17** (1984) 2423

- 20 Mikihiko Nishitani, Takayuki Negami, Masaharu Terauchi, Takashi Hirao *Jpn.J.Appl.Phys.* **31** (1992) 192
- 21 S. T. Lakshmikumar, A. C. Rastogi, *Solar Energy Materials and Solar Cells*, Volume **32**(1), (1994) 7
- 22 C.Guillen,J.Herrero, *Solar Energy Materials and Solar Cells* **73** (2002)
- 23 C Calderon, G Gordillo, E Romero, W Bolanos and P Bartolo-Perez, *phys.stat.sol(b)* **242**, No.9 (2005) 1910
- 24 Mario Gossila, William N Shafarman, *Thin Solid Films* **480-481**(2005)33
- 25 Sung Chan Park, Se Han Kwon, Jin Soo Song, Byung Tae Ahn, *Solar Energy Materials and Solar Cells* **50**(1-4) (1998) 43
- 26 T Schlenker, H W Schock, J H Werner, *Journal of Crystal Growth* **259** (2003)47
- 27 M J Romero, K M Jones, J AbuShama, Y Yan, M M Al-Jassim, R Noufi, *Appl.Phys.Lett* **83**(4731)
- 28 Akhlesh Gupta, Sho Shirakata, Shigehiro Isomura, *Solar Energy Materials and Solar Cells*, **32**(2) (1994) 137
- 29 S. I. Castañeda, F. Rueda, *Thin Solid Films* **361-362** (2000) 145
- 30 A H Moharram, I M Al-Mekawy, A Salem, *Applied Surface Science* **191**(2002) 85
- 31 O Rodriguez, W Bolanos, G Gordillo, *phys.stat.sol(a)* **201**, No.10 (2004) 2381
- 32 A. Ashour, A. A. S. Akl, A. A. Ramadan, K. Abd EL-Hady, *Thin Solid Films* **467**(1-2) (2004) 300
- 33 C. Guillén, J. Herrero, *Solar Energy Materials and Solar Cells* **73**(2) (2002) 141
- 34 F. Kurdesau, M. Kaelin, V. B. Zaleski, V. I. Kovalevsky, V. F. Gremenok, E. P. Zaretskaya, A. N. Tiwari, *Thin Solid Films* **451-452** (2004) 245
- 35 A. G. Chowles, J. A. A. Engelbrecht, J. H. Neethling, C. C. Theron, *Thin Solid Films* **361-362** (2000) 93
- 36 A. Brummer, V. Honkimäki, P. Berwian, V. Probst, J. Palm, R. Hock, *Thin Solid Films* **437**(1-2) (2003) 297
- 37 R. Caballero, C. Guillén, *Solar Energy Materials and Solar Cells* **86**(1) (2005)1
- 38 M.A. Contreras, K. Ramanathan, J. AbuShama, F. Hasoon, D.L. Young, B. Egaas, and R. Noufi 2005 *Prog. Photovolt: Res. Appl.* **13** 209
- 39 C.M.Joseph, C.S.Menon, *J.Phys.D.Appl.Phys.* **34** (2001) 1143
- 40 A.A.S.Akl, A.Ashour, A.A.Ramadan, K.Abd El-Hady, *Vacuum* **61** (2001) 75

- 41 M. Klenk, O. Schenker, V. Alberts, E. Bucher, *Thin Solid Films* **387**(1-2) (2001) 47
- 42 C. Guillen, J. Herrero, *Vacuum* **67** (2002) 659
- 43 I. Martil, J. Santamaria, E. Iborra, G. Gonzalez-Diaz, F. Sanchez-Quesada, *J. Appl. Phys.* **62**(10) (1987), 4163
- 44 P. Menna, A. Parretta, M. Pellegrino, L. Quercia, M. L. Addonizio, *Solar Energy Materials and Solar Cells*, Volume **35** (1994) 165
- 45 Sang Deok Kim, Hyeong Joon Kim, Frederick Ojo Adurodija, Kyeong Hoon Yoon, Jinsoo Song, *Journal of the Korean Physical Society* **35** (1999) S403
- 46 J. Schmidt, H. H. Roscher, R. Labusch, *Thin Solid Films*, **251**(2) (1994) 116
- 47 F. O. Adurodija, S. K. Kim, S. D. Kim, J. S. Song, K. H. Yoon, B. T. Ahn, *Solar Energy Materials and Solar Cells* **55**(3) (1998) 225
- 48 Tooru Tanaka, Toshiyuki Yamaguchi, Akihiro Wakahara, Akira Yoshida, *Thin Solid Films* **343-344** (1999) 320
- 49 Tooru Tanaka, Toshiyuki Yamaguchi, Akihiro Wakahara, Akira Yoshida, Ryoichi Taniguchi, Yatsuka Matsuda, Masatoshi Fujishiro, *Solar Energy Materials and Solar Cells* **75**(1-2) (2003) 115
- 50 J. Müller, J. Nowoczin, H. Schmitt, *Thin Solid Films* **496**(2) (2006) 364
- 51 A. Yoshida, N. Tanahashi, T. Tanaka, Y. Demizu, Y. Yamamoto, T. Yamaguchi, *Solar Energy Materials and Solar Cells* **50**(1-4) (1998) 7
- 52 V. V. Kindyak, A. S. Kindyak, V. F. Gremenok, A. A. Kutas, *Thin Solid Films*, **240**(1-2) (1994) 114
- 53 S. Kuranouchi, A. Yoshida, *Thin Solid Films* **343-344** (1999) 123
- 54 A. Tverjanovich, E.N. Borisov, E.S. Vasilieva, O.V. Tolochko, I.E. Vahhi, S. Bereznev, Yu.S. Tveryanovich, *Solar Energy Materials and Solar Cells* **90**(20) (2006) 3624
- 55 W. Riedl, J. Rimmasch, V. Probst, F. Karg, R. Guckenberger, *Solar Energy Materials and Solar Cells*, **35** (1994) 129
- 56 V. Alberts, J. H. Schon, E. Buzher, *Journal of Applied Physics* **84**(12) (1998)
- 57 J. Keränen, J. Lu, J. Barnard, J. Sterner, J. Kessler, L. Stolt, Th. W. Matthes, E. Olsson, *Thin Solid Films* **387**(1-2) (2001) 80
- 58 S. Niki, I. Kim, P. J. Fons, H. Shibata, A. Yamada, H. Oyanagi, T. Kurafuji, S. Chichibu, H. Nakanishi, *Solar Energy Materials and Solar Cells* **49**(1-4) (1997) 319

-
- 59 K. Yoshino, T. Shimizu, A. Fukuyama, K. Maeda, P. J. Fons, A. Yamada, S. Niki, T. Ikari, *Solar Energy Materials and Solar Cells* **50**(1-4) (1998) 127
- 60 A. N. Tiwari, M. Krejci, F. -J. Haug, H. Zogg, *Thin Solid Films* **361-362** (2000) 41
- 61 James H. Ely, T. R. Ohno, T. E. Furtak, A. J. Nelson, *Thin Solid Films* **371**(1-2) (2000) 36
- 62 Tooru Tanaka, Toshiyuki Yamaguchi, Takeshi Ohshima, Hisayoshi Itoh, Akihiro Wakahara, Akira Yoshida, *Solar Energy Materials and Solar Cells* **75** (2003) 109
- 63 A. Zegadi, M.V. Yakushev, E. Ahmed, R.D. Pilkington, A.E. Hill, R.D. Tomlinson, *Solar Energy Materials and Solar Cells* **41-42** (1996) 295
- 64 168 C.H.Champness, I.Shilh, H.Du, *Thin Solid Films* **431-432** (2003) 68
- 65 H. P. Wang, I. Shih, C. H. Champness, *Thin Solid Films* **361-362** (2000) 494
- 66 C. H. Champness, G. I. Ahmad, *Thin Solid Films* **361-362** (2000) 482
- 67 K. Timmo, M. Altosaar, M. Kauk, J. Raudoja, E. Mellikov, *Thin Solid Films* **515**(15) (2007) 5884
- 68 Fabrication of CIS/CdS Thin Film Solar Cells By Chemical Bath deposition Technique and Characterization, Ph.D.Thesis, P.K.Vidyadharan Pillai, Cochin University of Science and Technology, March1997
- 69 K Bindu, C Sudha Kartha, K P Vijayakumar, T Abe, Y Kashiwaba, *Solar Energy Materials and Solar Cells* **79**(2003) 67
- 70 34 Pankaj Garg, Archana Garg, A C Rastogi and J C Garg, *J. Phys. D: Appl. Phys.* **24** (1991) 2026
- 71 N Khare, G Razzini, L Peraldo Bicelli, *Solar cells* **31**(1991)283
- 72 S. R. Kumar, R. B. Gore, R. K. Pandey, *Solar Energy Materials and Solar Cells*, **26**(1992)149
- 73 A. N. Molin, A. I. Dikumar, *Thin Solid Films* **237**(1-2) (1994) 72
- 74 H. P. Fritz, P. Chatziagorastou, *Thin Solid Films*, **247**(1) (1994) 129
- 75 R. Pal, K. K. Chattopadhyay, S. Chaudhuri, A. K. Pal, *Thin Solid Films*, **247**(1) (1994) 8
- 76 S. Jost, R. Schurr, F. Hergert, R. Hock, J. Schulze, A. Kirbs, T. Voß, M. Purwins, J. Palm, I. Mys, *Solar Energy Materials and Solar Cells* **92**(4) (2008) 410
- 77 S. Nakamura, S. Sugawara, A. Hashimoto, A. Yamamoto, *Solar Energy Materials and Solar Cells* **50**(1-4) (1998) 25
- 78 Shalini Menezes, *Appl.Phys.Lett.* **61** (13) (1992)
- 79 C. Guillen, J. Herrero, *Solar Energy Materials and Solar Cells* **43**(1) (1996) 47
- 80 P.P. Prosini, M.L. Addonizio, A. Antonaia, S. Loreti, *Thin Solid Films*, **288**(1-2) (1996) 90

- 81 S.N. Qiu, C.X. Qiu, I. Shih, *Applied Surface Science* **92** (1996) 306
- 82 81 A. M. Fernandez, P. J. Sebastian, M. E. Calixto, S. A. Gamboa, O. Solorza, *Thin Solid Films* **298** (1-2) (1997) 92
- 83 A.M.Fernandez, P.J.Sebastian, M.E.Calixto, S.A.Gamboa, O.Solorza, *Thin Solid Films* **298** (1997) 92
- 84 E. Tzvetkova, N. Stratieva, M. Ganchev, I. Tomov, K. Ivanova, K. Kochev, *Thin Solid Films*, **311**(1-2) (1997) 101
- 85 N. Stratieva, E. Tzvetkova, M. Ganchev, K. Kochev, I. Tomov, *Solar Energy Materials and Solar Cells* **45**(1) (1997) 87
- 86 R. P. Raffaele, J. G. Mantovani, R. Friedfeld, *Solar Energy Materials and Solar Cells* **46**(3) (1997) 201
- 87 A. M. Fernandez, M. E. Calixto, P. J. Sebastian, S. A. Gamboa, A. M. Hermann, R. N. Noufi, *Solar Energy Materials and Solar Cells* **52**(3-4) (1998) 423
- 88 A.A.I.Al-Bassam,*Physica B* **266** (1999) 192
- 89 L. Zhang, F. D. Jiang, J. Y. Feng, *Solar Energy Materials and Solar Cells* **80**(4) (2003) 483
- 90 J.L Xu,X.F.Yao,J.Y.Feng, *Solar Energy Materials and Solar Cells* **73** (2002) 203
- 91 M. E. Calixto, P. J. Sebastián, *Solar Energy Materials and Solar Cells* **63**(4) (2000) 335
- 92 R. Ugarte, R. Schrebler, R. Córdova, E. A. Dalchiele, H. Gómez. *Thin Solid Films* **340**(1-2) (1999) 117
- 93 M. C. F. Oliveira, M. Azevedo, A. Cunha, *Thin Solid Films* **405**(1-2) (2002) 129
- 94 J. L. Xu, X. F. Yao, J. Y. Feng, *Solar Energy Materials and Solar Cells* **73**(2) (2002) 203
- 95 M. E. Calixto, P. J. Sebastian, R. N. Bhattacharya, Rommel Noufi, *Solar Energy Materials and Solar Cells* **59**(1-2) (1999) 75
- 96 C. J. Huang, T. H. Meen, M. Y. Lai, W. R. Chen, *Solar Energy Materials and Solar Cells* **82**(4) (2004) 553
- 97 K. T. L. De Silva, W. A. A. Priyantha, J. K. D. S. Jayanetti, B. D. Chithrani, W. Siripala, K. Blake, I. M. Dharmadasa, *Thin Solid Films* **382**(1-2) (2001) 158
- 98 C. Guillén, J. Herrero, *Thin Solid Films* **387**(1-2) (2001) 57
- 99 J. Kois, S. Bereznev, E. Mellikov, A. Öpik, *Thin Solid Films* **511-512** (2006) 420
- 100 P. J. Sebastian, A. M. Fernandez, A. Sánchez, *Solar Energy Materials and Solar Cells*, **39**(1) (1995) 55

- 101 Philip A. Jones, Andrew D. Jackson, Paul D. Lickiss, Richard D. Pilkington, Robert D. Tomlinson, *Thin Solid Films*, **238**(1) (1994) 4
- 102 B Ghosh, D P Chakraborty, M J Carter, *Semiconductor Science and Technology*, **11**(1996) 1358
- 103 Manjunatha Pattabi, P. J. Sebastian, X. Mathew, R. N. Bhattacharya, *Solar Energy Materials and Solar Cells* **63**(4) (2000) 315
- 104 G. Norsworthy, C. R. Leidholm, A. Halani, V. K. Kapur, R. Roe, B. M. Basol, R. Matson, *Solar Energy Materials and Solar Cells* **60**(2) (2000) 127
- 105 M. Kaelin, D. Rudmann, F. Kurdesau, T. Meyer, H. Zogg, A. N. Tiwari, *Thin Solid Films* **431-432** (2003) 58187
- 106 Tomoaki Terasako, Yuji Uno, Tetsuya Kariya, Sho Shirakata, *Solar Energy Materials and Solar Cells* **90** (3) (2006) 262
- 107 Tomoaki Terasako, Seiki Inoue, Tetsuya Kariya, Sho Shirakata, *Solar Energy Materials and Solar Cells* **91**(12) (2007)1152
- 108 Seok Hwan Yoon, Kook Won Seo, Seung Soo Lee, Il-Wun Shim, *Thin Solid Films* **515**(4) (2006)1544
- 109 Yong Shi, Zhengguo Jin, Chunyan Li, Hesong An, Jijun Qiu, *Thin Solid Films* **515**(7-8) (2007) 3339
- 110 Jingxia Yang, Zhengguo Jin, Tongjun Liu, Chengjie Li, Yong Shi, *Solar Energy Materials and Solar Cells* **92**(6) (2008) 621
- 111 C.Rincon, J.Gonzalez, G.Sanchez Perez, *J.Appl.Phys* **54**(11), 1983
- 112 S Zott, K Leo, M Ruckh, H W Schock, *Appl.Phys.Lett.***68** (8), (1996)
- 113 J. H. Schön, V. Alberts, E. Bucher, *Thin Solid Films*, **301**(1-2) (1997) 115
- 114 O. Ka, H. Alves, I. Dirnstorfer, T. Christmann, B. K. Meyer, *Thin Solid Films* **361-362** (2000) 263
- 115 S. Niki, R. Suzuki, S. Ishibashi, T. Ohdaira, P. J. Fons, A. Yamada, H. Oyanagi, T. Wada, R. Kimura, T. Nakada, *Thin Solid Films*, **387**(1-2) (2001) 129
- 116 Shigeru Niki, Yunosuke Makita, Akimasa Yamada, Akira Obara, Osamu Igarashi, Syunji Misawa, Michihiro Kawai, Hisayuki Nakanishi, Yutaka Taguchi, Noboru Kutsuwada, *Solar Energy Materials and Solar Cells*, **35** (1994) 141
- 117 K. Timmo, M. Altosaar, J. Raudoja, E. Mellikov, T. Varema, M. Danilson, M. Grossberg, *Thin Solid Films* **515**(15) (2007) 5887

- 118 K.Puech, S.Zott, K.Leo, M.Rukh, H.-W.Schock, *Appl.Phys.Lett.* **69**(22) (1996)
- 119 R.Trykozko, R.Bacewicz, J.Filipowicz, *solar cells*, **16**(1986) 35126
- 120 S.M.Wasim *solar cells* **16**(1986) 289
- 121 T.Datta, R.Noufi, S.K.Deb, *J.Appl.Phys.* **59**(5) (1986)
- 122 Masayuki Tanda, Susumu Manaka, Jorge R.Encinas Marin, Katsumi Kushiya, Hideki Sano, Akira Yamada, Makoto Konagi, Kiyoshi Takahashi, *Jpn.J.Appl.Phys.* **31** (1992) L 753
- 123 J. H. Schön, E. Bucher, *Solar Energy Materials and Solar Cells* **57**(3) (1999) 229
- 124 A. V. Mudryi, V. F. Gremenok, I. A. Victorov, V. B. Zalesski, F. V. Kurdesov, V. I. Kovalevski, M. V. Yakushev, R. W. Martin, *Thin Solid Films* **431-432** (2003) 193183
- 125 M. V. Yakushev, A. V. Mudryi, Y. Feofanov, R. D. Tomlinson, *Thin Solid Films* **431-432** (2003) 190
- 126 N. Rega, S. Siebentritt, I. E. Beckers, J. Beckmann, J. Albert, M. Lux-Steiner, *Thin Solid Films* **431-432** (2003) 186
- 127 A. V. Mudryi, I. V. Bodnar, V. F. Gremenok, I. A. Victorov, A. I. Patuk, I. A. Shakin, *Solar Energy Materials and Solar Cells* **53** (3-4) (1998) 247
- 128 N.A.Zeenath, P.K.V.Pillai, K.Bindu, M.Lakshmi, K.P.Vijayakumar, *Journal of Material Science* **35** (2000) 2619
- 129 Jochen Klais, Hans Joachim Möller, David Cahen, *Thin Solid Films* **361-362** (2000) 446
- 130 Su-Huai Wei, S B Zhang, Alex Zunger, *Journal of Applied Physics* **85**(10), (1999)
- 131 David W Niles, Mowafak Al-Jassim, Kannan Ramanathan, *Jornal of Vac.Sci.Technol.A* **17**(1) (1999) 291
- 132 Ryuhei Kimura, Tokio Nakada, Paul Fons, Akimasa Yamada, Shigeru Niki, Takeo Matsuzawa, Kiyoshi Takahashi, Akio Kunioka, *Solar Energy Materials and Solar Cells* **67**(1-4) (2001) 289
- 133 Yoshinori Nagoya, Katsumi Kushiya, Muneyori Tachiyuki, Osamu Yamase, *Solar Energy Materials and Solar Cells* **67** (2001) 247

2.1 Techniques for CuInSe₂ (CIS) deposition

A wide variety of techniques has been employed in the preparation of CuInSe₂ (CIS) right from the year of 1953. Sputtering¹, Co-evaporation², Chemical Bath Deposition (CBD)³, Chemical Spray Pyrolysis (CSP)⁴, Electrodeposition⁵, Metal Organic Chemical Vapour Deposition (MOCVD)⁶, etc are some of the preparation techniques used in the deposition of polycrystalline CIS, meanwhile Molecular Beam Epitaxy(MBE)⁷, Pulsed Laser Deposition⁸, Bridgeman Growth technique etc are used for preparing single crystalline CIS⁹. Recently a low cost 3D TiO₂/CIS nanocomposite solar cell has been fabricated using electrodeposition with some photovoltaic effect¹⁰. Mean while TiO₂/CuInS₂ nanocomposite solar cell has achieved an efficiency of 5%¹¹. CIS flexible foil solar cells are also available in the market now¹². ISET developed a non-vacuum processing technology for CIGS fabrication in the commercial scale. Process uses water-based inks, made from tiny nanoparticles of Copper, Indium and Gallium oxides as the precursor materials¹³.

The greater efficiency of the solar cells fabricated using polycrystalline CIS has resulted in intensive research works on polycrystalline cells. The most successful method is co-evaporation, through which the record-breaking devices were fabricated. Photovoltaic-grade Cu(In,Ga)Se₂ (CIGS) films have slightly Indium-rich composition. Copper-rich CIGS shows the segregation of Cu_xSe phase, preferentially at the surface of the absorber film. Metallic nature of this phase does not allow the formation of efficient

heterojunctions. Even after the removal of this phase by Potassium Cyanide (KCN) etching, the utility of this material for photovoltaic application is limited. But the importance of Cu-rich composition is pronounced during film growth. Cu-rich films can have grain sizes of the order of $1\mu\text{m}$ whereas In-rich films have much smaller grains. It was observed that CuSe phase is formed on the surfaces and grain boundaries in polycrystalline films, grown under Cu- excess conditions. Presence of solid or liquid Cu_xSe phase, at the surface or within the film, promotes growth of large grains by enhancing diffusion or through the use of a liquid phase epitaxy-like process.¹⁴

The co-evaporation process requires a maximum substrate temperature of 550°C for a certain time during film growth, preferably towards the end of the growth. One of the advantages of the evaporation route is that material deposition and compound formation are performed during the same processing step. A feedback loop, based on a quadrupole mass spectrometer or an atomic absorption spectrometer, controls the rates of each source. The composition of the deposited material with regard to the metals is related to their evaporation rates, while Se is always evaporated in excess. This precise control over the deposition rates allows a wide range of variation and optimization with different sub-steps or stages for film deposition and growth. These sequences are defined by the evaporation rates of the different sources and the substrate temperatures during the course of evaporation. Advanced preparation sequences always include a Cu-rich stage during the growth process and end up with an In-rich overall composition.

Another class of CIGS preparation route is based on the separation of deposition and compound formation into two different processing steps. High efficiencies are obtained from absorber prepared by selenization of metal precursors using H_2Se gas and by rapid thermal processing of the stacked elemental layers in Se atmosphere. These sequential processes have the advantage that large area deposition techniques like sputtering can be used for the deposition of the materials. The very first large area modules were prepared by selenization of metal precursors in the presence of H_2Se .¹⁵

In the present work, CIS samples were prepared using two techniques, Chemical Bath Deposition (CBD) and Physical Vapour Deposition (PVD).

2.1.1 Chemical Bath Deposition (CBD)

CBD technique is probably the simplest and cost-effective of all the deposition techniques. This is a solution growth process used for depositing thin films of compound or elemental materials. The arrangement is very simple, consisting of a beaker containing the solution with the substrates dipped in it. The process is carried out in atmospheric pressure and relatively low temperature. An aqueous solution of a metal complex, when mixed with a solution of chalcogen bearing compound, precipitation of the chalcogenide occurs under certain conditions. When precipitation is controlled, the compound gets deposited on clean substrate or other nucleating centres present in the solution. In the present work this technique was made use of to deposit Selenium film.

Principle

According to solubility product principle, in a saturated solution of a weakly soluble compound, the product of molar concentrations of its ions (each concentration term being raised to a power equal to the number of ions of that kind as shown by the formula of the compound), called the ionic product, is a constant at a given temperature.

Precipitation of solid phase occurs due to super saturation of the reaction bath. At a given temperature, when the ionic product exceeds the solubility product, precipitation occurs. Otherwise the solid phase produced will dissolve back into the solution resulting in no net precipitation. In a typical CBD, substrates are immersed in a solution containing the cations and anions and controlled precipitation leads to formation of thin films.

There are two possibilities for thin film deposition in CBD. One is the ion-ion process in which the ions condense on the substrate surface to form the film. The other is the cluster by cluster process in which colloidal particles of the compound formed in the solution gets adsorbed at the substrate surface to form thin layers. There are many factors, which influence the deposition process viz. nature of reactants, temperature, pH value and concentration of ions, nature of the substrate and duration of reaction.

2.1.2 Vacuum evaporation

Evaporation of material requires that it should be heated to a sufficiently high temperature to produce the desired vapour pressure. Evaporant molecules coming out from the heated source will spread out in all directions. But their velocity distribution will depend on the nature of the source, which can be broadly classified as point source, surface source and cylindrical source. If a source can be approximated to a tiny sphere compared to its distance from the receiving substrate, then the emitted vapour stream will have the same velocity distribution in all directions and hence resembling the emission from a point source. Usually source is assumed to be a point source.

Different techniques are employed to supply heat of vaporization of materials and important ones are the following: resistive heating, flash evaporation, sputtering, electron beam deposition, and laser evaporation. Here we adopted “resistive heating” method. There are several types of practical heating sources made from refractory metals such as tungsten, molybdenum, tantalum etc. We used molybdenum source in the form of a boat.

Material to be evaporated is placed in the boat and is converted in to vapour form by means of resistive heating. The vapour atoms thus created are transported through vacuum of 10^{-5} Torr to get deposited on the substrate. At a steady state of evaporation these vapour atoms or molecules will have an equilibrium vapour pressure (p), which is given by the relation

$$p = \frac{NkT}{V} \quad (2.1)$$

where N is the total number of vapour atoms or molecules V is the volume of the enclosed chamber T is the absolute temperature of the gaseous species and k is Boltzmann's constant.¹⁶ These atoms or molecules in the gaseous state will however collide with one another after a certain mean free time (τ) and the average distance of travel before suffering a collision with another can be expressed by the relations

$$l = \left(\frac{N}{V} \pi \sigma^2 \sqrt{2} \right)^{-1} \quad (2.2)$$

$$l = \frac{kT}{(p \pi \sigma^2 \sqrt{2})} \quad (2.3)$$

where l is the mean free path (mfp) in cm of the vapour species and σ is the conductivity of the film .

From the above relations, it is seen that the lower the equilibrium vapour pressure; the more will be l and when p is very low vapour atoms or molecules will travel a long distance without encountering any collision i.e. these will be moving in a straight path relatively unhindered. This is illustrated for the case of air molecule at low equilibrium pressure. The above equation for air at room temperature can be written as

$$l \approx \frac{5}{p} \text{ (in cm)} \quad (2.4)$$

where p is expressed in micron pressure. Thus in an evacuated system if the residual air pressure at steady states are say 10^{-3} and 10^{-4} torr, then corresponding l will respectively be 5 and 50cm and with lower p , mfp will still be larger. Thus in a highly evacuated system, evaporated atoms or molecules from a heated source will have high l and if l is greater than the length of the enclosed chamber then there will not be any collision of atoms or molecules and these will move unhindered.

Rate of free evaporation of vapour atoms from a clean surface of unit area in vacuum is given by the Langmuir-Dushman kinetic theory equation:

$$N_e = 3.513810^{22} P_e / (MT)^{1/2} \text{ molecules cm}^{-2} \text{ s}^{-1} \quad (2.5)$$

where P_e is the equilibrium vapour pressure (in Torr) of the evaporant under saturated vapour conditions at a temperature T , and M is the molecular weight of the vapour species. Vapour atoms traverse through the medium and are made to condense on a substrate kept at suitable temperature and convenient distance from the evaporant to form a thin film. With increase in substrate temperature, the surface mobility of the adsorbed

species increases and they interact among themselves resulting in well-defined large grains.

2.2 Technique for deposition of In_2S_3 films

In_2S_3 is one of the ideal candidates to replace the toxic CdS in CIS solar cells. Atomic layer epitaxy (ALE)¹⁷, physical vapour deposition¹⁸, chemical bath deposition¹⁹, chemical spray pyrolysis²⁰, MOCVD²¹ and sputtering²² are used for the preparation of In_2S_3 thin films. In the present work, In_2S_3 was prepared using Chemical Spray Pyrolysis.

Chemical Spray pyrolysis (CSP)

Chemical Spray Pyrolysis technique, one of the chemical methods for the preparation of thin films, is widely used to deposit a variety of thin films. It is a simple and low cost technique through which large area deposition is possible with good uniformity. It involves spraying a solution, usually aqueous, containing soluble salts of constituents of the desired compound, onto a heated substrate.

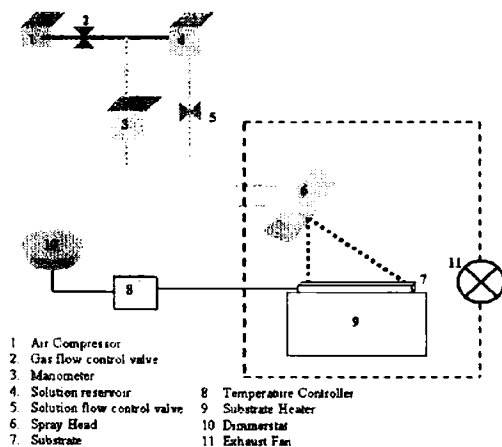


Fig 2.1: Schematic diagram of Spray pyrolysis set up

In CSP technique, it is quite easy to vary the stoichiometry of the film or the doping profile. Stoichiometry can be varied by changing molarity of the solution while dopant concentration in the film can be varied by changing the quantity of dopant dissolved in the solution. These parameters can be varied along film thickness itself.

2.3. Sample preparation

CIS thin films were prepared through two different techniques, viz., selenization of Cu-In alloy using chemical bath deposited Selenium and sequential evaporation. In_2S_3 films were prepared using chemical spray pyrolysis.

2.3.1 Cleaning of substrates

Substrates used were well-cleaned micro glass slides of dimension $2.5 \times 3.75 \times 0.13 \text{ cm}^3$. Procedure for cleaning is as follows. Glass slides were first dipped in freshly prepared hot chromic acid for half an hour, to remove oil content on the glass substrates. Then the slides were washed in running water followed by washing in soap solution (Extran-Neutral). These were again washed in running water and finally the slides were rinsed with distilled water.

2.3.2 Deposition of CIS films using CBD Se layer

Deposition of Se: A stock solution of 0.2M Sodium Selenosulphate (Na_2SeSO_3) is prepared by adding 3.2g of Se powder to aqueous solution of 0.1M excess sodium sulphite (Na_2SO_3) kept at 363K with constant stirring. The chemical reaction can be written as;



or



pH of the as prepared solution is ~ 10 . The 'as- prepared -condition' of the solution was stable for 15 days. Acidification of the above solution resulted in precipitation of Sulfur.

Principle of Se deposition is based on the fact that concentration of sulphites and hence solubility of Selenium depends on pH of the solution. This could be explained as follows. For the above reaction (2.6), equilibrium constant of this reaction is given by,

$$K_{SeSO_3^{2-}} = \frac{[SeSO_3^{2-}]}{[SO_3^{2-}]}$$

Where $[SeSO_3^{2-}]$ and $[SO_3^{2-}]$ are equilibrium concentrations of $SeSO_3^{2-}$ and SO_3^{2-} respectively. Considering hydrolysis of sodium sulphite, the fractional concentration of SO_3^{2-} , $\alpha_{SO_3^{2-}}$ is given by,

$$\alpha_{SeSO_3^{2-}} = \frac{[SO_3^{2-}]}{[H_2SO_3] + [HSO_3^-] + [SO_3^{2-}]} \quad (2.8)$$

$$= \frac{K_{H_2SO_3}}{[H^+]^2 + K_1[H^+] + K_{H_2SO_3}} \quad (2.9)$$

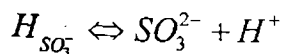
where K_1 is the first dissociation constant of the reaction, $H_2SO_3 \rightleftharpoons HSO_3^- + H^+$ is given by

$$K_1 = \frac{[H_{SO_3^-}][H^+]}{[H_2SO_3]}$$

and $K_{H_2SO_3}$ the total dissociation constant is given by

$$K_{H_2SO_3} = K_1 K_2 \quad (2.10)$$

Where K_2 is the second dissociation constant of the reaction,



and is given by,

$$K_2 = \frac{[SO_3^{2-}][H^+]}{[HSO_3^-]}$$

It is clear that as a result of hydrolysis of Na_2SO_3 , concentration of $[SO_3^{2-}]$ ions is defined not only by concentration of sodium salt in the solution, but also based on the value of

pH. It was found that the concentration of SO_3^{2-} is equal to that of Na_2SO_3 in the solution, only at $pH \geq 10$. Hence if pH of the Na_2SO_3 solution is < 9 , the concentration of SO_3^{2-} is,

$$[SO_3^{2-}] = \alpha_{SO_3^{2-}} \times [Na_2SO_3] \quad (2.11)$$

From the known amount of Na_2SO_3 the equilibrium constant of eqn (2.6), [which expresses the precipitation of Se], becomes,

$$K_{SeSO_3^{2-}} = \frac{[SeSO_3^{2-}]}{[Na_2SO_3] - [SeSO_3^{2-}]} \quad (2.12)$$

From the above equation, the equilibrium concentration of $SeSO_3^{2-}$ can be calculated as,

$$[SeSO_3^{2-}] = \frac{\alpha_{SO_3^{2-}} \times K_{SeSO_3^{2-}}}{1 + \alpha_{SO_3^{2-}} \times K_{SeSO_3^{2-}}} + [Na_2SO_3]$$

This equation gives the solubility of Se in Na_2SO_3 solution of the given concentration.²³

From the above discussion, it can be concluded that the value of pH of the medium to be employed in the synthesis of Na_2SeSO_3 solution should be ≥ 10 . Thus Selenium can be precipitated by reducing the pH of selenosulphate solution to more acidic values.

In order to obtain good film, precipitation was controlled by varying molarity, pH and temperature of the bath containing Na_2SeSO_3 solution. 0.0125M solution was prepared from the 0.2M stock solution. pH of the solution was adjusted to be ~ 4.5 by adding 50% diluted acetic acid to the solution. Bath was then kept at room temperature. Cleaned glass plates were placed vertically in the solution bath and uniform films were obtained after a period of three hour.

In the present work, the sample was subjected to two dips of three hours and then a third dip of two hour. Deposition was carried out in 25ml beaker. At a time, two substrates were kept in the bath with a distance of 2.2cm between them. Films obtained after eight hour deposition were found to be uniform having orange-red colour. Thickness of the film was approximately 2500\AA .²⁴

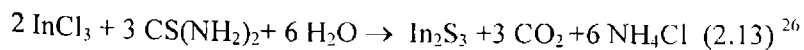
CIS was then prepared by two different methods using the Se films, deposited using CBD technique. In the first process (i.e. SEL technique) Indium and Copper were sequentially deposited on the Se film, using vacuum evaporation and then the samples were annealed in vacuum (at a pressure $\sim 2 \times 10^{-5}$ mbar) at 400°C for one hour. The rate of heating was $2.3^\circ\text{C}/\text{min}$. The second method (i.e. thermal diffusion of Cu into In_2Se_3), had two steps. First step was the deposition of In over the Se layer using vacuum evaporation and annealing of this bilayer film in vacuum at 100°C for one hour to form In_2Se_3 . The second step was to deposit Cu over the In_2Se_3 and anneal in vacuum at 400°C for one hour to get CIS.

2.3.3 CIS using sequential evaporation of elemental layers

CIS films were also prepared by sequential evaporation of Cu, In and Se at a pressure of 10^{-5} mbar. Indium was evaporated first at a substrate temperature of 100°C , followed by deposition of Se at 50°C and finally Cu at room temperature. Rates of deposition were 0.5 nm/sec, 0.3 nm/sec and 0.2 nm/sec for Se, In and Cu respectively. After deposition, the samples were annealed at 400°C for one hour at a pressure of 10^{-5} mbar resulting in the formation of CIS. Here, the heating rate was 1.5°C . The concentration of Cu, In and Se were varied one at a time for optimization.

2.3.4 In_2S_3 using Chemical Spray Pyrolysis

In_2S_3 thin films were deposited by spraying aqueous solutions of Indium chloride (InCl_3) and thiourea ($\text{CS}(\text{NH}_2)_2$), using compressed air as carrier gas. Thiourea was chosen as the source of sulfur ions in spray solution because it avoids precipitation of metallic sulfides and hydroxides.²⁵ The aqueous solutions of these salts were prepared in distilled water. Indium to sulfur ratio in the solution was varied by varying molar concentration of InCl_3 and $\text{CS}(\text{NH}_2)_2$. Formation of In_2S_3 results from the chemical reaction:



Characterization of In_2S_3 was done earlier.²⁰ In the present work the substrate temperature was held constant at $300^\circ\text{C} \pm 5^\circ$. The substrate was kept at this temperature for one hour

before the deposition, for stabilization of the temperature. Volume of the solution was varied to get different thicknesses. Concentration of In_2S_3 was varied for device fabrication.

2.4 Characterization tools Used

2.4.1 X-ray Diffraction (XRD)

X-ray diffraction is the most precise technique for studying crystal structure of solids. Samples can be analyzed using this technique in a non-destructive way. In the X-ray diffractometer, a flat specimen is mounted on a turntable around which moves a detector. As the sample rotates, the angle θ between the incident beam and the sample changes. Whenever the Bragg condition is fulfilled, X-rays are reflected to the detector. The detector is connected to the specimen table and geared in such a way that when the table rotates through θ degrees, the detector rotates through 2θ degrees. This results in the detector always being in the correct position to receive rays reflected by the sample. To record the diffraction pattern, the detector is positioned at or near 0° on the graduated 2θ scale, and then driven by a motor at a constant speed. The X-rays reaching the detector are registered and displayed on a paper chart recorder as a series of peaks on top of background due to white radiation.

XRD gives whole range of information about crystal structure, orientation, crystallite size, composition defects and stresses in thin films. Experimentally determined data is compared with JCPDS file for standards. The interplanar spacing 'd' can be calculated from the Bragg's formula,

$$2d \sin \theta = n\lambda \quad (2.14)$$

where θ is the Bragg angle, n is the order of the spectrum, λ is the wavelength of X-rays which is equal to 1.5405 \AA .

Using d values, the plane (hkl) can be identified and lattice parameters are calculated using the following relations:

For the tetragonal systems,

$$\frac{1}{d^2} = \frac{h^2 + k^2}{a^2} + \frac{1}{c^2} \quad (2.15)$$

and for hexagonal systems,

$$\frac{1}{d^2} = \frac{4(h^2 + hk + k^2)}{3a^2} + \frac{1}{c^2} \quad (2.16)$$

where a and c are lattice parameters.

The grain size 'L' can be calculated from the Debye-Scherrer formula,

$$L = \frac{k\lambda}{\beta \cos \theta} \quad (2.17)$$

where k is a constant equal to 0.9 and β is the full width at half maximum (FWHM) measured in radians.²⁷

In the present work, XRD measurements were taken using $\text{CuK}\alpha 1$ ($\lambda=1.5405 \text{ \AA}$) radiation and a Ni filter operated at 30 kV (Rigaku (D.max.C) X-ray diffractometer).

2.4.2 Raman Scattering

Raman spectroscopy is a non-destructive and non-contact method used to study vibrational, rotational, and other low-frequency modes in a system. When a light is scattered from the surface of a sample, the scattered light is found to contain mainly wavelengths that were incident on the sample and this is called 'Raleigh scattering'. In addition to this, it contains different wavelengths also with very low intensities that present an interaction of the incident light with material. The interaction of the incident light with optical phonons is called 'Raman scattering' while the interaction with acoustic phonon is called Brillouin scattering.²⁸ If the incident photon imparts part of its energy to the lattice in the form of a phonon, it emerges as a lower-energy photon. This frequency shift is known as Stokes-shifted scattering. When the photon absorbs a phonon and emerges with higher energy, it is called Anti-Stokes-shifted scattering. The 'anti-stokes'

mode is much weaker than 'the stokes' mode and it is stokes-mode scattering that is usually observed. The frequency of light scattered from a molecule may be changed based on the structural characteristics of the molecular bonds. It provides information about the vibrational and electronic properties of semiconductors that are sensitive to crystalline quality, microstructure, strain, alloy composition and free carrier density. The intensity of the Raman scattered light is weak, hence an intense monochromatic light source like laser should be used.

Typically, the sample is illuminated with a laser beam. Light from the illuminated spot is collected with a lens and sent through a monochromator. Wavelengths close to the laser line (due to elastic Raleigh scattering) are filtered out and those in a certain spectral window away from the laser line are dispersed onto a detector. Raman spectrometers typically use holographic diffraction gratings and multiple dispersion stages to achieve a high degree of laser rejection. A photon-counting photomultiplier tube (PMT) or, more commonly, a CCD camera is used to detect the Raman scattered light. In the past, PMTs were the detectors of choice for dispersive Raman setups, which resulted in long acquisition times. However, the recent uses of CCD detectors have made dispersive Raman spectral acquisition much more rapid.²⁸

Recently micro Raman spectroscopy has emerged as a powerful technique for the study of vibrational spectra of crystals, glasses, polymer films etc. This technique has the advantage that it can be employed with microcrystalline samples because the spatial resolution can be as small as 1 μ m. Hence it is very useful in the study of chalcopyrite compounds where large single crystals are not available.

In the present work, Raman analysis was performed in the back scattering mode at room temperature using micro Raman system from Jobin Yvon Horibra LABRAM-HR visible (400 -1100 nm) with a spectral resolution of 1cm⁻¹. Argon ion laser of wavelength 488nm was used as excitation source.

2.4.3 Optical absorption studies

Most of the semiconductors generally absorb strongly in the visible region of the spectrum, having absorption coefficients of the order of 10^5 cm^{-1} . The characteristic feature of semiconductors in the pure state is that at a certain wavelength, generally in the near or intermediate infra-red, the absorption co-efficient drops rapidly and the material becomes fairly transparent at longer wavelengths. This marked drop in the absorption is called fundamental absorption edge or lattice absorption edge.

Absorption of light by different materials can induce various types of transitions such as band to band, between sub-bands, between impurity levels and bands, interactions with free carriers within a band, resonance due to vibrational state of lattice and impurities. These lead to the appearance of bands or absorption peaks in the absorption spectra. Hence the spectral positions of bands determine the types of transitions occurring during the process. In the absence of any thermal energy (about 0°K), only possible absorption that can take place is when the incident radiation is of sufficient energy to excite valence band electrons across the forbidden energy band gap into the conduction band. In the presence of defects, impurities, dislocations and other imperfections etc, one has to consider the perturbation of the system due to their presence and also their interactions with phonons. All these give rise to the indirect transitions.

The electronic transition between valence and conduction bands can be direct or indirect. In both cases, it can be allowed as permitted by the transition probability (p) or forbidden where no such probability exists. The transition probability is related by the equation,

$$\alpha = A(h\nu - E_g)^p \quad (2.18)$$

where p has discrete values like $1/2$, $3/2$, 2 or more depending on whether the transition is direct or indirect and allowed or forbidden. In the direct and allowed cases, the index $p=1/2$ whereas for the direct but forbidden cases it is $3/2$. But for the indirect and allowed cases $n=2$ and for the forbidden cases, it will be 3 or more. Thus a linear graph when α^2 is drawn against $h\nu$ will suggest a direct but allowed transition whereas a linear one with $\alpha^{1/2}$

against $h\nu$ indicates an indirect transition. The magnitude of p can also be estimated from the slope of the graph of $\log \alpha$ vs $\log (h\nu)$ and hence it can suggest the type of transition.

It is well established that, CIS is a direct band gap semiconductor with the band extreme located at the center of the Brillouin zone.¹⁶

For the present work, the equation (2.18) becomes,

$$\alpha = A(h\nu - E_g)^2 \quad (2.19)$$

A plot of $(\alpha h\nu)^{1/p}$ as a function of $h\nu$ gives a straight line, with an intercept on the $h\nu$ axis equal to the band gap of the material.

In the present work, band gap of CIS film was measured using optical absorbance and transmittance of the films. Spectrum was recorded using UV-VIS-NIR Spectrophotometer (Hitachi U-3410 and JASCO V 570 model).

2.4.4 Stylus profilometer

Stylus profilometer is an advanced tool for thickness measurement of both thin and thick films. It is capable of measuring steps even below 100\AA . This instrument can also be used to profile surface topography and waviness, as well as, measuring surface roughness in the sub nanometer range. The instrument takes measurements electromechanically by moving the sample beneath a diamond-tipped stylus. The high precision stage moves the sample beneath the stylus according to a user-programmed scan length, speed and stylus force. The stylus is mechanically coupled to the core of an LVDT (Linear Variable Differential Transformer).

As the stage moves the sample, the stylus rides over the sample surface. Surface variations cause the stylus to be translated vertically. Electrical signals corresponding to stylus movement are produced as the core position of the LVDT changes. The LVDT scales an AC reference signal proportional to the position change, which in turn conditioned and converted to a digital format through a high precision, integrating, analog to digital converter.

In the present work, thickness measurements were carried out using a Dektak 6M surface profilometer.

2.4.5 Photoluminescence(PL)

Photoluminescence spectroscopy is a contactless, nondestructive method of probing the electronic structure of materials. Light is directed onto the sample, where it is absorbed and imparts excess energy into the material in a process called photo-excitation. One way this excess energy can be dissipated by the sample is through the emission of light or luminescence. In the case of photo-excitation, this luminescence is called 'photoluminescence'. The intensity and spectral content of this photoluminescence is a direct measure of various important material properties. In the present study PL is used to determine the defect levels in the samples. It is particularly suited for the detection of shallow level impurities, but can be applied to certain deep level impurities provided their recombination is radiative. In general, non-radiative processes are associated with localized defect levels, whose presence is detrimental to material quality and subsequent device performance. Thus, material quality can be measured by quantifying the amount of radiative recombination.

The sample is placed inside a cryostat and cooled to temperatures near liquid Helium. Low temperature measurements are necessary to obtain the fullest spectroscopic information by minimizing thermally activated non-radiative recombination processes and thermal line broadening. The thermal distribution of carriers excited into a band contributes a width of approximately $kT/2$ to an emission line originating from that band. This makes it necessary to cool the sample to reduce the width. The thermal energy $kT/2$ is only 1.8meV at $T=4.2$ K. Using a scanned photon beam or moving the sample allows PL maps to be generated. The sample is excited with an optical source typically a laser with energy $h\nu > E_g$, generating electron-hole pairs which recombine by one of several mechanisms. Photons are emitted for radiative recombination. Photons are not emitted for the non-radiative recombination in the bulk or at the surface. For good PL output, the majority of the recombination process should be radiative.

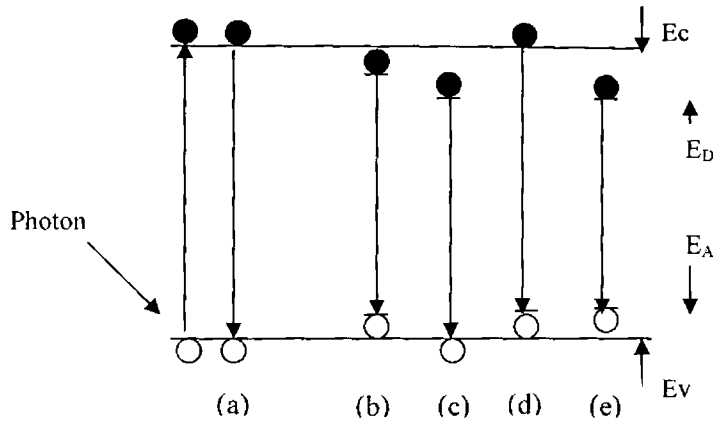


Fig 2.2: Transitions occurring in PL spectra

Five kinds of transitions mostly occurring in the PL measurement are shown in the fig.2.2. Band to band recombination (a), excitonic recombination (b), bound excitonic recombination(c & d) and donor-acceptor recombination (e).

The photon energy in a direct band gap semiconductor is

$$h\nu = E_g - E_x \quad (2.20)$$

where E_x is the excitonic binding energy. In the case of donor-acceptor recombination, the emission line has an energy modified by the Coulombic interaction between donors and acceptors

$$h\nu = E_g - (E_A + E_D) + e^2 / \epsilon r \quad (2.21)$$

where r is distance between donor and acceptor. The full width at half maximum (FWHM) for bound exciton transitions are typically $\leq kT/2$ and resemble slightly broadened delta functions.²⁹

In the present work, PL measurements were carried out in the temperature range 12 to 300 K with a closed cycle liquid Helium cryostat (Janis Research Inc.). The temperature was maintained with an accuracy of ± 1 K using a temperature controller (Lake Shore Model 321). The 632.8 nm line of a He-Ne laser (5 mW, Melles Griote) was used as the

excitation source. The laser beam was focused onto the samples with a beam diameter of 1mm. Emission spectra were analyzed using spectrophotometer (Ocean optics NIR 512) having a InGaAs linear array detector.

2.4.6 Energy Dispersive Analysis by X-rays (EDAX)

When an element is bombarded with a particle beam, in this case an electron beam, the specimen will release some of the absorbed energy as x-rays. Much of the time, the energy is the result of changes in the speed of an electron, which is random; however, when this interaction removes an electron from a specimen's atom, frequently an electron from an outer shell (or orbital) occupies the vacancy. When an outer electron occupies a vacancy, it must lose a specific amount of energy to occupy the closer shell. This amount is readily predicted by the laws of Quantum Mechanics and usually much of the energy is emitted in the form of X-rays.

The X-ray detector in the EDAX is a reverse biased semiconductor (usually Si) pin or Schottky diode. X-rays are absorbed in a solid according to the equation

$$I(x) = I_0 \exp[-(\mu/\rho)\rho x] \quad (2.22)$$

with (μ/ρ) , the mass absorption co-efficient, ρ the detector material density, $I(x)$ the X-ray intensity in the detector, and I_0 the incident X-ray intensity. The mass absorption co-efficient is characteristic of a given element at specified X-ray energies. Its value varies with the photon wavelength and with the atomic number of the target element, generally decreasing smoothly with energy. It exhibits discontinuities in the energy region immediately above the absorption edge, corresponding to the energy necessary to eject an electron from a shell.

The X-rays from the sample pass through a thin Beryllium window onto a Lithium drifted Si detector, which should be cooled at times. Liquid Nitrogen cooling prevents Lithium diffusion and also reduces the diode leakage current. Each absorbed X-ray creates many electron-hole pairs which are swept out of the diode by high electric field in the space-charge region. The charge pulse is converted to a voltage pulse by a charge sensitive pre-

amplifier. The signal is further amplified and shaped and then passed to a multi channel analyzer.

Elements from Na to U can be detected with EDAX. However, it is difficult to detect lower Z elements due to the Be window that isolates the cooled detector from the vacuum system. Windowless system allows lower Z elements to be detected.

In this work, the compositional analysis and surface morphology were studied using Scanning Electron Microscopy (JEOL JSM-5600).

2.4.7 Atomic Force Microscopy (AFM)

Atomic force microscopy operates by measuring the forces between a probe and the sample. These forces depend on the nature of the sample, the distance between probe and the sample, the probe geometry and the sample surface contamination. AFM is suitable for conducting as well as insulating samples.

In atomic force microscope, a sharp tip is scanned over a surface with feedback mechanisms that enable the piezo-electric scanners to maintain the tip at a constant force (to obtain height information), or height (to obtain force information) above the sample surface. Tips are typically made from Si_3N_4 or Si, and extended down from the end of a cantilever. The nanoscope AFM head employs an optical detection system in which the tip is attached to the underside of a reflective cantilever. A diode laser is focused onto the back of a reflective cantilever. As the tip scans the surface of the sample, moving up and down with the contour of the surface, the laser beam is deflected off the attached cantilever into a dual element photodiode. The photo detector measures the difference in light intensities between the upper and lower photo detectors, and then converts to voltage. Feedback from the photodiode difference signal, through software control from the computer, enables the tip to maintain either a constant force or constant height above the sample. In the constant force mode the piezo-electric transducer monitors real time height deviation. In the constant height mode, the deflection force on the sample is recorded. The latter mode of operation requires calibration parameters of the scanning tip to be inserted in the AFM head during force calibration of the microscope. In non contact

mode, the AFM derives topographic images from measurements of attractive forces; the tip does not touch the sample. AFMs can achieve a resolution of 10 pm

In the present work, AFM-Nanoscope-E, Digital Instruments, was used for the measurements. The measurements were taken in contact mode.

2.4.8 X-ray Photoelectron Spectroscopy (XPS)

X-ray Photoelectron Spectroscopy (XPS), also known as Electron Spectroscopy for Chemical Analysis (ESCA), is used to determine quantitative atomic composition and chemistry. It is a surface analysis technique with a sampling volume that extends from the surface to a depth of approximately 50-70Å. Alternatively, XPS can be utilized for sputter depth profiling to characterize thin films by quantifying matrix-level elements as a function of depth. XPS is an elemental analysis technique that is unique in providing chemical state information of the detected elements, such as distinguishing between sulfate and sulfide forms of the element sulfur. The process works by irradiating a sample with monochromatic X-rays, resulting in the emission of photoelectrons whose energies are characteristic of the elements within the sampling volume.

XPS involves the removal of a single core electron, while Auger Electron Spectroscopy is a two-electron process subsequent to the removal of one core electron, with Auger electron ejected following reorganization within the atoms. Auger electrons are produced in XPS along with photoelectrons.

The sample is irradiated with X-rays of known energy, $h\nu$, and the electrons of binding energy (BE) E_b are ejected, where $E_b < h\nu$. These electrons have a kinetic energy E_k which can be measured in the spectrometer, and is given by

$$E_k = h\nu - E_b - \Phi_{sp} \quad (2.23)$$

Where Φ_{sp} is the spectrometer work function, and is the combination of the sample work function, Φ_s , and the work function induced by the analyzer. The work function term can be compensated electronically, hence

$$E_k = h\nu - E_b$$

or

$$E_b = h\nu - E_k \quad (2.24)$$

Thus by measuring the KE of the photoelectrons, the above equation can be used to translate this energy into BE of the electrons.³⁰

The surface sensitivities of electron spectroscopies are due to the low inelastic mean free path λ_m , of the electrons within the sample. For XPS, the main region of interest relates to electron energies from 100-1200eV, which gives rise to a λ_m value of 0.5-2 nm. However the actual escape depth, λ , of the photoelectrons depends on the direction in which they are traveling within the solid, such that

$\Lambda = \lambda_m \cos\theta$ where θ is the angle of emission to the surface normal. Thus electrons emitted perpendicular to the surface will arise from the maximum escape depth, whereas electrons emitted nearly parallel to the surface will be purely from the outermost surface

X-ray Photoelectron Spectroscopy (XPS-ULVAC-PHI Unit, Model: ESCA 5600 CIM), employing argon ion sputtering was employed in the present work.

2.4.9 Electrical Characterization

(i) Resistivity / Conductivity

Conductivity of a semiconductor crystal is considerably affected by lattice vibrations, impurities, strain, displaced atoms in the lattice, grain boundaries etc.

Conductivity can be expressed in terms of material dimensions through resistivity or resistance (ρ or R). If L and B are the length and breadth of a rectangular shaped specimen and d is the thickness then,

$$R = \frac{\rho L}{Bd} \quad \text{where } \rho \text{ is the resistivity in ohm-cm}$$

$$\rho = \frac{RBd}{L} \text{ or } \sigma = \frac{L}{RBd} \quad (2.25)$$

ρ and σ are constant for any particular bulk material at a fixed temperature but not for films, since these are dependent on thickness unlike the bulk material.

$$\frac{\rho}{d} = \frac{RB}{L} = R_s \quad (2.26)$$

where R_s is known as the 'sheet resistance' which is expressed in ohm per square.

If we assume $L=B$, then $\frac{\rho}{d} = R = R_s$ which means that the resistance of one square of a film is its sheet resistance R_s and it is independent of the size of the square but depends only on resistivity and film thickness. If the film thickness is known then resistivity is given by,

$$\rho = d \cdot R_s \quad ^{16}$$

(ii) Photosensitivity

Photosensitivity is a measure of the minority carriers in a semiconductor produced on illumination with light. It is calculated as

$$\phi = \frac{I_L - I_D}{I_D} \quad (2.27)$$

where I_L is the current under illuminated condition and I_D is the current under dark conditions. In this work, samples are illuminated using a tungsten halogen lamp of intensity 100mW/cm^2 to measure photosensitivity.

(iii) Activation energy from Temperature Dependant Electrical Conductivity

Activation energy measures the thermal or other form of energy required to raise electrons from the donor levels E_d to the conduction band or to accept electrons by the acceptor levels E_a from the valence band respectively for n and p-type materials. This corresponds to the energy height difference $(E_c - E_d)$ and $(E_a - E_v)$ respectively. It can be

experimentally measured from the variation of ρ or σ with increase or decrease temperature.

$$\sigma = \sigma_0 \exp\left(-\frac{E_a}{kT}\right) \quad (2.28)$$

where E_a = activation energy (or enthalpy) of the process

A plot of $\log(\sigma)$ against $1/T$ (Arrhenius plot) will be linear with its slope equal to the activation energy. If the slope changes at different regions of temperature, it indicates a variation of activation process i.e. activation energy due to thermal excitation of impurities situated at different levels in the band gap and consequent jumping of electrons either to the conduction band or to the acceptor level.

(iv) Type of conductivity using hot probe

Conductivity type can be determined by hot or thermoelectric probe method; the conductivity type is determined by the sign of the thermal emf or Seebeck voltage generated by the temperature gradient. Two probes are kept in contact with the sample surface, with one hot and the other cold.

Thermal gradients produce currents in a semiconductor; the majority carrier currents for n and p-type materials are

$$J_n = -qn\mu_n P_n \frac{dT}{dx} \quad \text{and}$$

$$J_p = -qP\mu_p P_p \frac{dT}{dx} \quad (2.29)$$

Where $P_n < 0$ and $P_n > 0$ are the differential thermoelectric power.

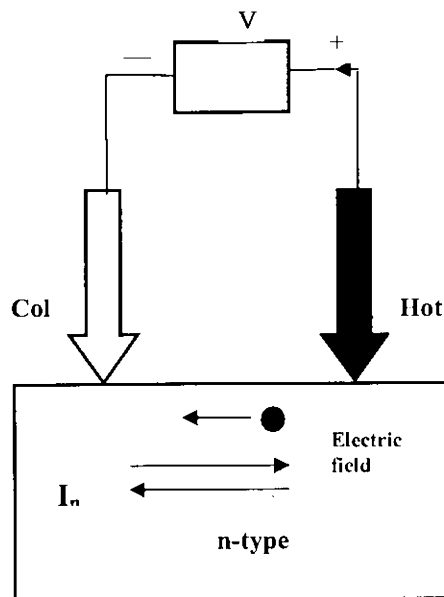


Fig 2.3: Hot probe method

In fig 2.3, $dT/dx > 0$, and the electron current in an n-type sample flows from left to right. The thermoelectric power can be thought of as a current generator. A part of the current flows through the voltmeter causing the hot probe to develop positive potential with respect to the cold probe. Electrons diffuse from the hot to the cold region setting up an electric field that opposes diffusion. The electric field produces a potential detected by the voltmeter with the hot probe positive with respect to the cold probe. Analogous reasoning leads to the opposite potential for p-type samples.

Hot probes are effective over the 10^{-3} to $10^3 \Omega\text{cm}$ resistivity range. The voltmeter tends to indicate n-type for high resistivity material even if the sample is weakly p-type, because this method actually determines the $n\mu_n$ or the $p\mu_p$ product. With $\mu_n > \mu_p$, intrinsic or high resistivity material is measured n-type if $n \approx p$. In semiconductors with $n_i > n$ or $n_i > p$ at room temperature, it may be necessary to cool one of the probes and let the room temperature probe be the hot one²⁹.

References

1. Piekozewski J, Loferski J.J, Beaulieu R, Beall J, Roessler B, Shewchun J, *Solar Energy Mater.* **2** (1980)363
2. M.A. Contreras, K. Ramanathan, J. AbuShama, F. Hasoon, D.L. Young, B. Egaas, and R. Noufi, *Prog. Photovolt: Res. Appl.* **13** (2005) 209
3. P.K.Vidyadharan Pillai and K.P.Vijayakumar, *Sol. Energy Mater. Sol. Cells* **51** (1998) 47
4. Tomoaki Terasako, Yuji Yuno, Tetsuya Kariya, Sho Shikarta, *Sol. Energy Mater. Sol. Cells* **90** (2006) 262
5. C.Guillen, E.Galiano, J.Herrero *Thin Solid Films* **195** (1991) 137
6. M.C.Artaud, F.Ouchen, L.Martin, S.Duchemin, *Thin Solid Films* **324** (1998)115
7. Grindle S P, Clark A H, Rezaie-Serej S,Falconer E, McNeily J, Kazmerski L L 1980, *J.Appl.Phys.* **51** (1980)5464
8. J.Levoska, S Leppävuori, F Wang, O Kusmartseva, A E Hill, E Ahmed, R D Tomlinson and R D Pilkington, *Phys. Scr.* **T54** (1994) 244
9. C.H. Champness, *J. Mater. Sci. Mater. Electron.* **10** (1999) 605
10. M.Valdes, M.A.Frontini, M.Vazquez, A Goossens, *Appl.Surf.Sci.*(2007), doi:10.1016/j.apsusc.2007.07.063
11. Marian Nanu, Joop Schoonman, and Albert Goossens, *Nano Lett.*, **5** (9) (2005)1716
12. M A Martinez, C Guillen, A Morales, J Herrero, *Surface and Coatings Technology* **148**(2001) 61
13. V. K. Kapur, A. Bansal, O. Asensio, P.Le, N. Shigeoka, "Fabrication of Solar Cells via Printing of Nanoparticle Inks" DOE Solar Energy Technologies Program Review Meeting, Denver, CO (2005) 135
14. S.Niki, P.J.Fons, A.Yamada, Y.Lacroix, H.Shibata, H.Oyanagi, M.Nishitani, T.Negami, T.Wada, *Appl.Phys.Lett.*, **74**(1999) 1630
15. *Practical Hand book of Photovoltaics*, Tom Makwart and Luis Castaner, Elsevier Advanced Technology, UK(2003)
16. A.Goswami, *Thin Film Fundamentals*, New Age International (P) Limited, New Delhi (1996)
17. E.B.Yousafi, T Asikainen, V Pietu, P Cowache, M Powalla, D Lincot, *Thin Solid Films* **361-362**(2000)183

18. A Strohm, L Eisenmann, R.K. Gebhardt, A Harding, T Schlotzer, D Abou-Ras, H W Schock EMRS Spring meeeting 2004
19. C.D Lokhande, A Ennaoui, P S Patil, M Giersig, K Diesner, M Muller, H Tributsch, *Thin Solid Films* **340**(1999)18
20. Teny Theresa John, S.Bini, Y Kasiwaba, T Abe, Y Yasuhiro, C Sudha kartha, K P Vijayakumar, *Semicond.Sci.Technol.***18**(2003) 491
21. Paul O' Brien, David J Otway, John R Walsh, *Thin Solid Films* **315**(1998) 57
22. D Hariskos, R Menner, S Spiering, A Eicke, M Powalla, K Ellmer, M Oertel, B Dimmler, 19th EUPVSEC, Paris 2004
23. G A Kitaev and G M Fofauov, *Zh.Prikl.khim*[Leningrad] **43** (1970) 169
24. K.Bindu, C.Sudhakartha, K.P.Vijayakumar, T.Abe and Y.Kashiwaba, *Solar Energy Materials and Solar Cells* **79** (2003) 67
25. M. Ortega – Lopez and A. Morales- Acevedo *Thin Solid Films* **330** (1998) 96
26. N. Bouguila, H. Bouzouita, E. Lacaze, A. B. Amara, H. Bouchriha and A. Dhouib *J. de Physique III* **7** (1997) 1647
27. X-ray methods, Clive Whiston, John Wiley and sons, New york (1987)
28. Optical processes in semiconductors, Jacques I Pankove, Dover Publications Inc, New York (1971)
29. Semiconductor Material and Device Characterization, Dieter K Schroder , John Wiley and sons, New York (1998)
30. Surface Analysis Methods in Material Science, D.J.O'connor, B A Sexton, R St.C.Smart, Springer-Verlag, Germany (1992)

CuInSe₂ Thin Films Using Chemical Bath Deposited Selenium

3.1 Introduction

With an efficiency of 19.9% in the laboratory scale and 13.4% in the industrial scale, CuInSe₂ today is the supreme nominee for thin film solar cell.¹ However production of device quality material over large area at low cost still remains to be the key issue in the production line of solar cells using this material. This chalcopyrite compound also finds application in the area of visible and Infra Red LEDs, Infra Red detectors, optical parametric oscillators and up-converters, apart from thin film solar cells²⁻⁵. A wide variety of methods has been employed in the deposition of CuInSe₂ thin films like co-evaporation⁶, flash evaporation⁷, electro-deposition⁸, chemical bath deposition⁹, sputtering¹⁰, selenization of Cu-In alloy¹¹, spray pyrolysis¹², molecular beam epitaxy¹³, screen printing¹⁴ etc. In many of these cases, selenization is done either using H₂Se gas or Se vapor, which is highly toxic.

As an alternative to these toxic approaches, a method which is simple, ecofriendly and capable of giving large area samples with uniformity was proposed and standardized by Bindu et al.¹⁵. The technique involved a combination of Chemical Bath Deposition (CBD) and Physical Vapor Deposition (PVD) techniques to yield CuInSe₂ thin films. In this method Selenium layer was deposited using CBD while Indium and Copper layers were deposited using PVD. CuInSe₂ thin films were prepared through two different processes using CBD Se. In this, the first process, named as 'technique A', involved deposition of Copper and Indium using thermal evaporation over the Se film prepared through CBD and successive annealing of this stacked layer containing Se/Cu/In in

vacuum at 400°C, resulting in the formation of CuInSe₂. In the second process, named as 'technique B' on top of the Se layer, In was deposited using thermal evaporation and this stack layer of Se/In was annealed at a temperature of 100°C to obtain In₂Se₃. This was then converted it into CuInSe₂ by thermal diffusion of Cu into In₂Se₃, with further annealing in vacuum at 400°C.

Improvements were made in these two techniques to get better stoichiometric CuInSe₂ films with better crystallinity, grain size, uniform thickness and increased photosensitivity. For this, the ratio of Cu and In was varied over a wider range and all the samples were characterized structurally, optically and electrically. On comparison of the properties of the films, it was noted that the technique of thermal diffusion of Cu into In₂Se₃ was better than the stacked elemental layer (SEL) deposition, for getting good quality CuInSe₂ films consistently. One of the main advantages of both these techniques is that Se film for selenization was prepared using CBD at room temperature, avoiding the usage of highly toxic H₂Se or Se vapour. It was possible to prepare Cu-rich, In-rich and nearly stoichiometric films by the two techniques. A detailed study of CuInSe₂ thin films, deposited by this method was carried out and an attempt to device fabrication is also made. More details of sample preparation are given in chapter 2.

3.2 Experimental details

CuInSe₂ films were prepared using two different techniques as detailed earlier. In order to standardize a route for the preparation of stoichiometric CuInSe₂ thin films, concentrations of Cu and In were varied, keeping thickness of the Se layer constant (0.25µm) in all the cases. When the thickness was increased beyond 0.25µm, the samples started to peel-off. For both the routes of preparation, samples were prepared by varying the concentration of In, keeping the mass of Cu fixed at 20 mg. In- was varied from 20 mg to 100 mg, in steps of 20 mg. Sample nomenclature was done on the following basis: A sample was named as CIS22- when 20 mg of Cu and In was evaporated on to the Se film. Similarly for CIS24 -Cu 20 mg and In 40 mg, for CIS26 -Cu 20 mg and In 60 mg, for CIS28 -Cu 20 mg and In 80 mg and for CIS210-Cu 20 mg and In 100 mg were used

respectively for film preparation. Among this set of samples, CIS28 was found to be better in crystallinity and hence in the next step, In was fixed at 80 mg and Cu was varied from 30 to 50 mg in steps of 10 mg. Samples in this set were named as CIS38, CIS48 and CIS58 following the same nomenclature rule as in the earlier case.

3.3 Structural characterization

The X-ray diffractograms of the samples the prepared using technique A [by varying mass of In and keeping mass of Cu constant -CIS22 to CIS210] are shown in fig.3.1. Diffraction peaks were observed at angles 26.5° , 44.17° and 52° , which were corresponding to planes (112), (204)/(220), (116)/(312) respectively. The (204)/(220) and (116)/(312) peaks were not resolved in the XRD.

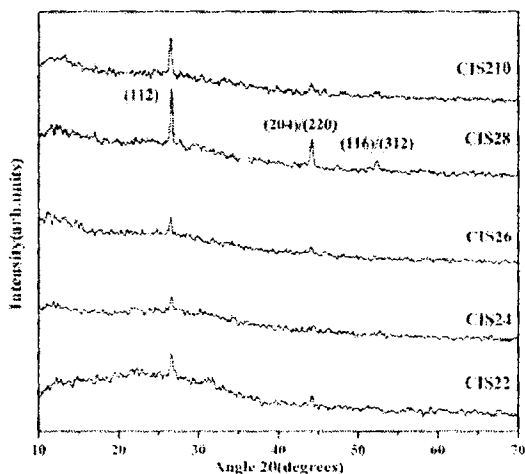


Fig 3.1: XRD pattern of samples prepared through technique A

Corresponding d values were obtained as 3.34, 2.04 and 1.74 \AA respectively, which agreed with the standard JCPDS data card (JCPDS 23-209) confirming the existence of tetragonal CuInSe_2 phase in the thin films prepared using this technique. From the XRD analysis, it was also observed that in sample CIS22, only two peaks corresponding to the planes (112) and (204)/(220) were prominent. It could be expected that this film would be Cu-rich because of the initial stoichiometry of the precursors. Moreover, there can be loss of Indium due to the annealing at 400°C . When the In content was increased to obtain

sample CIS24, the crystallinity decreased. On further increasing the 'In' content, the crystallinity increased and reached maximum for the sample CIS28, in which all the three prominent peaks became clearly visible. This increase in crystallinity could be attributed to the improved stoichiometry of the sample. Further increase of the In-content, (sample CIS210) resulted in decrease of the crystallinity, which was attributed to the deviation from stoichiometry. It was also observed that the additional growth planes at (204)/(220) and (116)/(312) were disrupted at higher percentage of 'In'. Hence it was concluded that initially 80 mg of 'In' could be used to grow crystalline CuInSe₂ thin films. Grain size was calculated from the XRD data using the Debye-Scherrer formula. Table 3.1 depicts the variation in grain size

Table 3.1: Variation of grain size with Cu/In ratio for techniqueA

Sample Name	Grain size (nm)
CIS22	17
CIS24	14
CIS26	25
CIS28	26
CIS210	24

The maximum gain size was obtained for the most crystalline sample, CIS28. Large grain size is one of the fundamental requirements in photovoltaics so as to reduce grain boundary scattering and improve conductivity. This was another reason to fix In-content at 80 mg for the next step in CuInSe₂ preparation.

CuInSe₂ thin films can exist in two different structures viz. chalcopyrite and sphalerite (a disordered version of chalcopyrite). Some of the XRD peaks are common to both sphalerite and chalcopyrite structures and these common peaks were obtained from the present XRD studies. Hence the structure of the films could not be confirmed from the XRD analysis alone. To confirm the structure, Raman analysis was performed using an

Argon ion laser of wavelength 488 nm as excitation line. Raman analysis was carried out on selective samples only (Cu-rich, In-rich and nearly stoichiometric) it was observed that the strongest Raman peak was at 233cm^{-1} which proved that the structure was sphalerite.

Fig 3.2 shows the variation in crystallinity for the samples prepared through technique B, for the same concentrations as for the technique A described above. The same nature of variation in crystallinity was observed for these samples also. Through technique B, it was found that as In-content was increased, crystallinity decreased, reaching a minimum for CIS26 and abruptly rose to maximum for CIS28. But for CIS210, the crystallinity again decreased. The major difference between the CuInSe_2 films prepared using the two techniques A and B films was in sample CIS210. CIS210 prepared through technique B, exhibited In_2Se_3 phase which may be due to the fact that loss of Indium was less in this method, as 'In' was in the compound form In_2Se_3 , before annealing at 400°C . Fig 3.3 shows the XRD spectrum of CIS210, which clearly shows the existence of In_2Se_3 phases along with the CuInSe_2 phase in the sample.

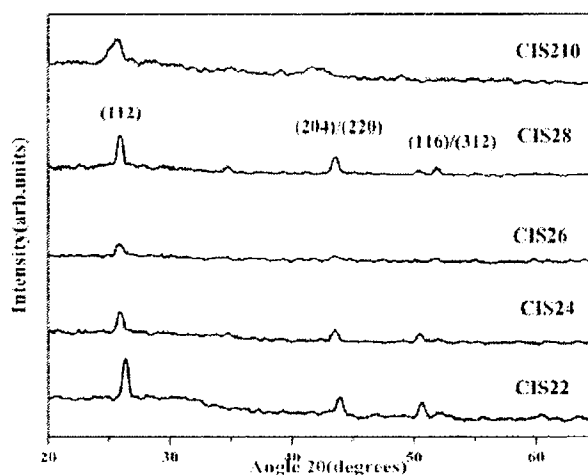


Fig 3.2: XRD pattern of samples prepared using technique B

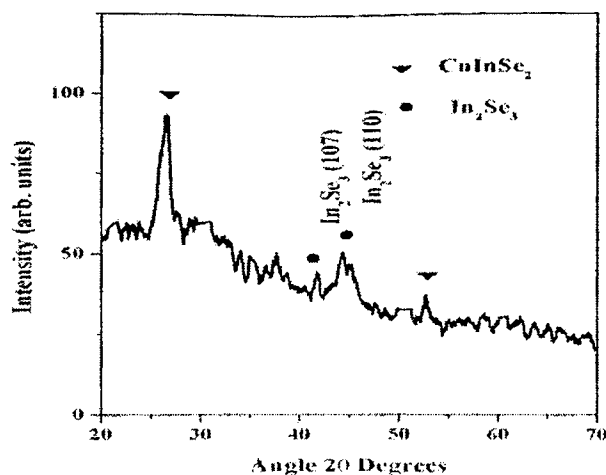


Fig 3.3: XRD pattern of CIS210

The variation in grain size for this set of samples is shown in the Table 3.2; sample CIS22 which was Cu-rich, possessed the maximum grain size and had a grain size identical to that of CIS22, prepared through the technique A. The grain size decreased with increase in Indium concentration. There was an increase in grain size for CIS28 [as observed in the sample prepared using technique A], but the gain size decreased when In-content was increased to 100 mg in CIS210.

Table 3.2: Variation of grain size for the samples prepared through technique B

Sample name	Grain Size (nm)
CIS22	18
CIS24	17
CIS26	16
CIS28	18
CIS210	13

CIS210 was having the smallest grain size and hence could be assumed to be the one with maximum 'In' concentration. By direct comparison of the diffractograms of the films

grown using the two techniques it could be concluded that best crystallinity was obtained when the 'In' composition was fixed at 80 mg. To improve the crystallinity further, the Cu concentration was varied keeping the Indium content fixed at 80 mg. Concentration of Cu was varied to 30 mg, 40 mg and 50 mg respectively so that sample nomenclature was now CIS38 for Cu 30 mg and In 80 mg; CIS48 for Cu 40 mg and In 80 mg and CIS58 for Cu 50 mg and In 80 mg.

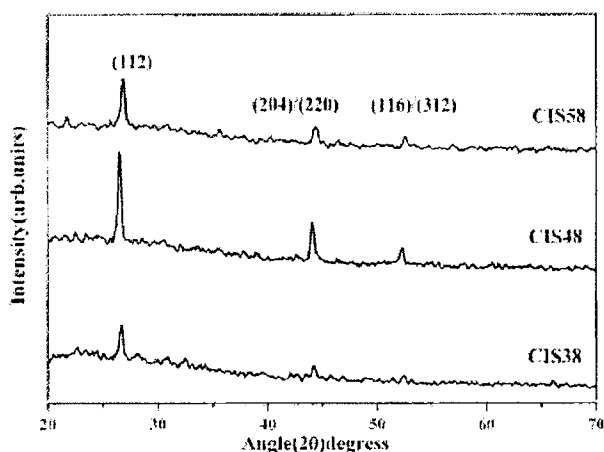


Fig 3.4: XRD pattern of Cu-varied samples prepared using technique A

Fig.3.4 shows the XRD pattern of samples CIS28 to CIS58 prepared using this technique A. As concentration of Cu increased, crystallinity increased, [with maximum for Cu= 40 mg -CIS48] and then decreased on further increasing the Cu- content. It is well established that films with the stoichiometry 1:1:2 show maximum crystallinity and on deviation from this, the crystallinity reduces. The improvement in crystallinity and then a decrease could be hence due to the approach to stoichiometry and subsequent deviation from it, as Cu-content increases. An important result was that all the samples showed three prominent peaks very clearly which was absent when the In-content was varied from 80 mg. Also the growth of the planes was well affected when the Cu-content was varied which strongly indicated that formation of the films was not in direct proportion to the initial precursor masses. Had it been so, the improved crystallinity should be observed

for initial precursor having Cu 20 mg and In 20 mg, where the stoichiometry Cu/In =1, as per the requirement for ideal stoichiometry. Grain size was calculated for this set of samples and results are as shown in Table 3.3. Grain size increased to 24nm on increasing the Cu content and for CIS58, it decreased.

Table 3.3: Variation of grain size for Cu-varied samples grown using technique A

Sample name	Grain size (nm)
CIS38	23
CIS48	24
CIS58	18

A set of samples was prepared using technique B by fixing ‘In’ content at 80 mg and varying Cu in order to compare the effect of the growth process. The X-ray diffraction pattern for the set of samples prepared is shown in the Fig 3.5.

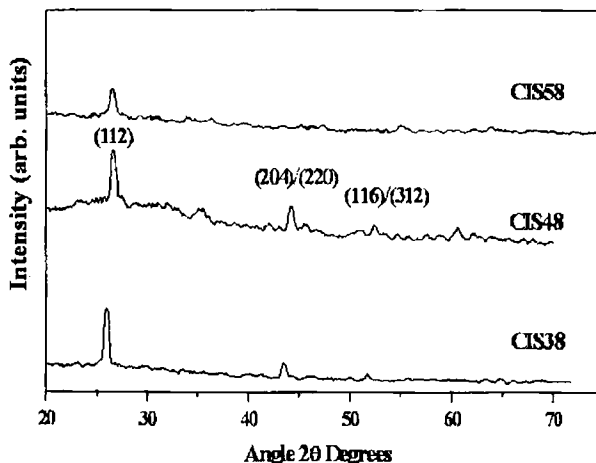


Fig 3.5: XRD pattern of Cu-varied samples prepared through technique B

As the sample stoichiometry was changed from CIS38 to CIS58 using this technique, it was observed that the crystallinity increased to a maximum for sample CIS48 and then decreased with further increase in Cu. The additional diffraction peaks at (204)/(220) and

(116)/(312) were absent in sample CIS58. The growth mechanism in this case was thus similar to that for the films prepared using technique A. It could however be observed that the crystallinity of the CIS48 prepared using technique A was better than the one grown using technique B. Table 3.4 shows the variation in grain size for this set of samples. Maximum grain size of 19 nm was obtained for sample CIS48, which was also the most crystalline sample in the set.

Table 3.4: Variation in grain size of Cu-varied samples prepared through technique B

Sample name	Grain size (nm)
CIS38	18
CIS48	19
CIS58	16

Among the batch of samples prepared using the two techniques and different stoichiometry, CIS48 grown using technique A was the most crystalline. The grain size of the samples prepared using technique A was, on the average, greater than that of samples prepared using technique B in spite of having the same stoichiometry. But no large scale variations were there. Maximum grain size of 26nm was obtained for the samples prepared using technique A while for the sample from technique B, it was 18nm for the same composition.

3.4 Optical characterization

Optical absorption studies were carried out on all the samples, measuring the absorption spectra in the wavelength range 500 nm to 1500 nm. Band gap (E_g) was obtained by extrapolating the linear portion of the $(\alpha hv)^2$ versus hv graph to hv axis. Figs 3.6 (a) and (b) show the absorption spectra of CIS22 and CIS210. The same trend in variation of the band gap was noted with variation in Cu/In ratio for the samples prepared using the two techniques and is given in tables 3.5.

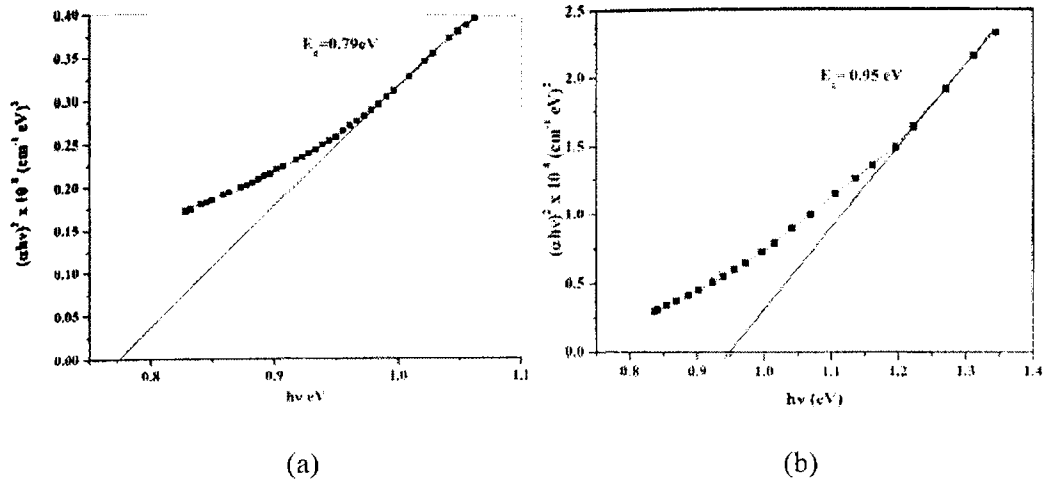


Fig 3.6: Absorption spectra of sample (a) CIS22 and (b) CIS210

It was observed that the band gap decreased with increase in Cu concentration. Band gap was lowest for Cu-rich film CIS22 (0.79eV) and largest for In-rich film CIS210 (0.95eV).

Table 3.5: Band gap variation samples prepared through technique A and B

Sample name	Band Gap E_g (eV)	
	Technique A	Technique B
CIS22	0.79	0.82
CIS24	0.94	0.93
CIS26	0.85	0.89
CIS28	0.87	0.9
CIS210	0.88	0.95
CIS38	0.92	0.93
CIS48	0.91	0.92
CIS58	0.88	0.83

As can be seen in table 3.5, samples did not show any kind of dissimilarity (except CIS210) in their optical band gap based on the route of preparation. In both the cases, the band gap was lowest for the Cu-rich sample CIS22 (0.79 eV for the samples prepared through technique A and 0.82 eV for the samples prepared through technique B) and was largest for the In-rich sample CIS210 (0.88 eV for the samples prepared through technique A and 0.95 eV for the samples prepared through technique B). In general, it could be stated that the band gap was larger for films prepared by technique B than that of the films [of the same composition] prepared using technique A.

In the case of I-III-VI₂ compounds, the uppermost valence bands get strongly influenced by the metal d levels (in the present case Cu-d levels). The Cu-3d levels and Se-4p levels being degenerate and possessing same symmetry because of the p-d hybridization interaction and cause the valence band maxima to be displaced upwards.¹⁶ Hence an increase in Cu content could increase the spread of Cu-3d orbital, which enhances the possibility of interaction, leading to the reduction of the band gap. However a drastic increase in Cu concentration will increase the number of donors and thus shift the Fermi level to the conduction band (Burstein-Moss shift), thereby increasing the band gap.¹⁷

3.5 Electrical characterization

Type of majority carriers in the films deposited was identified using 'hot probe method'. All the samples showed p-type conductivity except CIS210, which showed n-type conductivity. This could be due to presence of excess In. It was observed that In-rich films showed n-type conductivity while near-stoichiometric and Cu-rich films demonstrated p-type conductivity.¹⁸ The p-type conductivity is achieved by cation vacancies or anion interstitials while n-type conductivity is due to anion vacancies or by cation interstitials.

Sheet resistance and photosensitivity measurements were carried out on all the samples and it was observed that these were the highest for the In-rich sample [CIS210] and minimum for the Cu-rich film [CIS58], for the samples obtained from both the techniques. Photosensitivity is a measure of minority carriers generated by light. For the

highly resistive sample, the effect of minority carriers will be enhanced and hence the photosensitivity would be improved. It could be observed that the sheet resistance and photosensitivity were different for the samples prepared using the two techniques even though there was not much variation in crystallinity, grain size and band gap for these samples.

Table 3.6: Comparison of photosensitivity and sheet resistance of the samples prepared through the two different techniques

Sample name	Photosensitivity		Sheet resistance MΩ	
	Technique A	Technique B	Technique A	Technique B
CIS22	0.05	0.9	0.643×10^{-3}	9
CIS26	2.90	7	325	385
CIS28	0.24	11	3	1378
CIS210	3.20	9	608	469

Table 3.6 shows the sheet resistance and photosensitivity of the films prepared using the two techniques. From the table, it was clear that, photosensitivity was better for samples prepared using technique B. A definite conclusion about the sheet resistance of the films could not be made on similar line, since for certain stoichiometry, films deposited by technique A, had lower sheet resistance and for some other stoichiometry the films grown under technique B, had lower sheet resistance.

3.6 Observations

Photosensitivity of the absorber layer plays an important role in the performance of a solar cell. Hence it was concluded that, out of the two types of CuInSe₂ films, films prepared using thermal diffusion of Copper into In₂Se₃ which showed better material

properties, were more suitable for photovoltaic applications. Hence further analysis was carried out on these samples. In order to increase the Cu content the samples were prepared by decreasing the 'In' content. A sample of this kind was CIS52, which was prepared by evaporating 20 mg of In and 50 mg of Cu. CIS52, CIS48 and CIS210 were selected for further studies so that the stoichiometry was Cu-rich, nearly stoichiometric and In-rich respectively.

3.7 Compositional analysis

Atomic concentration of the constituent elements present in the samples was determined using EDAX. A typical EDAX spectrum is shown in fig. 3.7 and the atomic concentration for the set of ideal samples is given in table 3.7.

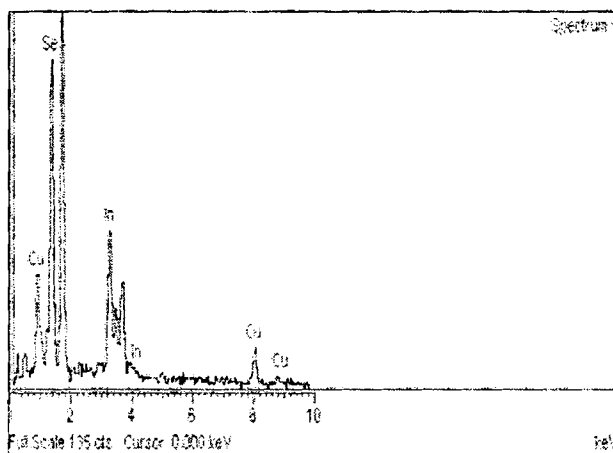


Fig.3.7: A typical EDAX spectrum of CuInSe_2

On analyzing the EDAX results, it was found that sample CIS52 was Cu-rich, CIS210 was In-rich and CIS48 was nearly stoichiometric, as expected. Based on the compositional analysis, it could now be concluded that the mass of In required was double the mass of Cu, for obtaining a nearly stoichiometric film (In-80mg and Cu-40mg). This might be due to the fact that melting point of In was only 150°C and hence some quantity of In was always lost during annealing at 400°C .

Table 3.7: Atomic concentration in percentages

Sample Name	Cu%	In%	Se%
CIS210	8.79	35.04	56.16
CIS48	20.73	24.65	54.65
CIS52	41.24	16.28	42.48

3.8 Structural analysis

On comparing the X-ray diffractograms of the samples CIS52, CIS48 and CIS210 secondary phases were obtained for Cu-rich (Fig 3.8) and In-rich films (Fig 3.9) while single phase CuInSe₂ was obtained for nearly stoichiometric film (Fig.3.10). For the pure CuInSe₂ phase, planes were identified as (112) at $2\theta = 26.6^\circ$, (220)/(204) at $2\theta = 44.1^\circ$ and (116)/(312) at $2\theta = 52.3^\circ$ respectively with preferred orientation along (112) plane (JCPDS card 23-209).

In the case of sample CIS52 (Cu-rich), secondary phases such as CuSe, Cu₂Se and Cu_{2-x}Se (Fig. 3.8 (JCPDS Card 18-0453, 20-1020, 27-0184) were identified from the XRD. It was earlier reported that CuSe phase formed on the surfaces and grain boundaries in polycrystalline films, grown under Cu- excess conditions.¹⁹ Presence of solid or liquid Cu_xSe phase, at the surface or within the film, promotes growth of large grains by enhancing diffusion or through the use of a liquid phase epitaxy-like process.²⁰ In the present study also the grain size was found to be increased for Cu excess sample CIS52 (24nm). However any excess Cu_xSe phase is detrimental to CuInSe₂ devices due to its highly conductive nature.

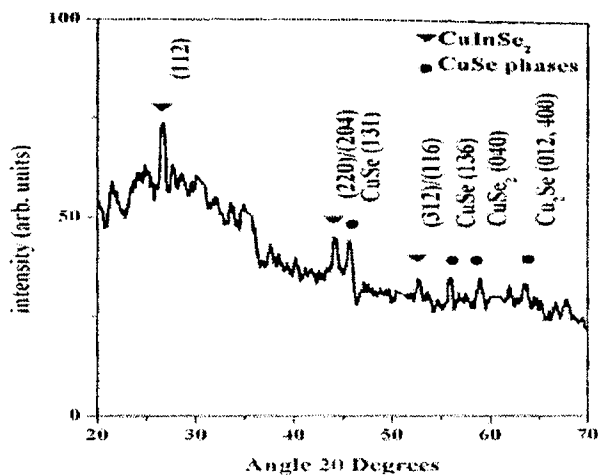


Fig 3.8: X-ray Diffraction pattern of CIS52

At the same time, In_2Se_3 phase (JCPDS Card 20-0496) was found for In-rich films CIS210 (Fig 3.9).

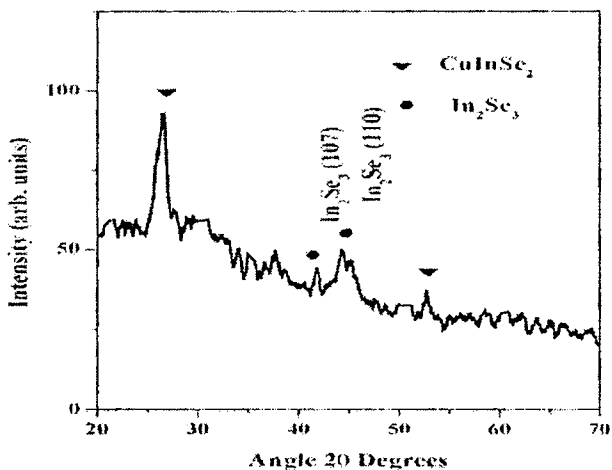


Fig 3.9: X-ray Diffraction pattern of CIS210

In-rich films possess high density of defect states, reducing the grain size. For the fabrication of solar cells, slightly In-rich films (In concentration about 26%) were preferred. It is reported that this In-rich stoichiometry helps to form a thin n-type layer at the surface (an ordered vacancy compound), which enhances the efficiency of the solar

cell.²¹ For nearly stoichiometric film CIS48 (Fig 3.10), only peaks of CuInSe₂ were visible. No binary phases were seen.

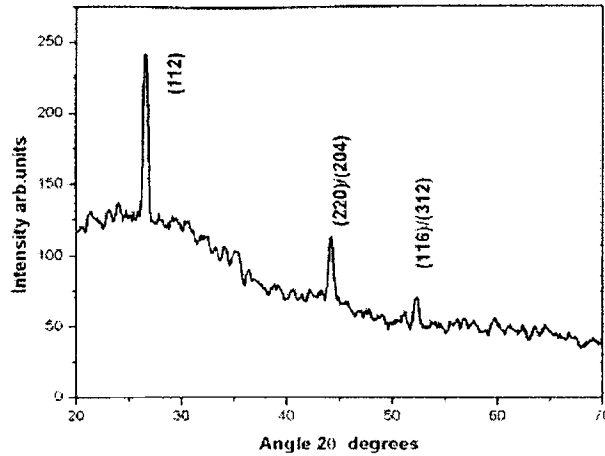


Fig 3.10: X-ray Diffraction pattern of CIS48

3.9 Raman analysis

Raman analysis was carried out on the samples CIS48, CIS52 and CIS210 to confirm the structure and chemical state. Optical vibrational modes of CuInSe₂ thin films were obtained from the analysis of the Raman spectra (Fig 3.11).

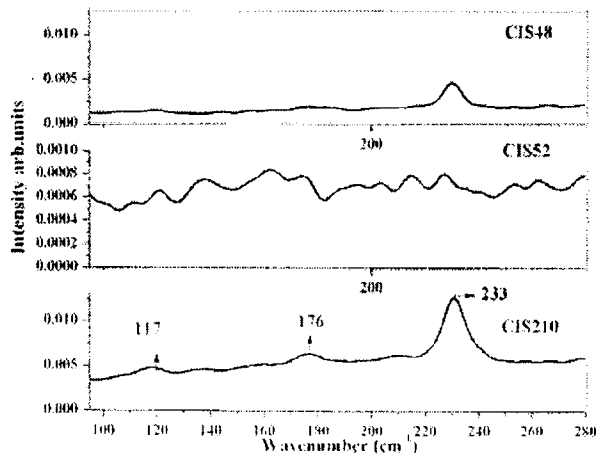


Fig 3.11: Raman spectra of the samples CIS48, CIS52 and CIS210

In all the samples, a prominent mode at 233cm^{-1} was observed which corresponded to the sphalerite phase of CIS. Three modes of vibration were observed for CIS210 at 117, 176 and 233 cm^{-1} with prominent one at 233 cm^{-1} . The mode at 117 cm^{-1} was assigned to the B_1 symmetry. This B_1 mode corresponds to the frequency of vibration of Cu and In atoms in antiphase. In this case, the polarizability change during the vibration due to the stretching of the Cu-In bond is partially compensated by the compression of the In-Se bond and hence this mode is very weak. Frequency of this mode is given by.²²

$$\nu = k(M_{Cu} + M_{In})^{1/2} (M_{Cu}M_{In})^{-1/2} \quad (3.1)$$

Vibrational mode at 176 cm^{-1} was assigned to A_1 symmetry and this mode gave the strongest line generally observed in the Raman spectra of I-III-VI chalcopyrite compounds. In this mode, Se atoms vibrate in the x-y plane with Cu and In atoms at rest. Hence frequency of this mode is associated with Se mass and the cations–Se bond stretching forces, describing the interaction between nearest neighbours. The frequency of the A_1 mode is given by

$$\nu = \left(\frac{k}{M_{Se}} \right)^{1/2} \quad (3.2)$$

where k is the force constant and M_{Se} , mass of Se atom. Dependence of ν on these force constants can be expressed as

$$\nu^2(A_1) = 2 \frac{(\alpha_{Cu-Se} + \alpha_{In-Se})}{M_{Se}} \quad (3.3)$$

Here α_{Cu-Se} and α_{In-Se} are the bond-stretching constants between the corresponding atoms²³. Because of the dependence on force constants, position of this mode directly depends on the atoms surrounding Se.²⁴ The A_1 mode was attributed to vibration of Se atoms, with Cu and In atoms at rest.²⁴⁻²⁶

In the present study, we observed the prominent peak at 233 cm^{-1} and it was assigned to B_2 or E symmetry. This peak was considered to be from sphalerite phase of CIS²⁷ and

related to the phonon mode of In-Se bond.²⁸ The relative intensity of this peak was much greater for the In-rich film CIS210. Here the prominence of In-Se bond can be assumed.

Peak position for the sample CIS52 was slightly (168 cm^{-1}) less than that obtained from the other samples. Since the force of interaction between selenium atoms and cation atoms mainly determine the vibrational frequency, vacancies at anion site would effectively reduce the A_1 mode frequency²⁹. In the case of CIS52, the small shift in peak position of A_1 mode might be due to the vacancies at indium site. EDAX measurements on this particular sample showed a deficiency of In (table3.7).

Raman spectra of CIS48 showed single peak at 233cm^{-1} , which corresponded to the sphalerite phase of CuInSe_2 . Combining the observations from Raman Analysis and XRD, it was concluded that the CuInSe_2 film in the present study was having sphalerite phase, which is a disordered version of chalcopyrite structure.

3.10 AFM analysis

Fig.3.12 and 3.13 illustrate the 2D and 3D AFM micrographs of Cu-rich (CIS52) and In-rich (CIS210) films. It showed that both these films were free of void and pinholes.

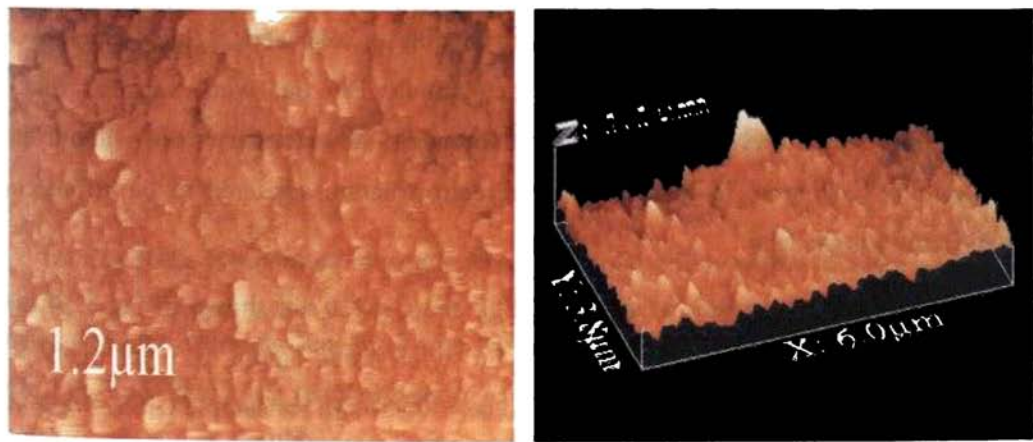


Figure.3.12: 2D and 3D AFM micrographs of CIS52

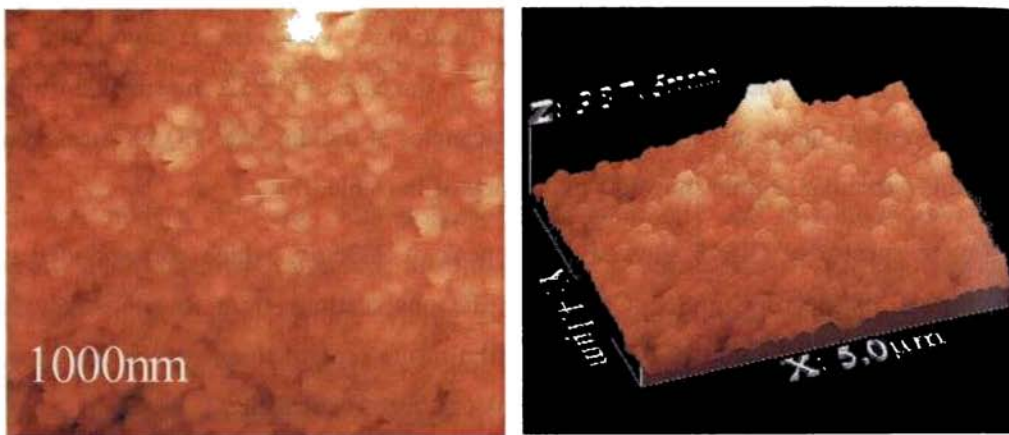


Figure.3.13: 2D and 3D AFM micrographs of CIS210

In indium rich samples, grains were evenly distributed and spherical growth was also observed [Fig 3.13]. But Cu-rich films had well-separated pyramidal islands and were evenly distributed [Fig 3.12]. This kind of surface structure has potential application as it reduces reflection loss and enhances light trapping in solar cells.³⁰ Such structures were earlier reported as a consequence of wet-etching. But our work suggests that such structures can be developed by the variation of film stoichiometry itself without the use of etching technique. In general, surface microstructure appeared to be influenced by Cu/In ratio in the film.

The stylus surface profile for sample CIS52 and CIS210 are shown in Fig 3.14 (a) and (b). The roughness was obtained using the stylus probe having a 5 μm diamond tip, where the average roughness was found to be 130-110 nm for sample CIS52 while it was found to be 15-30 nm for sample CIS210.

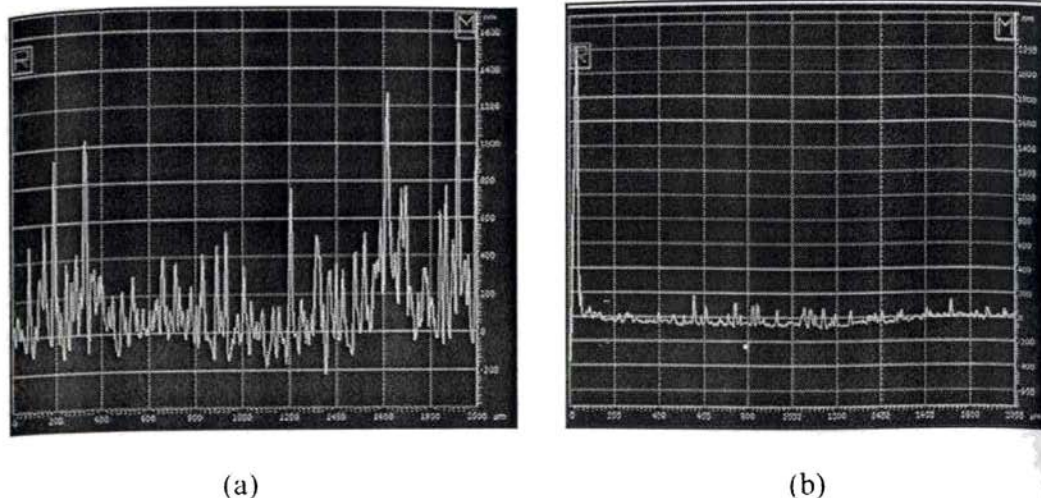


Fig 3.14: Surface Roughness profile for sample (a) CIS52 and (b) CIS210

3.11 Photoluminescence studies

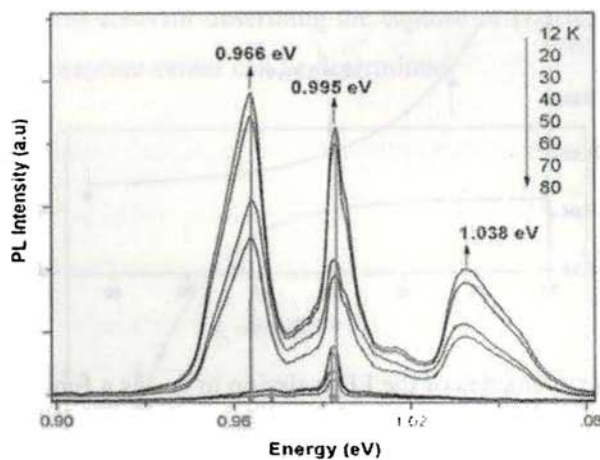


Fig 3.15: Temperature dependence of PL emission in sample CIS48.

PL measurements were carried out in the temperature range 12K-300K for the sample CIS48. Fig 3.15 shows the temperature dependent PL spectra of sample CIS48. Three distinct PL emissions could be obtained from the films, centered at 1.038 eV, 0.995 eV

and 0.966 eV. The highest PL emission was at 1.038 eV and it possessed a 'high energy tail' going up to 1.076 eV and this was quenched above 40K.

Fig 3.16 represents the plot of log of ratio of the intensity (I_{FE}/I_A) versus $1000/T$ fitted using the equation

$$I_{FE} / I_A = \exp(-\Delta E / kT) \quad (3.4)$$

For ΔE , a value of ~ 5 meV was obtained which agreed with the 'exciton binding energy' in CuInSe_2 .³¹⁻³³ Hence it was concluded that the 1.038 eV emission was a Free Exciton (FE) emission in this sample.

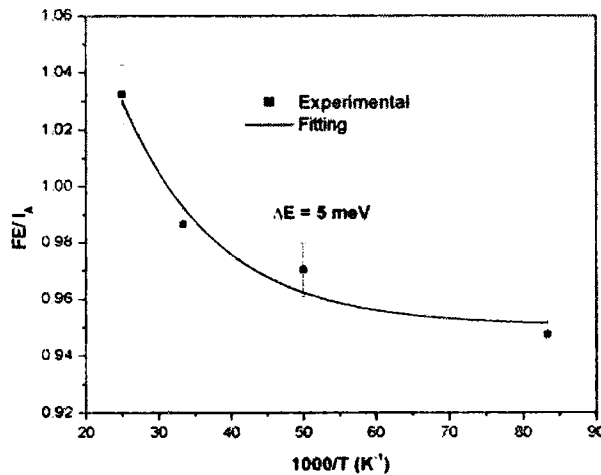


Fig 3.16: Ratio of the intensities of the FE emission to I_A , as a function of temperature

The emission at 0.995 eV was present up to 80 K in this sample. As the temperature was raised there was a shift in the peak energy position towards the lower energy side. This was evident from the temperature dependence of this emission (Fig 3.15) and was characteristic of a donor-acceptor pair (DAP) transition. The emission energy of a DAP pair at a distance r is given by equation

$$h\nu = E_g - (E_A + E_D) + e^2/\epsilon r \quad (3.5)$$

where E_g is the band gap, E_A and E_D are the acceptor and donor levels, ϵ is the dielectric constant and r is the separation of the DA pair involved in the transition.³⁴ Assuming that the Coulomb term in equation (3.5) is negligible, the binding energy of the donor-acceptor pair impurity for the emission at 0.995 eV was determined to be 47 meV. Dimstorfer et al had also observed a DAP transition in this energy scale and assigned it to a donor at 10 meV and the ionized acceptor complex $[Cu_{In}-Cu_I]$ at 40 meV.³⁵ The sustenance to high temperature for this emission was another proof to the DAP dynamics.

The activation energy of the shallower center among the DAP can be calculated by fitting the plot of logarithmic PL intensity vs $1000/T$ as shown in fig 3.17. Using the equation (3.6), describing the thermal quenching of PL in semiconductors.³⁶

$$I(T) = I(0) / [1 + C \exp(-\Delta E / k_B T)] \quad (3.6)$$

where $I(T)$ is the intensity at the temperature T , $I(0)$ is intensity at absolute zero and C is a temperature independent constant describing the capture of carriers at a center, ΔE the activation energy of the capture center can be determined.

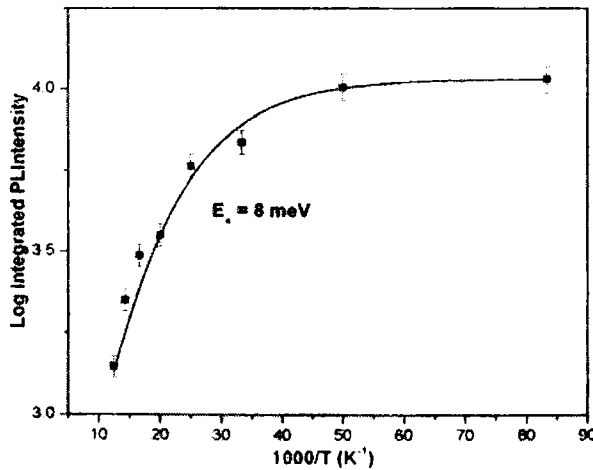


Fig 3.17: Plot of $1000/T$ versus logarithmic PL intensity fitted using expression 3.6 for the emission at 0.995 eV.

The activation energy of the shallow center was found to be 8 meV which agreed with the reported activation energy for the singly ionized In_{Cu} donor level.³⁷ Using $E_D = 8$ meV, $h\nu = 0.995$ eV, $E_g = 1.042$ eV [low temperature E_g calculated from Varshni's equation: $E_g = E_{g0} + aT^2/(T+b)$ where E_{g0} is the low temperature band gap and a and b are two empirical parameters] neglecting the Coulomb term in equation (3.5), the activation energy of the acceptor E_A was found to be 39 meV. This agreed with the activation energy of the singly ionized V_{Cu} acceptor level, reported by Dagan et al and Masse et al.^{35, 38} Thus it could be concluded that the PL emission at 0.995 eV in this sample was from the $In_{Cu} - V_{Cu}$ DAP recombination. The sample stoichiometry was also supporting this, as the film was slightly In-rich.

The emission at 0.966 eV in the sample was quenched above 60 K. The peak position of this emission varied gradually when the temperature was raised from 12 to 40 K. Beyond this temperature, the position of the impurity shifted rapidly towards the high energy side. This gave conclusive evidence to the (e, A^0) free-to-bound nature of this transition. Using equation

$$E_{PL} = E_g - E_A + (1/2)k_B T_e \quad (3.7)$$

[where E_{PL} is the PL peak energy of (e, A_0) emission, E_g is the band gap energy, E_A is the ionization energy of acceptor impurities, k_B is Boltzmann's constant and T_e is the effective temperature of electrons in the conduction band], the activation of the acceptor impurity for this transition was obtained to be 77 meV which agreed closely to the activation energy of the ionized acceptor V_{In} level, reported by Rincon et al and Dagan et al.^{38,39} Thus it was concluded that the emission at 0.966 eV in this sample was due to the $CB - V_{In} (e, A^0)$ transition.

Three major defects present in this sample identified using PL technique are In_{Cu} at 8 meV, V_{Cu} at 39 meV and V_{In} at 77 meV. An excitonic binding energy of 5 meV was also observed in this measurement.

3.12 Temperature dependant conductivity

Temperature dependant conductivity measurements were performed on the samples CIS52, CIS210 and CIS48 in the temperature range 100-300 K. Among these, CIS52 showed metallic nature, i.e. the resistance increased with increase in temperature (Fig3.18). The EDAX result of this sample showed an increased concentration of Cu [41.24%]. This may be the reason for the metallic behavior of this sample.

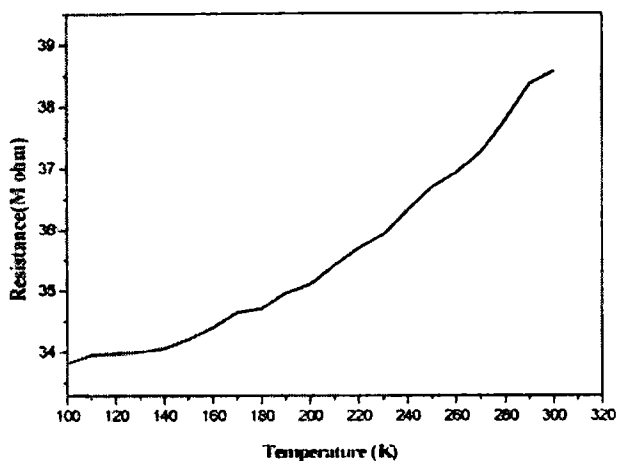


Fig 3.18: Plot of Temperature vs Resistance of the sample CIS52

The samples CIS48 and CIS210 showed negative temperature coefficient of resistance i.e. their resistance decreased with increase in temperature. Fig 3.19 shows the Arrhenius plot of $\ln(R)$ vs $1000/T$ for the sample CIS48. Three distinct regions are marked in the graph, indicating the change in the variation of resistance with temperature. Three slopes can be obtained from the graph, from which, the corresponding activation energies can be calculated.

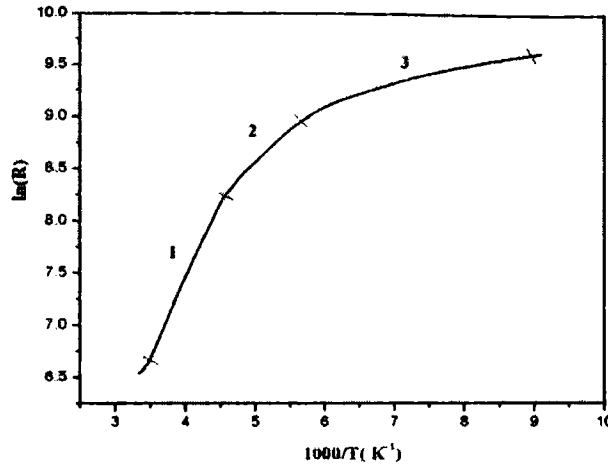


Fig 3.19: Arrhenius plot of $\ln(R)$ Vs $1000/T$ for the sample CIS48

Activation energy was calculated from the variation of ρ or σ with increase or decrease of temperature using the formula,

$$\sigma = \sigma_0 \exp\left(-\frac{E_a}{kT}\right) \quad (3.8)$$

where E_a = activation energy (or enthalpy) of the process and k is the Boltzmann constant. From the Arrhenius plot, E_a is calculated as

$$E_a = 1000mk \quad (3.9)$$

where m is the slope of the plot. The three slopes in the plot resulted in three activation energies of 110 meV, 49 meV and 14 meV. Activation energy of 110 meV could be assigned to the vacancy of In (V_{In}). Rincon et al, through electrical studies, had assigned the same defect level to be between 110-130 meV while H Neumann et al had assigned it to be between 115-125 meV.^{40,41} The small difference in reported values was due to the screening effect originating from the presence of ionized defects. This effect reduces the activation energy of shallow acceptor or donor levels according to the expression.⁴²⁻⁴⁴

$$E_A = E_{A0} - \beta(N_A - N_D)^{1/3} \quad (3.10)$$

where E_{A0} is the acceptor activation energy in the dilute limit and $\beta \approx 3 \times 10^{-5} \text{ meV cm}^{-1}$ is the 'screening constant', of CuInSe_2 . Even though this sample was slightly In-rich, the possibility of this defect formation can not be fully ruled out. The sample was p-type and the formation energy of V_{In} defect is very low.⁴⁵ Another possibility is Cu_{In} ; but according to Zhang et al, the formation energy of V_{In} is less than that of Cu_{In} for a Cu-poor, In-rich p-type sample.⁴⁶ Hence the defect could be confirmed to be V_{In} defect level which is an acceptor level, contributing to p-type conductivity. The formation energy of these defects for a stoichiometric sample are given in the table 3.8.

Table 3.8: Formation energy of intrinsic defects in stoichiometric CuInSe_2

Intrinsic Defect	Formation energy (eV)	Electrical activity
In_{Cu}	1.4	Donor
Cu_{In}	1.5	Acceptor
V_{Se}	2.4	Donor
V_{Cu}	2.6	Acceptor
V_{In}	2.8	Acceptor
Cu_i	4.4	Donor
In_{Se}	5	Donor
Se_{In}	5.5	Acceptor
Cu_{Se}	7.5	Acceptor
Se_{Cu}	7.5	Donor
In_i	9.1	Donor
Se_i	22.4	Acceptor

The activation energy of 49meV could be assigned to the acceptor level, V_{Cu} .⁴⁰ Cu is weakly bonded and vacancy of Cu exists in almost all the films, irrespective of the composition. The order of formation energy of the defects for this sample is $V_{Cu} < In_{Cu} < V_{In} < Cu_{In} < Cu_i$.⁴⁶ The lowest formation energy of this defect also supports the argument. Activation energy of 14 meV corresponds to the In_{Cu} donor level. This defect can occur in the present case, as a consequence of the composition and formation energy. PL measurements also confirmed the existence of In_{Cu} and V_{Cu} defect levels in this sample. There was slight difference in the values of the activation energies for the defects obtained from the optical and electrical study. The shallow levels of V_{Cu} , In_{Cu} and V_{In} could be identified in CIS48.

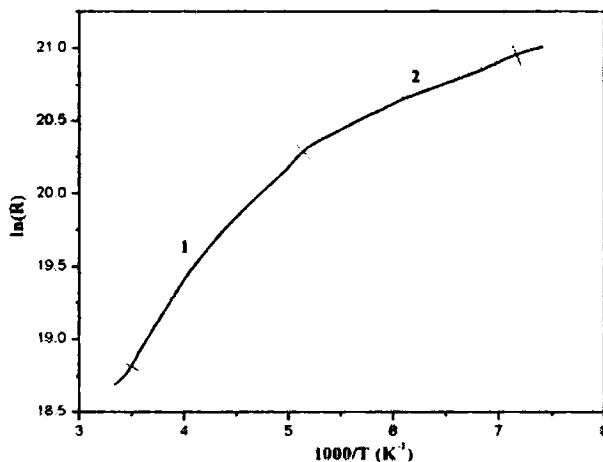


Fig 3.20: Arrhenius plot of CIS210

Fig 3.20 shows the Arrhenius plot of the sample CIS210, which was highly In-rich. Two distinct slopes are seen in the graph corresponding to activation energies of 75 meV and 25 meV respectively. The activation energy of 75 meV could be assigned to V_{Se} , and that at 25 meV to In_{Cu} which acts as donor levels. As the sample was n-type, these donor levels may be contributing to the conductivity.

3.13 Characteristics of optimized CdS thin film for solar cell fabrication

Fig 3.21 shows the X-ray diffraction pattern of the CdS thin film, deposited at a substrate of 50°C. The peak at 26.6° corresponds to hexagonal (002) plane. Peaks were also found at 27.9°, 47.87° and 52.13° corresponding to planes (101), (103) and (112).

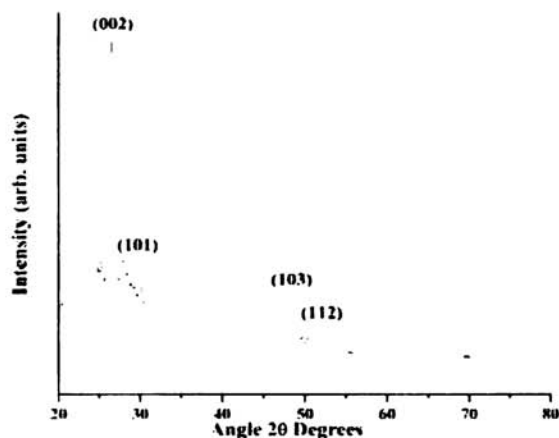


Fig 3.21: X-ray Diffraction pattern of CdS thin film

Grain size of the sample was calculated to be 19 nm. Figure 3.22 shows the Scanning Electron Microscopic image of CdS film prepared in the above condition. The image shows highly dense grains even though the grain size was low.

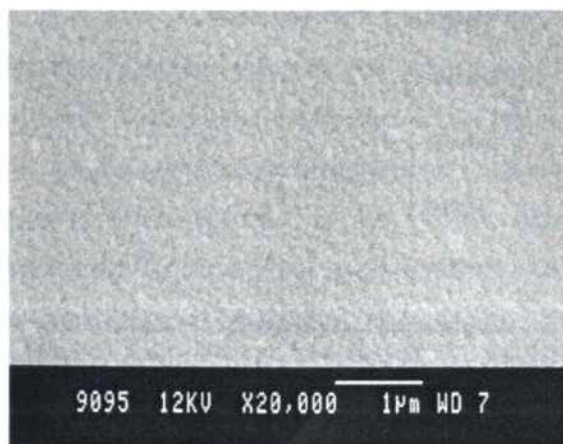


Fig 3.22: Scanning electron microscopic image of CdS

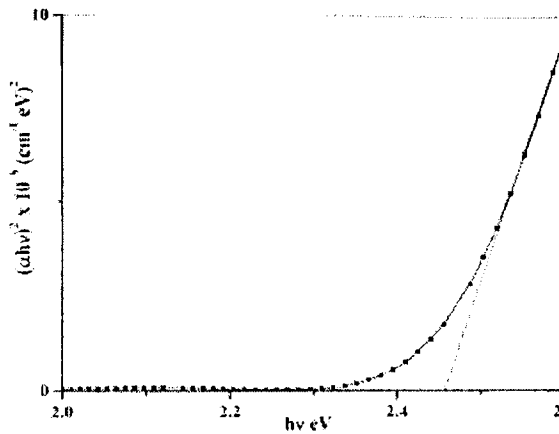


Fig 3.23: Absorption spectra of CdS

Fig 3.23 shows the absorption spectra of CdS film and the band gap obtained as 2.46eV. The sheet resistance was obtained as 603MΩ, from the I-V measurements in dark condition. Photosensitivity of 280 was obtained for this sample.

3.14 Device fabrication: Trial

An attempt for solar cell fabrication was made with CdS as buffer layer, Aluminium and Molybdenum as top and bottom electrodes. CdS thin films were prepared using thermal evaporation. The structure of the solar cell was Mo/CuInSe₂/CdS/Al.

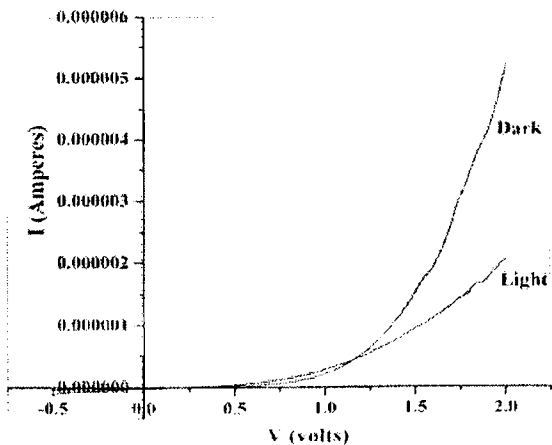


Fig 3.24: I-V characteristics of CuInSe₂/CdS junction

Even though the sample showed the I-V characteristics of a p-n junction, on illumination, photovoltaic effect could not be obtained (fig 3.24). Even after varying the concentration and deposition parameters, photovoltaic effect could not be observed. This technique had the disadvantage that, thickness of Se layer could not be increased beyond $0.25\mu\text{m}$ because the films develop the tendency to peel off beyond a certain dipping time during the CBD process. Hence the total CuInSe_2 thickness was restricted to $< 0.5\mu\text{m}$. The problems with this lower thickness are reduced absorption of incoming photons and also increased back surface recombination. As techniques like light trapping and back reflectors were not employed in this configuration, slightly increased thickness ($0.5\text{-}1\mu\text{m}$) should be used. In this technique, the overall absorber layer thickness was lower for getting considerable absorption of the photons. Unfortunately the thickness of the absorber layer could not be increased further so as to increase the absorption.

3.15 Conclusion

A cost-effective and eco-friendly method was used for the preparation of CuInSe_2 thin films using chemical bath deposited Selenium films. CuInSe_2 films were prepared through two different techniques (viz, Stacked Elemental Layer technique and Thermal diffusion of Copper into In_2Se_3 bilayer) using this chemical bath deposited Se as the bottom layer. Stoichiometry of the sample was varied over a wide range by varying Cu and/or In content. Though the films prepared using the two techniques showed same variation in crystallinity, grain size and band gap with Cu to In ratio, the photosensitivity was found to be more for those prepared using thermal diffusion of Cu into In_2Se_3 . The films showed good crystallinity with sphalerite structure which could be confirmed from XRD and Raman studies. Stoichiometry of the samples could be confirmed from EDAX measurements. The CuInSe_2 films prepared by the present technique using CBD Selenium layer were found to be free from voids and pinholes. Defect analysis was also performed using photoluminescence and temperature dependant conductivity studies.

Even though the technique was eco-friendly with the exclusion of highly toxic Se vapor and H_2Se , photovoltaic effect could not be observed at the $\text{CuInSe}_2/\text{CdS}$ junction. We

conclude that absorber layer thickness should be of the order of 0.5-1 μ m for efficient absorption of radiation and elimination of back surface recombination.

References

1. Kannan Ramanathan, Miguel A. Contreras, Craig L. Perkins, Sally Asher, Falah S. Hasoon, James Keane, David Young, Manuel Romero, Wyatt Metzger, Rommel Noufi, James Ward and Anna Duda, *Prog. Photovolt: Res. Appl.* **11** (2003) 225
2. L L Kazmerski, *Int. Mater. Rev.* **34** (1989) 185
3. F Abou El Fotouch, S A Al Kuhaimi, R Mustafa, D J Dulavy, L L Kazmerski, Photoluminescence of CuInSe₂ and its intrinsic defect states, 19th IEEE Specialist conf. May 4-8, 1989
4. R L Byer, H Kidal, R S Feigelson, *Appl. Phys. Lett.* **19** (1979) 237
5. M Lal, P K Batham, N Goyal, *Sol. Energy Mater. Sol. Cells* **36** (1995) 111
6. J. Kessler, C. Chityuttakan, J. Lu, J. Scholdstrom, L. Stolt, *Prog. Photovolt: Res. Appl.* **11** (2003) 319
7. C. M. Joseph, C. S. Menon, *J. Phys. D: Appl. Phys.* **34** (2001) 11431
8. C. Guillen, E. Galiano, J. Herrero *Thin Solid Films* **195** (1991) 137
9. P. K. Vidyadharan Pillai, K. P. Vijayakumar, P. S. Mukherjee, *Journal of Material Science Letters* **13** (1994) 1725
10. Piekozewski J, Loferski J.J, Beaulieu R, Beall J, Roessler B, Shewchun J, *Solar Energy Mater.* **2** (1980) 363
11. M Gossla, H Metzner, H C Mahnke, *J. Appl. Phys.*, Vol. **86**(7). (3624-3632), 1999
12. Abernathy C R, Bates C W, Anani A.A, Haba B, Smestad G, *Appl. Phys. Lett.* **45** (1984) 890
13. Grindle S P, Clark A H, Rezaie-Serej S, Falconer E, McNeily J, Kazmerski L L 1980, *J. Appl. Phys.* **51** (1980) 5464
14. M Casteleyn, M Burgelman, B Depuydt, Clemminck, *Proc. 12th European Photovoltaic Solar Energy Conference*, Amsterdam, 1994, p.604
15. K. Bindu, C. Sudhakartha, K. P. Vijayakumar, T. Abe and Y. Kashiwaba, *Sol. Energy Mater. Sol. Cells* **79**, (2003) 67
16. B. Tell and P. M. Bridenbaugh, *Phys. Rev. B.* **12**, (1975) 3330
17. Jacques. I. Pankove. Dover Publications, Inc, New York (1971)

18. S M Firoz Hasan, M A Subhan, Kh.M Mannan, *Optical Materials* **14**(2000) 329
19. T.Wada, N.Kohara, T.Negami, M.Nishitani, *J.Mater.Res.* **12** (1997) 1465
20. C. Rincon, F. J. Ramirez, *J. Appl. Phys.*, **72**(9) (1992) 4321
21. V Alberts, R Herberholz, T Walter, H W Schock, *J.Phys.D.Appl.Phys.***30**(1997) 2156
22. J. N. Gan, J. Tauc, V. G. Lambrecht Jr. and M. Robbins, *Phys. Rev B*, **13** (1976) 3610
23. C. Rincon, S.M.Waso, G.Martin, J.R.Huntzinger, A.Zwick, J.Galibert, *J. Appl. Phys.*, **85**(7) (1998) 3925
24. M. Tanda, S. Manaka, A. Yamada, M. Konagai and K.m Takahashi, *Jpn. J. Appl. Phys.* **32** (1993) 1913
25. M. Nishitani, T. Negami, S. Kohiki, M. Terauchi, T. Wada, T. Hirao, *J. Appl. Phys.* **74** (1993) 2067
26. C. Rincon, F. J. Ramirez, *J. Appl. Phys.*, **72** (1992) 4321
27. S. Shirakata, H. Kubo, C. Hamaguchi, S. Isomura, *Jpn. J. Appl. Phys* **36** (1997) L1394
28. M. Nishitani, T. Negami, M. Terauchi, T. Hirao, *Jpn.J. Appl. Phys.* **31** (1992) 192
29. S. Nomura, S. Ouchi, S. Endo, *Jpn. J. Appl. Phys.* **36** (1997) L1075
30. P. M. Varghese, D. R. Clarke, *J. Mater. Res.* **14**(3) (1999) 1039
31. Schön, J. H.; Bucher, E. *Appl. Phys. Lett.*, **73**(2) (1998) 211
32. V. Mudryi, I. V. Bodnar, V. F. Gremenok, I. A. Victorov, A. I. Patuk and I. A. Shakin, *Sol. Energy Mater. Sol. Cells*, **53**(3-4) (1998) 247
33. S. Niki, H. Shibata, P. J. Fons, A. Yamada, A. Obara, and Y. Makita, T. Kurafuji, S. Chichibu, and H. Nakanishi *Appl. Phys. Lett.* **67** (1995) 289
34. Zott, S. Leo, K. Ruckh M. and Schock , H.-W. *Appl. Phys. Lett.* **68**(8) (1996) 1144
35. Dimstorfer I. Burkhardt W. Meyer B.K. Ostapenko S. Karg F. *Solid State Communications*, **116** (2000) 87
36. Dean, J.P. *Phys.Rev.***157**, (1967) 655
37. Shay, J. L. and Wernick, J. H. *Ternary Chalcopyrite Semiconductors: Growth, Electronic Properties and Applications* (Pergamon, Oxford, 1975)118
38. Dagan, G. Abou-Elfotouh, F. Dunlavy, D.J. Matson, R.J. and Cahen. D. *Chem. Mater.* **2** (1990) 286
39. Rincon, C. Arsene, M.A. Wasim, S.M. Voillot, F. Peyrade, J.P. Bocaranda, P. Albacete, *A. Materials Letters* **29** (1996) 87
40. C Rincon, R Marquez. *Journal of Physics and Chemistry of Solids* **60**(1999) 1865

-
41. H Neumann, E Nowak, Cryst Res Technol. **18**(1983) 779
 42. H Neumann, E Nowak, G Kuhn, Cryst Res Technol. **16**(1981) 1369
 43. C Rincon, S M Wasim, J L Ochoa, Phys.Status Solidi A **148**(1995) 251
 44. J Monecke, W Siegel, E Ziegler, G Kuhnel, Phys.Status Solodi B **103**(1981)269
 45. S M Wasim, Solar Cells **16**(1986) 289
 46. S B Zhang, Su-Huai Wei, Alex Zunger, Phys.Rev B **57**(16)9642

Modified Technique for Deposition of CuInSe₂ Thin Films Using Sequential Elemental Evaporation and Characterization

4.1 Introduction

In the last chapter, an economical and eco-friendly method was demonstrated for the deposition of CuInSe₂ (CIS) thin films in which chemically deposited Selenium was used. Optimization of these CuInSe₂ films was carried out and with this optimized sample, an attempt to device fabrication was also made. Here CdS was the buffer layer. But photovoltaic effect could not be observed with this CuInSe₂/CdS junction. One of the possible reasons for this could have been the reduced thickness of the absorber layer, which was < 0.5 μm. For the fabrication of solar cells, thickness of the absorber layer should be greater than 0.5 μm in order to have efficient absorption of the solar radiation, even though theoretical calculation predicts efficiency above 17% for an optimized cell with a thickness of 0.3 μm.¹ The main draw back of the above mentioned deposition technique was that the thickness of the Se layer could not be increased above a certain limit. As the thickness goes beyond this limit, the films started to peel off. Hence the overall thickness of the CuInSe₂ films, prepared using Se layer deposited using CBD technique, was limited to less than 0.5 μm.

With the aim of fabricating a solar cell with better efficiency, a modified technique was developed using vacuum evaporation, whereby the film thickness could be increased. In literature, there are many reports on deposition of CuInSe₂ thin films using vacuum evaporation.²⁻⁶ Interestingly, the record-breaking 19.9% efficient cell was also fabricated using co-evaporation technique.⁷ In all the reported techniques, Cu, In and Se were

deposited either in elemental or in compound form, at very high substrate temperatures starting from 350°C. Moreover, these processes are complex and controlling the deposition parameters is also difficult. In the present work, CuInSe₂ thin films were deposited through sequential evaporation of Se, In and Cu, at moderately low substrate temperature. This method of sequential evaporation is simpler than co-evaporation technique and control of stoichiometry could be easily achieved. We could deposit highly stoichiometric samples through this method. Here we made an attempt to deposit sub-micrometre thick absorber layers and fabricate solar cells using these.

The key issues in the field of CuInSe₂ based solar cells are, reducing the thickness of CIS and the replacement of CdS with non-toxic and low absorbing materials. Typical absorber layer thickness of today's solar cell ranges between 2 to 3 μm. Reducing the thickness of the absorber layer is one of the challenges to minimize the processing time and material usage, particularly of Indium. Work is going on to replace Indium partially by Ga, Al etc. The main reasons to find an alternative buffer layer are the following:

- (a) The expected environmental risks arising from implementation of a CBD CdS process in a CIGS module production line could be avoided.
- (b) The expected technological problems caused by a non-vacuum CBD process in a vacuum line could be separated.
- (c) The potential of increasing current generation in the spectral region of 350–550 nm, and thereby increasing the cell efficiency is another possibility.
- (d) As the presence of Cadmium in electrical or electronic equipment has already been prohibited through legal regulations in different countries, there is a marketing problem for the Cd-containing CIGS-based thin-film modules today.

In₂S₃, ZnS, ZnO, ZnSe, In₂Se₃, InZnSe_x, SnS₂, SnO₂ are reported to be the possible alternative buffer layers for CIS solar cells. In the present work, we chose In₂S₃ prepared through 'chemical spray pyrolysis' as the buffer layer. This was a novel approach as CuInSe₂/In₂S₃ junctions. This is rather rare as most of the reports are on the devices prepared using vacuum evaporation technique for the entire cell.

4.2 Experimental details

Soda lime glass was used as the substrate in this work. Samples were prepared using thermal evaporation of Cu, In and Se at a pressure of 10^{-5} mbar. Quantity of Cu, In and Se to be evaporated was selected such that the film stoichiometry was 1:1:2. Rates of evaporation were 0.5 nm/sec, 0.3 nm/sec and 0.2 nm/sec for Se, In and Cu respectively. After deposition, the samples were annealed at 400°C for one hour at a pressure of 10^{-5} mbar resulting in the formation of CuInSe_2 .

4.3 Optimization of deposition process

Molybdenum (Mo) coated glass (thickness of Mo ~ 80 Å) was used as the substrate in the optimization work. The Mo substrate was highly resistive so that it did not affect the conductivity measurements of the CIS sample. The deposition process was optimized by varying parameters like, substrate temperature, annealing rate and the sequence in which the three layers were deposited. As a primary step, deposition was carried out by sequential evaporation of Se, In and Cu to get the structure of glass/Mo/Se/In/Cu, keeping the substrate at room temperature. This sample was named as CIS1. After deposition, the sample was annealed at 400°C [heating rate $-2.5^{\circ}\text{C}/\text{min}$] for one hour at a pressure of 10^{-5} mbar resulting in the formation of CuInSe_2 .

A point to be noticed in this course is that an intermediate annealing at 150°C (near the melting point of In) was carried out for these samples, before increasing the temperature to 400°C . This process helped to form Cu-In alloy and subsequent selenization of this alloy lead to formation of CuInSe_2 .

From the X-ray diffractogram of CIS1 (Fig 4.1), single phase CuInSe_2 with chalcopyrite structure was identified. Peaks were at angles $2\theta=17.1^{\circ}$, 26.6° , 35.45° , 44.02° , 52.32° , 64.32° and 70.8° respectively. On comparing the observed d-spacing with powder diffraction standards (JCPDS card 23-209), planes were identified as (103) at $2\theta=17.1^{\circ}$, (112) at 26.6° , (211) at 35.45° , (220)/(204) at 44.02° , (116)/(312) at 52.3° , (400) at 65.02° and (316) at 71.51° . The sample showed strong preferential orientation along (112) plane. The characteristic chalcopyrite peaks were obtained at (103), (211) and (400) planes.

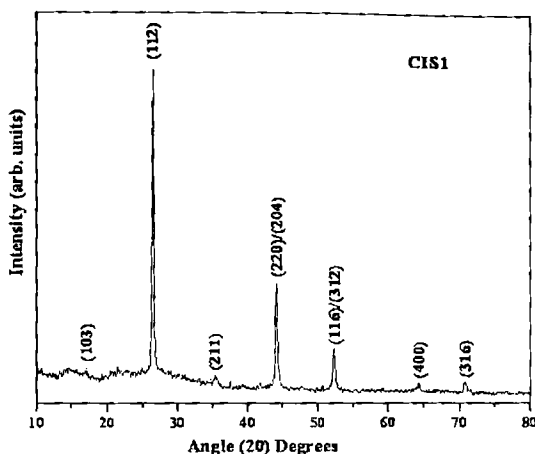


Fig.4.1: X-ray diffractogram of CIS1

Grain size was calculated using Debye-Scherrer's formula⁸, and was found to be of the order of 45 nm. However the samples were found to be highly porous in nature to the naked eye. Five samples of dimension $3.5 \times 1 \text{ cm}^2$ were prepared at a time. Among these, at least four were showing similar XRD pattern in spite of being porous in appearance. This proved that the structural properties were repeatable in this type of preparation.

In order to reduce the porosity, the deposition process was repeated by reducing the annealing temperature to 300°C (sample CIS2) keeping all the other deposition parameters identical to that used for sample CIS1. XRD pattern of sample annealed at 300°C is given in fig 4.2. It showed that reduction in annealing temperature lead to the formation of InSe phase together with CuInSe_2 phase.

The peak at 23.3° was corresponding to InSe phase (JCPDS card27-0244). Moreover, on reducing the annealing temperature to 300°C , porous nature of the film did not change and resulted in the decrease of crystallinity compared to the samples annealed at 400°C . The temperature of 400°C has been reported to be the optimum temperature for the deposition of CIS by many authors.^{9,10}

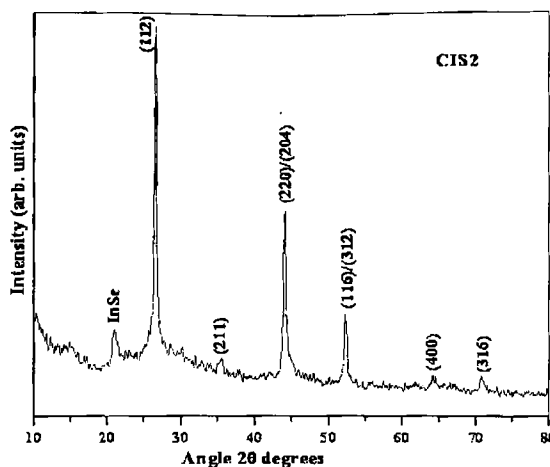


Fig.4.2: X-ray diffractogram of CIS2

In the next trial, Se was deposited at a substrate temperature of 50°C, while In and Cu layers were deposited at room temperature, followed by annealing of the entire structure at 400°C at a pressure of 2×10^{-5} mbar and this set of samples was named as CIS3. Visual examination revealed reduction in the porosity of the film. With the increase in substrate temperature, the surface mobility of the adsorbed species increased because of which they interacted among themselves, resulting in continuous films with well-defined grains of large size.

As the next step, samples were prepared by keeping the deposition parameters identical to that of CIS3, but changing the heating rate while annealing at 400°C. The heating rate was reduced to 1.2°C /minute from 2.5°C /minute. These samples were named as CIS4. Crystallinity of the sample also improved slightly. But these were still showing porous nature. Fig 4.3 reveals the XRD pattern of samples CIS3 and CIS4 which clearly showed that CIS3 was a better polycrystalline sample compared to CIS4.

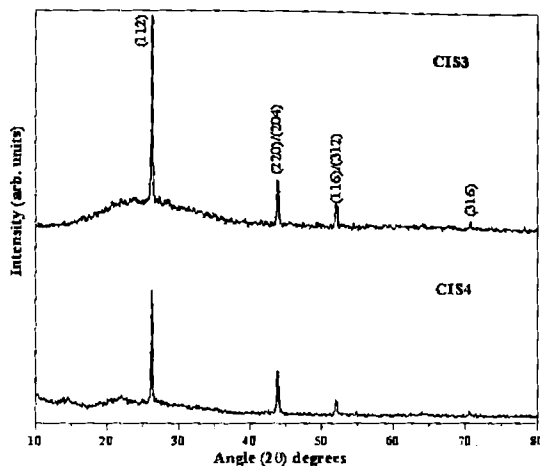


Fig 4.3: CIS3 X-ray diffractograms of and CIS4

The deposition process was further modified by depositing 'In' first at a substrate temperature of 100°C, followed by Se at 50°C and Cu at room temperature. Such samples [named as CIS5] exhibited better crystallinity without the porous nature. This might be due to the enhanced surface mobility of the adsorbed In atoms which filled the voids. Grain size increased to 60 nm even though this value was less compared to that already reported. Only three prominent peaks were observed corresponding to planes (112) at $2\theta = 26.6^\circ$, (220)/(204) at 44.1° and (116)/(312) at 52.3° respectively (fig 4.4). The characteristic chalcopyrite peaks were absent in these samples.

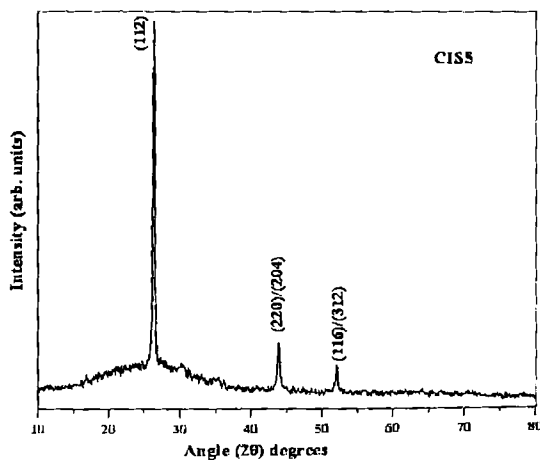


Fig.4.4: X-ray diffractogram of CIS5

Following the same deposition process as that of sample CIS5, deposition was repeated without keeping the samples at 150°C for one hour during the annealing process. These were named as CIS6. Fig 4.5 shows the XRD spectra of these. The sample showed the same polycrystalline quality as that of CIS5, with grain size of 57 nm. This is almost equal to that of CIS5. Hence it was concluded that, when ‘In’ was evaporated at a substrate temperature of 100°C, intermediate annealing at 150°C was not required. This could save time during deposition, making this method easier. Hence this method was followed for further fabrication process. This process was repeated to check consistency in the results and the properties of the repeated sample showed negligible variations.

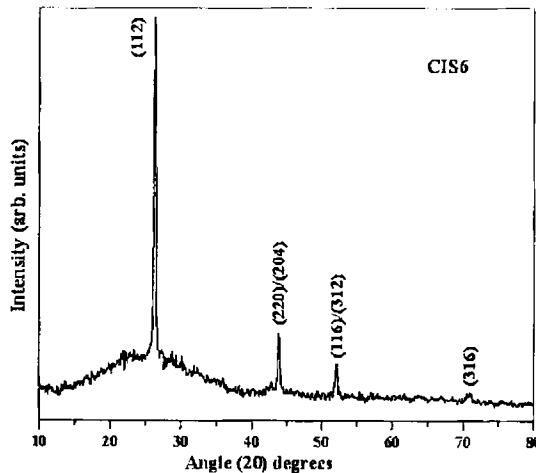


Fig.4.5: X-ray diffractogram of CIS6

To evaluate the degree of crystallinity of these samples, Preferred Orientation Quality (POQ_{hkl}) in the (hkl) direction was calculated using the formula ¹¹;

$$POQ_{hkl} = \frac{I_{hkl}}{\sum_{hkl} I_{hkl} (FWHM_{hkl} Ri_{hkl})} \quad (4.1)$$

where I_{hkl} is the actual intensity of the diffracting line hkl, $FWHM_{hkl}$ is their full width at half maximum and Ri_{hkl} is the relative intensity of that particular line, in a powder sample. POQ was calculated for all samples and the values are given in table 4.1.

Table 4.1: POQ values of the samples CIS1 to CIS6

Sample name	POQ
CIS1	1.8
CIS2	1.5
CIS3	2.5
CIS4	2.2
CIS5	2.2
CIS6	2.4

From the table, it could be seen that POQ was maximum for CIS3 which showed that it was more crystalline. But the sample was visibly porous. For CIS1 and CIS2, POQ was below 2 and for samples CIS4 and CIS5, the POQ value is more or less the same. Considering the visual appearance, XRD peaks as well as the POQ value, CIS6 could be taken as the best sample in this group. Compositional, optical, electrical and morphological analyses of this sample were carried out.

4.4 Characterization of Optimized sample

4.4.1 EDAX analysis

Atomic concentration of the constituent elements of CIS6 was determined using EDAX by applying an acceleration voltage of 20kV. The EDAX spectrum is shown in fig.4.6. EDAX spot analysis across the entire sample revealed high degree of compositional uniformity with typical values around 29.01 at%, 17.95 at% and 53.54 at% for Cu, In and Se respectively. This very well indicated that sample was homogeneous. Even though the masses evaporated were for stoichiometric with a ratio 1:1:2, the sample was Cu-rich. As the melting point of In is only 150°C, there is a high probability for Indium getting lost

during the annealing process at 400°C. This could be the reason as to why the films were Cu-rich.

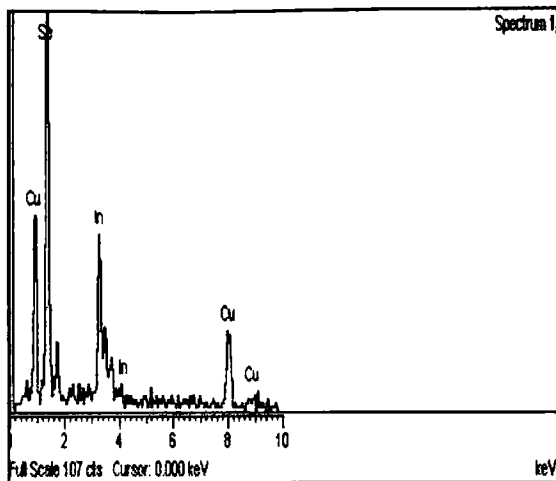


Fig.4.6: A typical EDAX spectrum of CuInSe_2

4.4.2 XPS analysis

Fig.4.7 shows the result of the 'XPS depth profile' analysis of CIS6. The results reveal that Cu and Se diffused into the 'In' layer due to annealing and this resulted in the formation of CuInSe_2 .

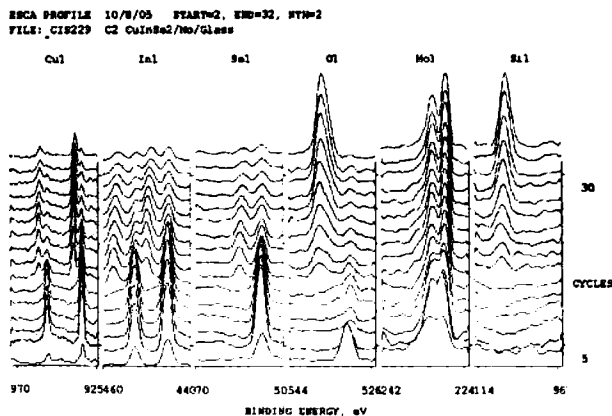


Fig.4.7: XPS depth profile of CuInSe_2

The binding energy values of Cu, In and Se were in agreement with the standard values reported earlier¹² and these are given in the table 4.2. A slight shift in BE of Cu, In and Se near the interface of film and the substrate was observed which could be due to the presence of oxygen in the substrate.

Table 4.2: Binding energies for the different elements in CIS

Element	Binding Energy (eV)
Cu2p _{3/2}	952.4
Cu2p _{1/2}	932.8
In3d _{5/2}	452.8
In3d _{3/2}	445.2
Se3d	54.8
Mo	231.3
Mo	229
O	531.1
O	530.4

From XPS analysis, we could conclude that, even with the Cu-rich composition, film existed in single phase, which is an indication of its large structural tolerance to off-stoichiometry. However, Mo diffused from the substrate up to the surface of the film. Two different binding energies were obtained for Mo, [231.3 and 229 meV]. These values were corresponding to two different phases of Molybdenum oxide namely, MoO₂ and MoO₃. Binding energies of oxygen also supported this assignment. Binding energy of Oxygen was 531.1 eV in MoO₂ and 530.4 eV in MoO₃.

4.4.3 Thickness measurement

Film thickness and sample surface roughness were determined from the one dimensional scan carried out by means of Dektak32 stylus profilometer. Thickness of the sample was found to be 0.79 μm while the average roughness was 93.6 nm. Thickness can be increased by multilayer deposition, if required.

4.4.4 Optical absorption

Absorption spectrum was recorded in the wavelength range 500 nm to 1500 nm for all the samples. Fig 4.8 shows the plot of $(\alpha h\nu)^2$ versus $h\nu$ for sample CIS6.

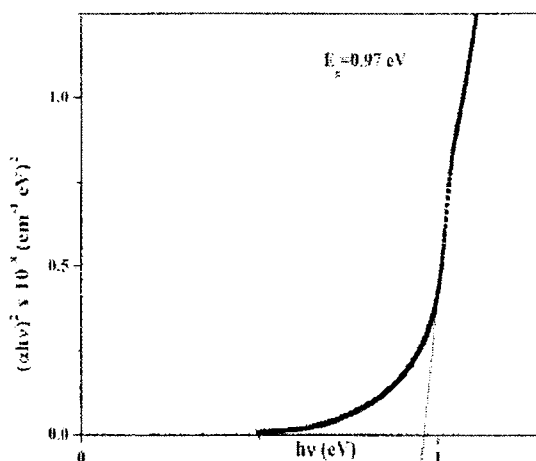


Fig.4.8: Absorption spectra of CuInSe_2

Band gap obtained, by extrapolating the linear portion of the $(\alpha h\nu)^2$ versus $h\nu$ graph to $h\nu$ axis [0.97 eV], was close to the reported value for Cu-rich films¹³. In all the films, there existed a second absorption edge at energy $\sim 1.1\text{eV}$. This absorption is attributed to the 'valence band splitting', a phenomenon commonly occurring in I-III-VI₂ semiconductors.

The valence band of CIS consists of three sub-bands. At the top, there is a broad band built up from Se-4p and Cu-3d states. Next is a narrower band formed from In-5s and Se-

4p bonding states. Finally, well-separated from the first two bands, there exists the Se-4s band. The uppermost valance band is lifted due to simultaneous influence of spin-orbit and crystal field interactions (tetragonal distortion). This splitting is owing to the following reasons.

- (1) Ordering of the metal cations relative to one another such that the unit cell is doubled along the optic axis
- (2) In the chalcopyrite structure, each cation (Cu and In) has four anions (Se) as nearest neighbours. The anion usually adopts an equilibrium position closer to one pair of cations than to the other. That means, the anions are not located at positions like $(\frac{1}{4}, \frac{1}{4}, \frac{1}{4})$; instead these are placed at $(\frac{1}{4}, \frac{1}{4}, \frac{1}{8})$ which make the In-Se and Cu-Se bond lengths unequal and
- (3) The chalcopyrite lattice is slightly compressed along the z-axis.¹⁴⁻¹⁷

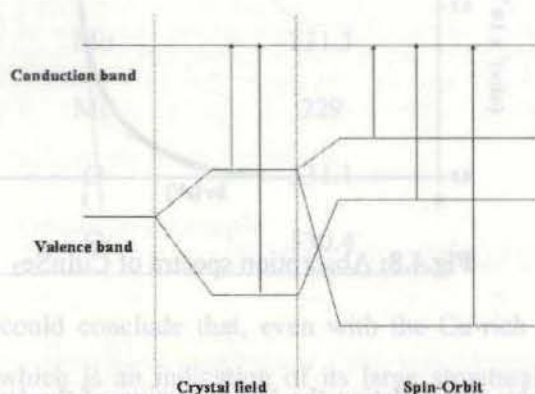


Fig 4.9: Splitting of the uppermost valence band in CuInSe_2

Fig 4.9 shows the valence-band splitting due to crystal field and spin-orbit interactions. The 3d or 4d electrons of the noble metal (Cu) hybridize with the p-like valence band due to proximity of their levels. This hybridization p-d resonance cause anion p-state and Cu-d band splitting. Transition can take place between conduction band and split valence bands which create additional absorption edge, as observed in the present case.

4.4.5 Electrical characterization

Hot probe measurement confirmed the samples to be p-type. Generally p-type samples are Cu-rich¹⁸ and this was consistent with EDAX measurement. Resistivity of the sample was found to be 3 Ωcm , from the dark I-V characteristics. For fabrication of solar cells, resistivity of the order of 10 Ωcm is usually preferred. The resistivity could be varied by varying the composition in the film.

4.4.6 Temperature dependant conductivity measurements

Defect levels were identified using temperature dependant conductivity measurements. Measurement was performed in the temperature range 100°K- 400°K under 'dark condition'. The Arrhenius plot of conductivity (fig.4.10) indicated two distinct slopes of activation energies 30 meV and 130 meV. These values agreed with the activation energies of Cu_{In}^- and V_{In}^- respectively.^{20,21} Since the film was Cu-rich, the probability of formation of these defects was high. These are the acceptor levels contributing to p-type conductivity.

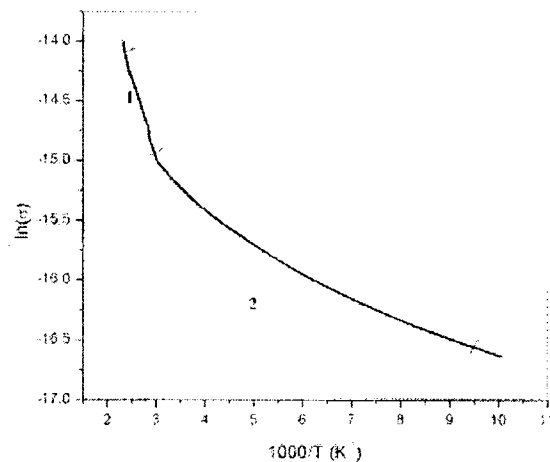


Fig 4.10: Temperature dependant conductivity of CuInSe_2

4.4.7 Morphological analysis

Morphological analysis of CIS6 was carried out using Scanning Electron Microscopy (SEM) and Atomic Force Microscopy (AFM). The image of the sample obtained from SEM analysis is given in fig.4.11 which shows that the film surface was smooth and uniform. It could also be seen that the sample was free of pinholes and micro-cracks.

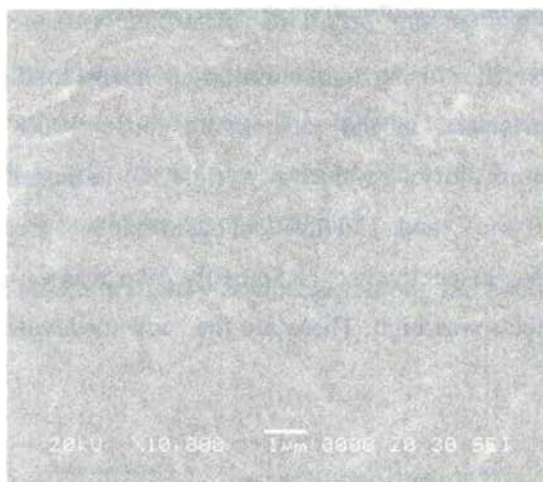


Fig 4.11: Scanning electron microscopic image of CuInSe₂

Fig 4.12 shows three dimensional AFM image of CIS6. From AFM, pyramidal structure of the grains could be seen, which is a characteristic of Cu-rich CuInSe₂ thin films. This kind of surface structure can be used to increase light trapping.²² Sample roughness was calculated from an area of 1 μ m x 1 μ m . The RMS roughness was found to be 26 nm which was comparable to that obtained from the stylus profilometer(93.6nm).

The two dimensional AFM image (fig.4.13) showed that the grain size varied in a wide range, from 75 nm to 200 nm and was different from the grain size obtained using Debye-Scherrer formula. From XRD analysis, the average grain size was calculated as 57 nm. Müller et al assigned the value calculated from this formula as “domain size” and one grain contains several domains.²³ From AFM study, we could get grain size of the order of 200 nm and also sub-particles of size ~ 75nm which can be called as domains.

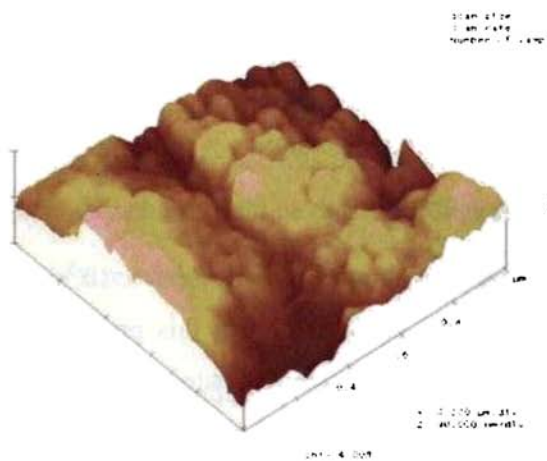


Fig.4.12: 3D AFM image in 1 x 1 µm area

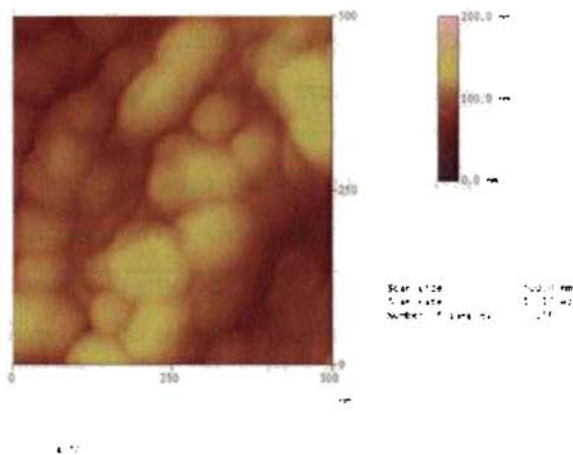


Fig. 4.13: 2D AFM image in 0.5 x 0.5 µm area

4.4.8 Inference

Stacked elemental layers of Cu, In and Se were deposited at moderately low substrate temperature. The deposition process was optimized as follows:

- (1) Structure of the film: Glass/In/Se/Cu

- (2) Indium evaporation at 100°C
- (3) Selenium evaporation at 50°C
- (4) Copper evaporation at room temperature
- (5) Annealing this layer at 400°C

All these processes were carried out at a pressure of 2×10^{-5} mbar. On analyzing the characteristics of the sample, we could infer that this procedure can be followed for further deposition. The samples were again deposited at the same condition to ensure repeatability and the film characteristics showed nearly the same values.

Films were characterized by varying the concentration of Cu, In and Se, one at a time.

4.5 Effect of variation of Cu

CuInSe₂ thin films were prepared by varying the concentration of Cu keeping In and Se concentrations constant at 110 and 170mg respectively. Concentration of Cu was varied from 40mg to 80mg. These samples were named as CIS7, CIS8, CIS9 and CIS10 depending up on concentration of Cu.

4.5.1 Structural characterization

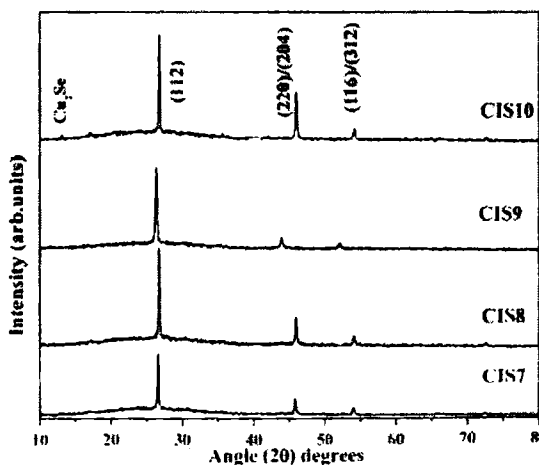


Fig.4.14: X-ray diffractograms of samples CIS7 to CIS10

Fig.4.14 shows the X-ray diffraction pattern of the samples CIS7, CIS8, CIS9 and CIS10. All the films were preferentially oriented along the (112) plane. Peaks were corresponding to planes (220)/(204) and (312)/(116). In addition, CIS4 showed a peak at 13.14° . The calculated d value of this peak was 6.73\AA , corresponding to (030) plane of Cu_2Se . Formation of this binary phase could be due to the higher Cu concentration.

POQ_{hkl} factor and the grain size were calculated for all samples and the values are given in Table 4.3.

Table 4.3: Grain size and POQ values of Cu varied samples

Sample name	POQ	Grain size nm
CIS7	2.2	58
CIS8	2.6	58
CIS9	2.4	33
CIS10	2.3	57

From the table 4.3, it could be seen that, POQ increased to 2.6 for CIS8 and then decreased with further increase in Cu. Grain sizes of the samples were comparable except CIS9 for which it decreased drastically to 33nm. But on considering POQ values, this sample can be considered to be more crystalline than CIS7 and CIS10. However, the grain size obtained through this deposition technique was smaller compared to other reported results obtained using evaporation techniques. Smaller grain size lead to an increase in grain boundaries which cause grain boundary scattering. This degrades conductivity of the samples. Also grain boundaries create potentials which are known to hamper the device performance. Controversial arguments exist about the role of the 'grain boundary potential'. According to some reports, grain boundary potential has beneficial effects in CuInSe_2 solar cell. even though conclusive evidence in this direction is still missing.²³⁻²⁵

The calculated values of lattice constants a, b and c are given in the table 4.4 and these values were comparable with the reported ones.²⁶ Among these, 'a' was high for CIS9, which had the lowest grain size. In the CIS lattice, tetragonal distortion occurs due to the excess and deficiency of bond charge in the In-Se and Cu-Se bonds respectively. This results in shortening of the In-Se bond, compared to the Cu-Se bond with a corresponding shift in the anion (sub-lattice displacement). The In-Se tetrahedron is consequently more rigid and shows little distortion, while Cu-Se tetrahedron is considerably distorted. The bond charge distribution also results in the tetragonal compression because the Cu-Se-In bond-bending force constant is not equal to the average of the corresponding Cu-Se-Cu and In-Se-In force constants and bond-bending energy is lowered by compression.¹⁵ The values of tetragonal distortion, $[\frac{2a}{c} - 1]$ is also shown in table 4.4. With decrease in 'a', tetragonal distortion becomes negative.

Table 4.4: Lattice constants and tetragonal distortion of the CuInSe₂ lattice

Sample name	Lattice parameters in Å		Tetragonal distortion: (2a/c)-1
	a, b	c	
CIS7	5.84	11.52	0.014
CIS8	5.76	11.61	-0.007
CIS9	5.94	11.48	0.035
CIS10	5.74	11.63	-0.012

4.5.2 Thickness measurements

Thickness measurement using stylus profilometer revealed that single layer CuInSe₂ was ~ 0.55 μm thick. Fig. 4.15 shows the stylus graph depicting a thickness of 0.55 μm for the single layer CIS. There was no variation in thickness with composition in the present samples and all the samples were nearly 0.55μm thick.

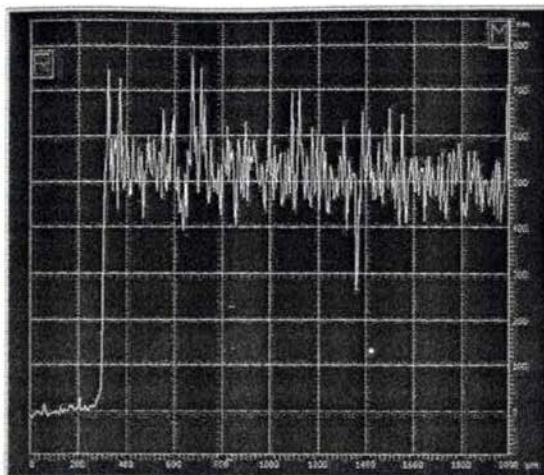


Fig. 4.15: Stylus graph showing single layer thickness of 0.55 μm

Thickness could be increased to 0.85 μm by depositing a second layer of CuInSe_2 , following same steps as for the first layer; this can be further increased by giving a third layer, if necessary. Since CIS possesses a very strong absorption coefficient ($\sim 10^5 \text{ cm}^{-1}$), thickness of about 1 μm is sufficient for absorption of the full intensity of sunlight falling on the specimen as these direct band gap semiconductors operate through field assisted carrier collection (carrier ‘drift’) rather depending on diffusion, as in high purity single-crystal region. It is better to have bi-layer structure for the absorber in photovoltaic devices, as back contact recombination can be reduced by making the bottom layer highly conductive. In the present study, this requirement can be achieved by making the back layer slightly Cu-rich. Increase in Cu concentration enhances the conductivity by forming a p^- layer. This p^- bottom layer can create “Back Surface Field (BSF)” which assists in hole collection and serves as an electron reflector thus reducing the recombination.

4.5.3 EDAX measurements

Deviation in the actual composition from the ideal formula can be described by two parameters, viz., deviation from molecularity (Δm) and the deviation from stoichiometry (Δs). These parameters are defined as,⁴³⁻⁴⁵

$$\Delta m = \frac{Cu}{In} - 1$$

and

$$\Delta s = \frac{2[Se]}{[Cu] + 3[In]} - 1$$

If $\Delta m > 0$ and $\Delta s > 0$ the sample will be p-type and if $\Delta m < 0$ and $\Delta s < 0$, the sample will be n-type.

Atomic concentration of the constituent elements was determined using EDAX, at different points along the entire length of the sample. Samples CIS10 was spatially non-uniform in composition. In CIS10, Cu was found to be agglomerated and hence the composition was different at different points. Average composition is given in table 4.5. Also formation of Cu₂Se phase was identified from the XRD studies, probably due to the increased concentration of Cu. Mass of Cu evaporated was greater for CIS10 than CIS9. But due to the spatial non-uniformity in CIS10, EDAX analysis showed nearly the same composition for both the samples. Typical values are given in table 4.5. With increase in Cu concentration in the solution, the atomic concentration of Cu in the sample (as per the EDAX results) was also increasing.

Cu-rich films should be dominated by antisite (Cu_{In}) acceptor defects, yielding strongly p-type layers. However, in all cases, auto-compensation may be expected at high intrinsic defect levels in order to maintain overall valence neutrality. Cu_{In} antisite defects move a Cu⁺¹ atom onto a nominally In⁺³ site, resulting in a net charge of -2. This can be compensated for by the creation of a Se vacancy (net change in charge of +2) with a resulting decrease in Se concentration as the Cu concentration increases as observed.

Table 4.5: Atomic percentage and deviation from stoichiometry and molecularity of the samples with different Cu concentrations.

Sample name	Atomic concentration in percentage			Δm	Δs	Cu/In ratio
	Cu	In	Se			
CIS7	20.67	23.38	56.05	-0.12	0.23	0.88
CIS8	23.89	21.44	54.67	0.11	0.24	1.11
CIS9	27.25	19.28	53.47	0.41	0.26	1.41
CIS10	27.15	21.71	51.14	0.25	0.55	1.25

4.5.4 Optical absorption

Fig 4.16 shows absorption spectra of samples CIS7 to CIS10, recorded in the wavelength range 500 nm to 1500 nm at room temperature. The band gap increased from 0.95 eV to 0.99 eV with increase in Cu concentration even though the variation was not regular. CIS8 had lowest E_g of 0.95 eV and CIS10 had the highest band gap of 0.99 eV in this set of samples. The crystallinity and grain size were high for CIS8, which caused the band gap to decrease. This increase in band gap for CIS10 can be attributed to the presence of Cu_2Se phase in CIS10. The absorbance was found to be larger for CIS8. Table 4.6 gives the band gap variation in the samples.

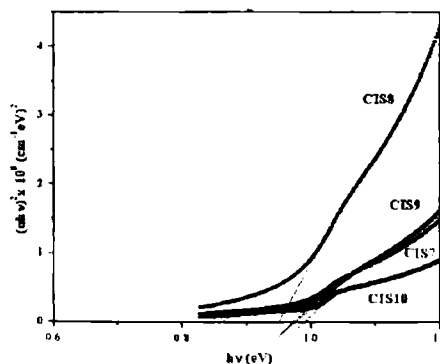


Fig.4.16 Absorption spectra of samples

Table 4.6: Band gap variation

Sample name	Band gap eV
CIS7	0.97
CIS8	0.95
CIS9	0.97
CIS10	0.99

In all the films, there existed a second absorption edge at energies near 1.1 eV as obtained in the earlier case which could be attributed to the valence band splitting.

4.5.5 Electrical characterization

Table 4.7 gives the type of conductivity, photosensitivity and resistivity of the samples. Type of conductivity was determined to be p-type using hot probe method for all the samples, except CIS7. Interestingly, CIS7 was the only In-rich sample in this series. Excess 'In' might have created donor levels like In_i, In_{Cu}, In_{Se} etc in CuInSe₂ which converted the conductivity type to n. For CIS7, the deviation from molecularity was <1 and hence the stoichiometry supported the n-type behaviour. For all other samples, deviation from molecularity and stoichiometry was >1, and hence were showing p-type conductivity.

Table 4.7: Type of conductivity and resistivity for the Cu varied samples

Sample name	Type of carrier	Photosensitivity	Resistivity Ωcm
CIS7	n	-0.78	10.37
CIS8	p	0.17	76
CIS9	p	0.1	3
CIS10	p	-0.045	1.8x10 ⁻³

For the n-type sample, the resistivity was 10.37 Ωcm while resistivity of p-type samples decreased with increase in Cu. Thus highly conductive ($\rho \sim 10^{-3}$ Ωcm) as well as resistive samples ($\rho \sim 76$ Ωcm) could be prepared using this method.

For device fabrication, usually slightly resistive samples (resistivity of the order of 10¹ Ωcm) are preferred, whereas the highly conductive films are used as the bottom layer of the absorber near the electrode. This low resistivity CIS layer incorporated on the contact-side lowers the series resistance R_s of the device. Photosensitivity of the n-type sample was negative and for the remaining samples its value was fractional. For the

highly conductive sample, CIS10, the photosensitivity again showed negative value. The negative photosensitivity may be due to recombination of light generated minority carriers with holes (electrons) at the top of the valence band (bottom of the conduction band).

4.5.6 Morphological analysis

Morphological analysis carried out using AFM is shown in (Fig.4.17 (a)-(d)). The 3 dimensional AFM image showed that in CIS7 (i.e. the n-type sample), the grains were agglomerated. These agglomerations might be due to the unreacted binary phases which were not revealed in XRD analysis. These grains were separated indicating the reason for low conductivity of this sample. There was a distribution of grain size in the films. Grain size varied over a wide range, (from 61 nm to 202 nm).

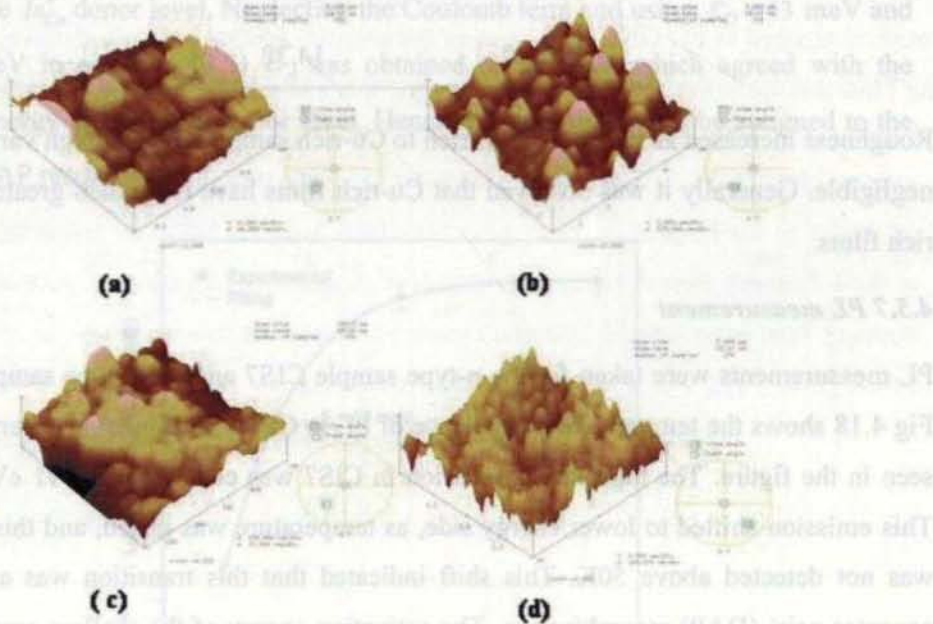


Fig. 4.17 Three dimensional AFM images of samples

(a) CIS7 (b) CIS8 (c) CIS9 (d) CIS10

With the increase in Cu concentration, the geometry of the grain changed from spherical to pyramidal. Pyramidal shape could be clearly seen in the case of CIS10. Here the grains were densely packed and hence this could lead to increase in conductivity as observed in the films. The rms value of surface roughness also increased with increase in Cu concentration and this was calculated from AFM for a sample area of 250nm x 250nm. The roughness values are given in Table 4.8.

Table 4.8: Roughness variation in the samples

Sample name	Roughness in nm
CIS7	7.64
CIS8	11.75
CIS9	16.87
CIS10	14.32

Roughness increased as we go from In-rich to Cu-rich samples even though variation was negligible. Generally it was observed that Cu-rich films have roughness greater than In-rich films.

4.5.7 PL measurement

PL measurements were taken for the n-type sample CIS7 and the p-type sample CIS10. Fig 4.18 shows the temperature dependence of PL in CIS7. The signal was very noisy as seen in the figure. The highest PL emission in CIS7 was centered at 0.991 eV at 12 K. This emission shifted to lower energy side, as temperature was raised, and this emission was not detected above 50K. This shift indicated that this transition was a 'donor – acceptor pair' (DAP) recombination. The activation energy of the shallow center among the DAP was calculated by fitting the plot of log (PL intensity) vs 1000/T as shown in Fig. 4.19 using the equation (3.6).

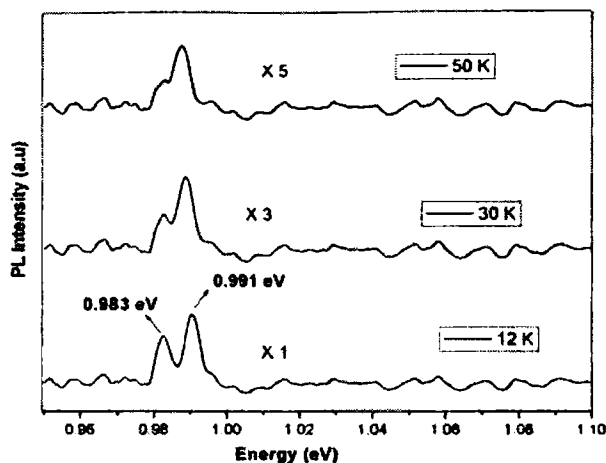


Fig. 4.18: Temperature dependence of PL spectra of sample CIS7 (Cu/In=0.88)

The activation energy was obtained to be 13 meV which agreed with the activation energy of the In_{Cu}^+ donor level. Neglecting the Coulomb term and using $E_D = 13$ meV and $E_g = 1.042$ eV in equation (3.5) E_A was obtained as 38 meV which agreed with the activation energy of the V_{Cu} acceptor level. Hence this emission could be assigned to the $In_{Cu}^+ - V_{Cu}$ DAP recombination.

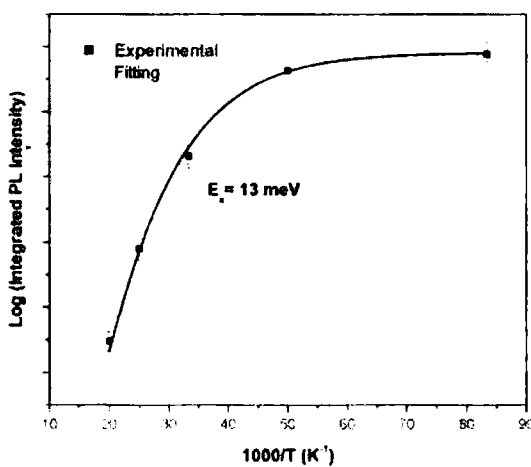


Fig. 4.19: Plot of $1000/T$ vs \log (integrated PL intensity) of CIS7 fitted using equation (4.2)

Fig.4.18 shows a shoulder on the lower energy side centered at 0.983 eV whose position did not change with increase in temperature. But this was quenched, at a much faster rate, compared to the peak due to the DAP transition. Hence this emission could be assigned to the (D^0, h) transition. From our previous work, it was well established that the 0.983 eV line is representing Cu_i -VB transition. For verification, we used equation

$$E_{PL} = E_g - E_D \tag{4.2}$$

(where E_{PL} is the emission energy, E_g the band gap and E_D the donor activation energy) and obtained $E_D = 59$ meV, which is comparable to the activation energy of ionized Cu_i donor level.^{30,31} Figure 4.20(a) reveals the PL spectra of sample CIS10 (Cu/In=1.25), which was Cu-excess in composition. The film stoichiometry indicated that this film was highly Cu-rich. In CIS10, the highest PL peak position was at 1.032 eV and was very weak compared to the other emissions in the sample. Also it was not observed above 12 K. Thus this emission could be assigned to the free exciton (FE) line in this sample.

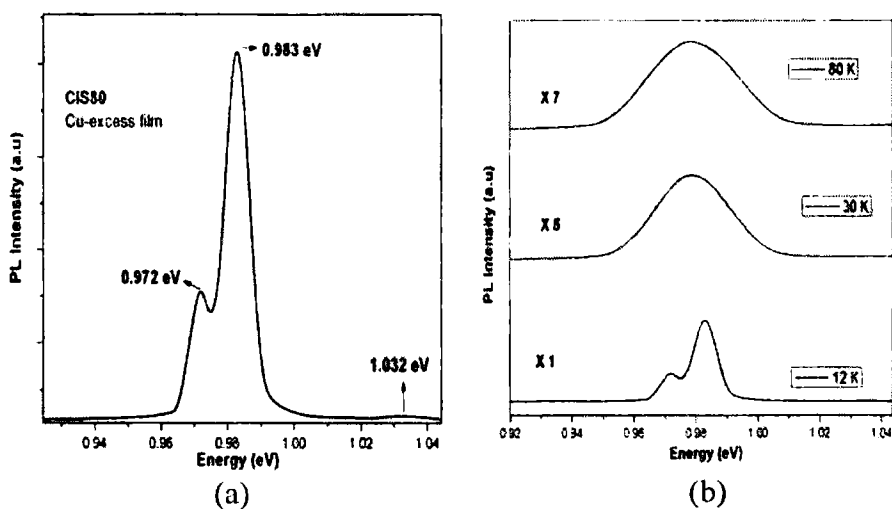


Fig. 4.20:(a) PL emission from sample CIS10(Cu/In=1.25) at 12 K and
(b) Temperature dependence of PL emission in the sample

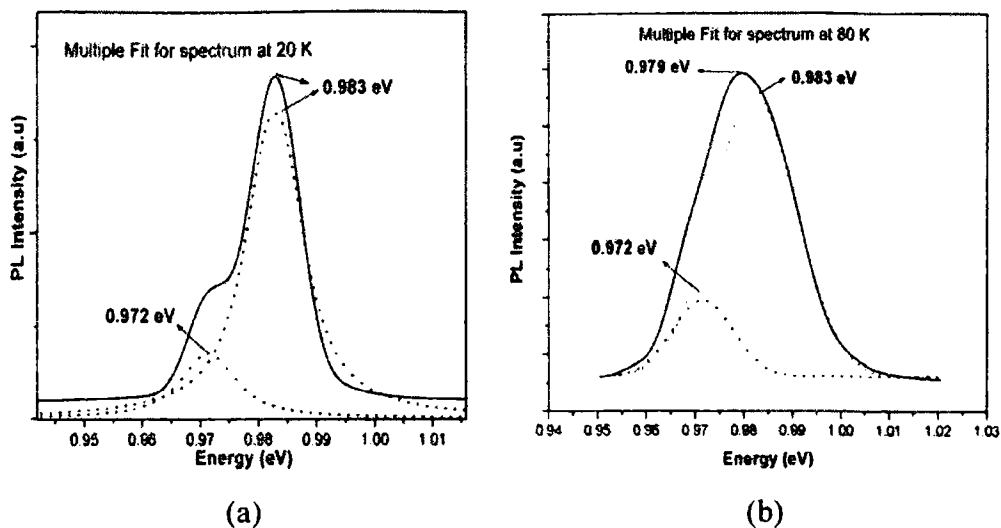


Fig. 4.21: Multiple curve fitting of the PL spectra obtained from sample CIS10 at (a) 20 K and (b) 80 K.

Figure 4.21(a) and (b) depict the temperature dependent PL of this sample. As the temperature increased, the PL spectra broadened, with the peak position shifting to 0.979 eV. Multiple fitting of the spectra at higher temperatures showed that the broad spectra contained emissions at 0.983 eV and 0.972 eV (Fig. 4.21 a & b). Thus it could be concluded that the two emissions merged, resulting in spectral broadening and shift in peak position. In the de-convoluted spectrum, since there was no change in peak position of the emission at 0.983 eV, it was assumed that this was the $Cu_i - VB (D^0, h)$ transition was observed in Cu-rich samples.

Figure 4.22 represents the plot of ratio of the intensities ($Cu_i - VB (D^0, h)$ to 0.972 eV transitions) versus $1000/T$ fitted using the equation

$$\frac{I_{Dh}}{I} = \exp\left(-\frac{\Delta E}{kT}\right) \quad (4.5)$$

where I_{Dh} is the intensity of the (D^0, h) emission while I is the intensity of the 0.972 eV emission. It could be realized that the intensity of the emission at 0.983 eV increased

relative to the emission at 0.972 eV. The activation energy, ΔE , was obtained to be ~ 5 meV, which agreed with the exciton binding energy in CuInSe₂.³²⁻³⁴ Hence it was concluded that the emission at 0.972 eV was the ‘bound exciton emission’ in this sample. Rincon et al had observed emission at 0.973 eV and had assigned it to the transition of exciton bound to the acceptor Cu_{In} (BX2: Cu_{In}).³⁵ Presently it can only be speculated that this may be the same BX2 transition as the film stoichiometry supported the assignment. The absence of this emission line in In-rich samples once again, supports the assignment.

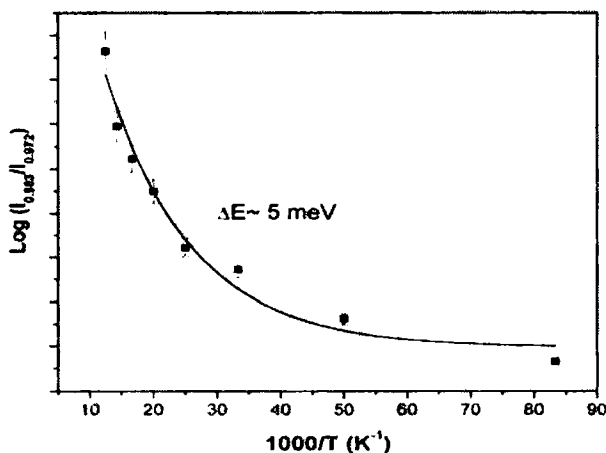


Fig. 4.22: Ratio of the intensities of the emission ($I_{Dh}(0.983 \text{ eV}) : I(0.972 \text{ eV})$) as a function of temperature fitted using equation (4.3)

4.6 Effect of variation of In-concentration

From the above series of samples, CIS7 to CIS10, we could not obtain a sample having reasonable photosensitivity. CIS8 (Cu-50, In-110 and Se-175mg) and CIS9 (Cu-60, In-110 and Se-175mg) were of comparable photosensitivity [0.17 and 0.1 respectively]. CIS9 had low resistivity and hence the Cu concentration was fixed at 60-mg and Se at 170mg; In concentration was varied from 110mg to 130 and 150mg and the samples are named as CIS11, CIS12 and CIS13 respectively.

4.6.1 Structural Characterization

Fig 4.23 shows the X-ray diffraction pattern of the samples in which concentration of In was varied from 110 to 150mg.

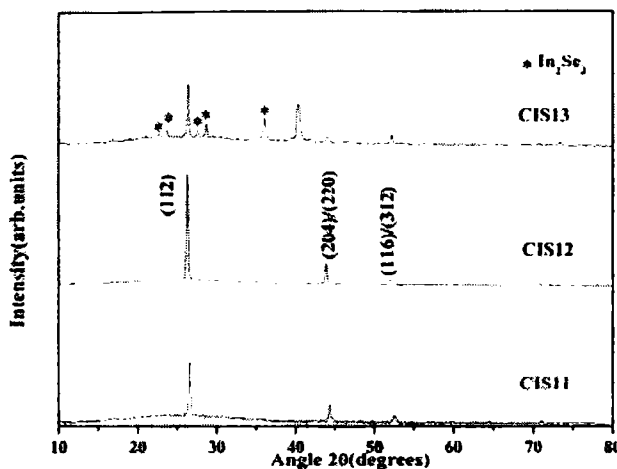


Fig 4.23: X-ray diffraction pattern of In varied samples

Samples CIS11 and CIS12 showed single phase CuInSe_2 , while CIS13 showed In_2Se_3 phase in addition to the CIS phase. All the samples were preferentially oriented along (112) plane. The peak intensity increased drastically for CIS12 in which case, all the three peaks were clearly visible. With further increase in 'In' concentration, secondary phases like In_2Se_3 appeared and the CIS peak intensity decreased with the onset of In_2Se_3 phase. The grain size of these samples, calculated using Debye-Scherrer formula, and the POQ values are given in table 4.9. Even though the sample CIS13 possessed secondary phases, grain size and POQ value were very high for this sample. The peak intensity was greater for CIS12. But the full width at half maximum (FWHM) was lowest for CIS13 and hence the highest grain size.

Table 4.9 Variation in grain size and POQ values

Sample name	POQ	Grain Size nm
CIS11	3	35
CIS12	4	42
CIS13	5	65

4.6.2 EDAX measurements

Table 4.10: Atomic concentration and deviation in molecularity and stoichiometry

Sample name	Atomic concentration in percentage			Δm	Δs
	Cu	In	Se		
CIS 11	27.25	19.28	53.47	0.41	0.26
CIS 12	17.12	31.48	51.39	-0.46	-0.08

Table 4.10 clearly indicates that, CIS11 was Cu-rich and CIS12 was highly In-rich. The table also gives the deviation from molecularity and stoichiometry. For the Cu-rich sample, both these values are positive and for the In-rich sample the values are negative.

4.6.3 Optical Absorption

Absorption spectra were recorded in the range 1500 to 500nm. Fig 4.24 shows the absorption spectrum of the In-varied samples. From the table 4.11, it was found that band gap varied slightly.

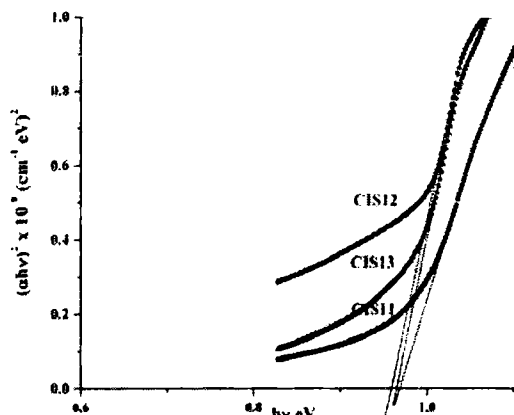


Fig 4.24: Absorption spectra of In varied samples.

Table 4.11: Band gap variation

Sample name	Band gap (eV)
CIS11	0.97
CIS12	0.96
CIS13	0.965

4.6.4 Electrical Characterization

Hot probe analysis proved p-type nature of sample CIS11. This sample was found to be Cu-rich from the EDAX analysis; more over, deviation from molecularity and stoichiometry was >0 in this case. But samples CIS12 and CIS13 were n-type, since In-concentration was high in these samples. CIS12 showed negative values for Δm and Δs . Table 4.12 shows the electrical parameters of samples CIS11-CIS13.

Table 4.12: Type of conductivity and variation in resistivity and photosensitivity of samples

Sample name	Type of conductivity	Resistivity, ρ (Ωcm)	Photosensitivity
CIS11	p	3	0.09
CIS12	n	0.005	-0.60
CIS13	n	1.03K	-0.01

Resistivity was $3\Omega\text{cm}$ for CIS11 and photosensitivity was 0.09. In the case of CIS12, the resistivity decreased and the photosensitivity became negative. In the normal case, there should be an increase in resistivity with increase in 'In' concentration. But in the present case, there occurred a type conversion and the increased 'In' concentration in this sample

gave way to decreased resistivity. With further increase in ‘In’ concentration, [i.e. for CIS13], the resistivity again increased. This increase can be attributed to the presence of binary phase in this sample.

4.6.5 Discussion

‘In’ concentration was varied in the samples. The samples CIS12 and CIS13 were n-type while CIS11 was p-type. Also, on increasing mass of ‘In’ evaporated to 150 mg, there occurred In₂Se₃ phase in addition to the CIS phase. Hence it was concluded that ‘In’ concentration of 110 or below should be used in the present work. However, this n-type layer can be made use of for the fabrication of homojunction solar cells.

4.7 Minute variations of Cu and In concentrations

From the characterizations carried out above, only CIS8 (Se-170, In-110 and Cu-50) exhibited reasonable photosensitivity. Minute variations in Cu and In concentrations were made to achieve better photosensitivity in the samples. However concentration of Se was fixed in all the cases. Samples were prepared with masses In-112mg and Cu-51mg(CIS14), In-110mg and Cu-46mg(CIS15), In-112 and Cu-50(CIS16), In-114 and Cu50mg(CIS17), In-118 and Cu-50mg(CIS18). Table 4.13 shows the photosensitivity and resistivity of these samples.

Table 4.13 Electrical parameters of the samples CIS14 to CIS18

Sample name	Resistivity Ωcm	Photosensitivity	Type of Conductivity
CIS14	0.019	0.02	p
CIS15	0.114	0.02	p
CIS16	0.011	-0.02	p
CIS17	2.6	-0.07	p
CIS18	9.3	0.1	n

From the table, it is clear that the photosensitivity of the p-type samples was very low and conductivity changed to n type, when In-concentration was increased to 118mg.

4.8 Optimization for solar cell fabrication

In order to get ideal samples for device fabrication, further variation in stoichiometry was carried out. Concentration of Se was fixed at 175 mg and that of Indium at 100 mg and mass of Cu was varied from 20 to 50 mg in steps of 10 mg so that Cu/In ratio was 2.37, 1.48, 1.13, and 0.98 respectively, as obtained from EDAX. The samples were named as CIS0.2, CIS0.3, CIS0.4 and CIS0.5. These samples were fully characterized to find the suitability for device fabrication.

4.8.1 Structural Characterization

Structural characterization was performed using X-ray diffraction and Raman analysis.

(i) **XRD:** Fig 4.25 shows the XRD pattern of the samples. Peaks were observed in the (112), (220)/(204) and (116)/(312) planes with preferential orientation along (112) direction as observed earlier. As Cu concentration increased, the crystallinity also increased. Cu-rich films are generally more crystalline than In-rich films. In the case of Cu rich films, there occurs a liquid phase of Cu_xSe which enhances the grain growth. Crystallinity was better for CIS0.4 and decreased with further increase in Cu-concentration. In the case of CIS0.5, for which Cu concentration was the maximum, secondary phase of Cu_3Se_2 was observed. However grain size and POQ value were high for CIS0.4 and the values are listed in the table 4.14

The XRD profile contained only the common peaks corresponding to sphalerite and chalcopyrite structures as obtained earlier. To confirm the structure of the CuInSe_2 films, Raman analysis was carried out on these samples.

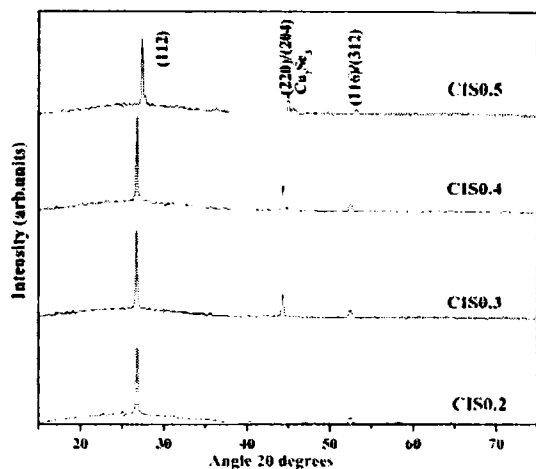


Fig. 4.25: X-ray diffractogram of the samples

Table 4.14: Grain size and POQ values

Sample name	POQ value	Grain size nm
CIS 0.5	3	51
CIS 0.4	4	63
CIS 0.3	4	60
CIS 0.2	3	49

(ii) **Raman analysis:** Raman analysis was performed in the ‘back scattering mode’ at room temperature using micro Raman system [Jobin Yvon Horibra LABRAM-HR] in visible region (400 -1100 nm) with a spectral resolution of 1cm^{-1} . Argon ion laser of wavelength 488nm was used as excitation source. The chalcopyrite structure is a tetragonal body centered lattice and belongs to the space group $I\bar{4}2d$, i.e. to the point group D_{2d}^{12} . On the basis of the character table of the group D_{2d} , the general vibrations for the primitive cell, involving optic and acoustic modes are distributed as,

$$\Gamma_{\sigma} = A_1 + 2A_2 + 3B_1 + 4B_2 + 7E$$

If we take into account that the symmetry of the acoustic modes is $B_2 + E$, then for the optic modes in the crystal,

$$\Gamma_{\text{vib}} = A_1 + 2A_2 + 3B_1 + 3B_2 + 6E$$

Therefore there are 19 Raman active vibrations ($A_1 + 3B_1 + 3B_2 + 6E$), nine infra red active ($3B_2 + 6E$), and two silent modes ($2A_2$).³⁶ The observed modes in CuInSe_2 are listed below in Table 4.15.

Table 4.15: The different vibrational modes observed in CuInSe₂

Frequency(cm ⁻¹)	Approximate relative strength (%)	Assignment
259	15	E
231	8	B ₂ ,E
215	22	B ₂ ,E
206	10	E
174	100	A ₁
124	20	B ₁
76	35	B ₁
61	30	B ₂

Figure 4.26 shows the Raman spectra of the samples. All the samples showed a prominent peak at 174 cm⁻¹, which is the characteristic peak of chalcopyrite structure. This peak corresponds to A₁ mode in which Se atoms vibrate in the x-y plane with Cu and In atoms at rest. Hence frequency of this mode is associated with Se mass and the cations–Se bond stretching forces, describing the interaction between nearest neighbors. The frequency of the A₁ mode is given by

$$\nu = \left(\frac{k}{M_{Se}} \right)^{1/2}$$

where k is the force constant and M_{Se}, mass of Se atom.³⁶ Dependence of ν on these force constants can be expressed as

$$\nu^2(A_1) = \frac{2(\alpha_{Cu-Se} + \alpha_{In-Se})}{M_{Se}}$$

where $\alpha_{\text{Cu-Se}}$ and $\alpha_{\text{In-Se}}$ are the bond-stretching constants between the corresponding atoms.³⁷ Because of the dependence on force constants, position of this mode directly depends on the atoms surrounding Se.

A₁ mode appears even for non-stoichiometric composition, if the chalcopyrite structure is not distorted. Intensity of Raman peak is directly proportional to crystallinity of the sample which can be verified using X-ray Diffractogram. XRD proved that crystallinity was better for CIS0.4 and Raman peak also showed maximum intensity for this sample.

CIS0.2 showed additional modes at 212 cm⁻¹ and 231 cm⁻¹ which were due to the transverse optical (TO) and longitudinal optical (LO) phonon mode with B₂ or E symmetry respectively. B₂ type are excited for light polarized parallel to the optic axis and E type are excited only for light polarized perpendicular to the optic axis. These modes reflect the vibration of In-Se atoms in antiphase. Remaining samples showed weak peaks for these modes, as In and Se concentrations were low compared with CIS0.2.

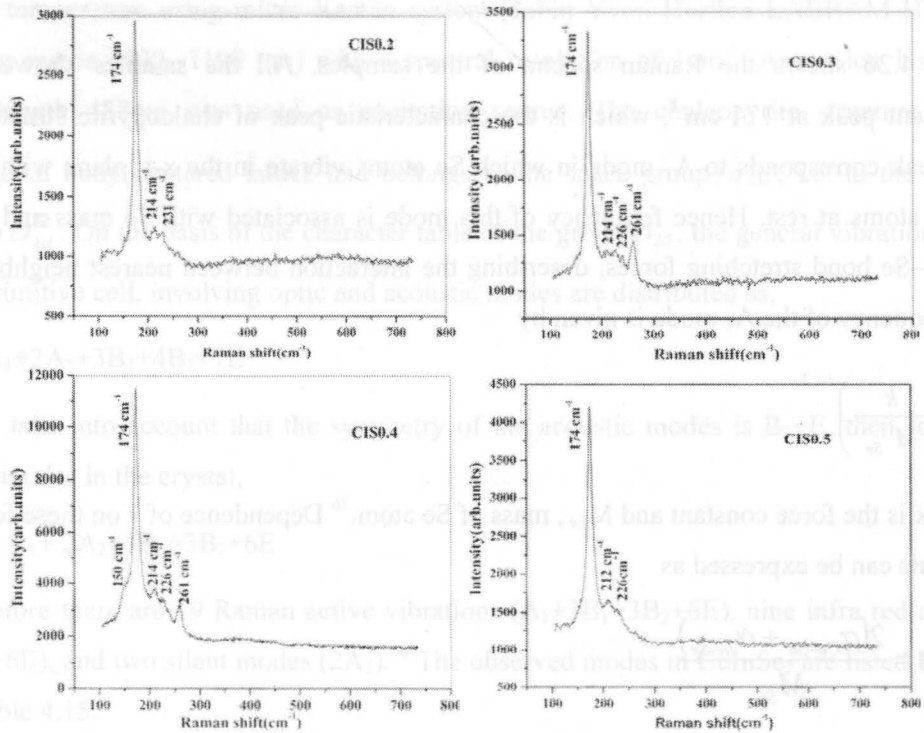


Fig. 4.26: Raman spectra of the samples CIS0.2 to CIS0.5

With the increase in Cu concentration (CIS0.4), B₂ mode showed a slight shift to 226 cm⁻¹ and this may be due to vacancy of Indium or stress in the sample. For CIS0.3 and CIS0.4, an additional mode at 260cm⁻¹ could be seen. This peak is assumed to be the highest frequency mode in CuInSe₂. This mode is reported to be due to Cu_xSe binary phase by many authors.^{38, 39} In the present case, this peak disappeared for the Cu-rich sample CIS0.5 which contained Cu₃Se₂ phase. Hence it was concluded that this peak was not due to any Cu_xSe phase and could be attributed to B₂+E mode. Intensity of the A₁ mode was better for CIS0.4 which also shows that it is the most ordered structure.

Raman spectra of CIS0.4 showed a shoulder at 150 cm⁻¹, which corresponds to the highest frequency B₁ mode. This peak showed a slight decrease from the original value of 160cm⁻¹. This may be due to stress in the sample. The B₁ mode corresponds to the frequency of vibration of Cu and In atoms in antiphase. In this case, the polarizability changes during the vibration due to the stretching of the Cu-In bond are partially compensated by the compression of the In-Se bond and hence this mode is very weak. Frequency of this mode is given by³⁶

$$\nu = \frac{k(M_{Cu} + M_{In})^{1/2}}{(M_{Cu}M_{In})^{1/2}}$$

Mode at 150cm⁻¹ is also reported to be due to In-Se compounds. As the composition was Cu-rich, in the present case, this possibility could be avoided.

From the Raman analysis of the samples, we could confirm that the structure was chalcopyrite which was the most favorable structure for solar cell fabrication. The compositional variation was reflected in the Raman spectrum also. Intensity of the A₁ mode was directly linked with the crystallinity. Hence from the FWHM of the Raman peak, one could have an idea about the crystallinity of the films.

4.8.2 Compositional analysis

(i) EDAX measurements: Elemental concentrations were determined using EDAX and depth-wise analysis of the sample was carried out using XPS measurements. The atomic concentrations in percentage are given in the table 4.16. CIS0.5 has Cu concentration of 32.79% for which Cu₃Se₂ phase was observed. From the table, it is clear that on decreasing Cu concentration, In and Se concentrations increase correspondingly. On reaching CIS0.3, the concentration of In remained almost steady and hence for CIS0.2, Se concentration increase sharply to 60.04%.

Table 4. 16 Atomic concentration and deviation from stoichiometry and molecularity

Sample name	Atomic concentration in percentage			Δm	Δs
	Cu	In	Se		
CIS 0.5	32.79	13.82	53.39	1.37	0.44
CIS 0.4	27.04	18.29	54.67	0.48	0.33
CIS 0.3	22.84	20.19	56.97	0.13	0.37
CIS 0.2	19.75	20.21	60.04	-0.022	0.49

The deviation from molecularity (Δm) and stoichiometry (Δs) of the samples were also listed in the table. CIS0.2 showed a slight negative value for Δm .

(ii) XPS analysis: XPS analyses were performed for the samples CIS0.2 and CIS0.4. Depth-wise XPS analysis was done, employing argon ion sputtering. Figures 4.27-4.28 show the XPS profile of CIS0.2. The shift in the binding energy (BE) of In and Se at the surface layers could clearly be seen. On comparing the binding energies it was observed that In₂Se₃ was formed at the surface. After two layers, the formation of CuInSe₂ was evident from the binding energy shift. In the case of CuInSe₂, binding energies of Cu, In and Se are Se-54.6 eV and In-444.7 eV respectively. From EDAX, the sample was identified as highly Se-rich. This may be the reason for the formation of In₂Se₃. However, from the XRD analysis, we could get only the CuInSe₂ phase.

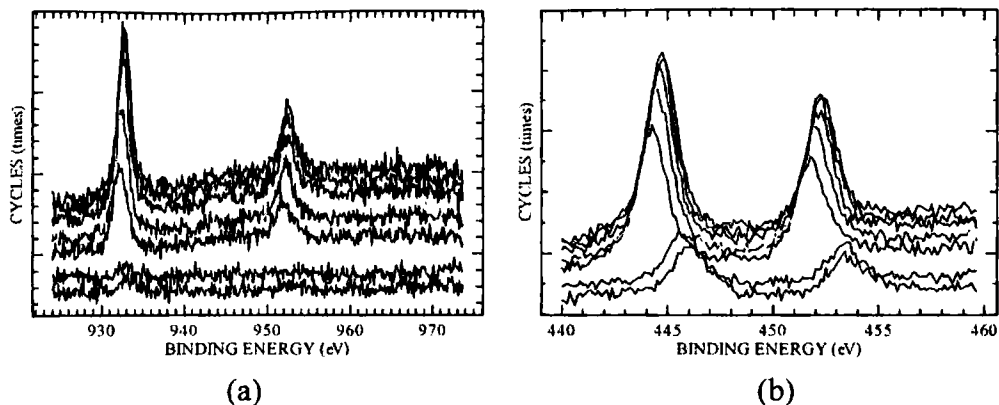


Fig. 4.27: XPS depth profile of (a) Cu in CIS0.2 (b) In in CIS0.2

Figure 4.27(a) shows the depth-wise analysis of Cu concentration. It can be seen that, Cu was absent in the surface layers of the sample. The peak intensity was high after two cycles of etching. Binding energies of 932 and 952.2eV were corresponding to $\text{Cu}2p_{1/2}$ and $\text{Cu}2p_{3/2}$ states in CuInSe_2 respectively.

The depth-wise analysis of In (Fig. 4.27(b)) shows a shift in binding energy for the two layers at the surface. The binding energies of 445.5 and 453.5eV were corresponding to that of In in In_2Se_3 phase. The shift in the first two layers was also observed in the Se depth analysis (Fig 4.28(a)). The binding energy of these layers was 55.5 eV, which was nearly equal to the BE of Se in In_2Se_3 . Hence it was concluded that In_2Se_3 was formed at the surface layers of the sample. Since sample stoichiometry contains 60.04% of Se, the formation of In_2Se_3 is possible.

The inner layers in the 'In' depth profile [with binding energies of 444.7 and 452.1eV] were corresponding to $\text{In}3d_{3/2}$ and $\text{In}3d_{5/2}$ respectively which was the BE of In in CIS. The selenium present in the inner layers was having BE of 54.6eV, which was corresponding to the BE of Se in CIS.¹⁰ Hence it could be concluded that CIS was formed in the interior of the sample. At the surface layers, formation of In_2Se_3 was prominent. Fig 4.28(b) shows the depth-wise analysis of oxygen in the sample. It could be seen that oxygen was

absent in the bulk of the sample. Oxygen occurred as a surface contamination at the top layer of the sample.

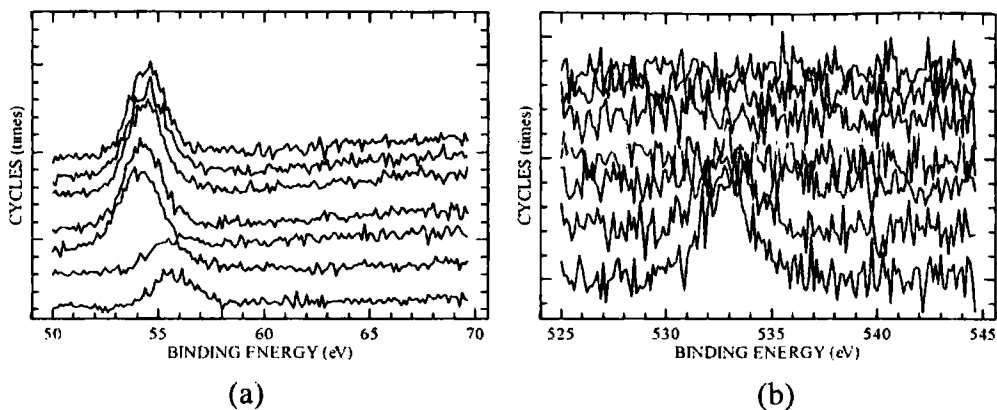


Fig 4.28: XPS depth profile of (a) Se in CIS0.2 (b) of O in CIS0.2

Figs 4.29-4.30 show the XPS depth profile of the sample CIS0.4. The binding energies of Cu, In and Se were corresponding to the BE of these elements in CIS. Hence it may be concluded that single phase CuInSe₂ was formed. No shift in the peak was observed throughout the depth of the sample.

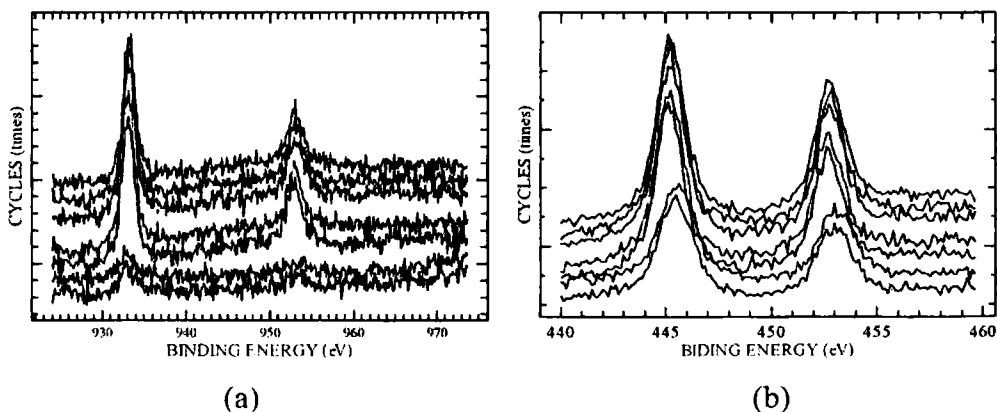


Fig. 4.29: XPS depth profile of (a) Cu and (b) In

The BE of 933eV corresponds to $\text{Cu}2p_{1/2}$ state and 952.6eV corresponds to $\text{Cu}2p_{3/2}$. BEs 445.5 and 452.5eV correspond to $\text{In}3d_{3/2}$ and $\text{In}3d_{5/2}$ respectively. The BE of Se was found to be 54.5eV. All these values correspond to the standard values of these elements in CIS. Fig 4.30(b) shows the depth profile of oxygen. Oxygen was present only at the surface of the sample as the surface contamination.

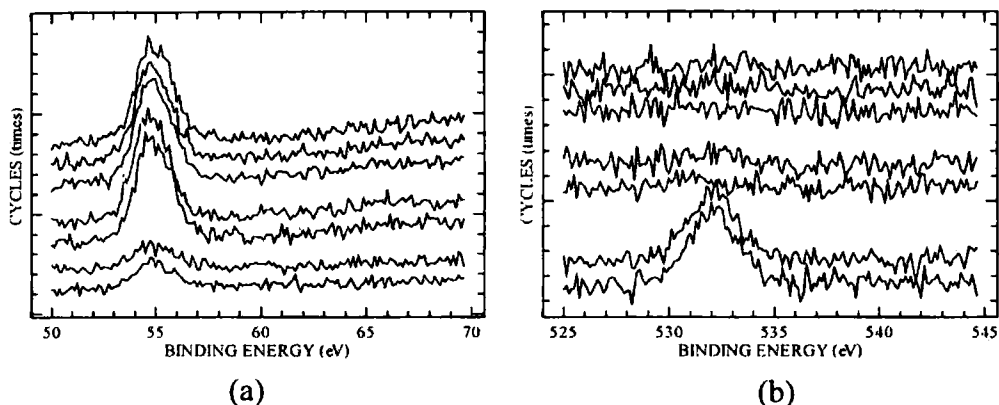


Fig. 4.30: XPS depth profile of (a) Se and (b) O

4.8.3 Optical characterization

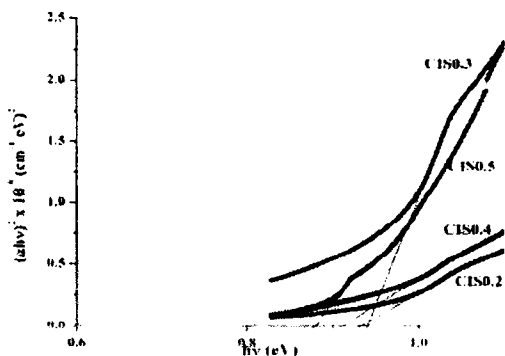


Fig. 4.31: Absorption spectra of the sample

Table 4.17: Band gap

Sample Name	E_g (eV)
CIS0.5	0.94
CIS0.4	0.94
CIS 0.3	0.92
CIS 0.2	0.93

Optical absorption of the sample CIS0.2-CIS 0.5 was measured in the range from 500nm to 1500nm. [Fig 4.31]. There was no significant variation in the band gap of the samples. However, there was a visible change in the value of the absorbance of these samples. CIS0.3 showed higher absorbance and CIS0.2, the least. The E_g values are listed in table 4.17

4.8.4 Electrical characterization

All the samples showed p-type conductivity. Even though there was deviation from molecularity [$\Delta m < 0$] for CIS0.2, the sample showed p-type conductivity. This may be due to the increased Se concentration. Resistivity and photosensitivity were high for CIS0.2. The photosensitivity of the sample gradually changed from positive to negative on increasing the Cu concentration. The high resistivity for CIS0.2 may be due to the presence of In₂Se₃ phase as observed in XPS analysis.

Table 4.18: Resistivity and photosensitivity variation in the samples

Sample name	ρ (Ωcm)	Photosensitivity
CIS 0.5	3.2×10^{-3}	Negative
CIS 0.4	5×10^{-2}	Negative
CIS 0.3	8×10^{-2}	0.001
CIS 0.2	8×10^2	4

For device fabrication, both high and low resistivity CIS are needed as Copper cones will be formed at the junction, when low resistivity CIS is used throughout. This will provide shunting paths. destroying junction properties.

4.8.5 Discussion

Highly resistive and highly conductive CuInSe_2 samples could be prepared using the technique developed in the present work. CIS0.2 was the most photosensitive sample. However, this sample contained secondary phase of In_2Se_3 which made it unsuitable for solar cell fabrication. CIS0.3 can be used as the conductive bottom layer of the solar cell because of its low resistivity. For device fabrication, a slightly resistive layer should be used at the junction. To find this Se concentration was varied slightly.

4.9 Variation of Se concentration

Concentration of Se was varied slightly, keeping the concentrations of Cu and In fixed at 20 and 100 mg respectively. 165 and 185 mg of Se were evaporated for further optimization. These samples were named as CIS165, CIS175 and CIS185 with masses of Se as 165, 175 and 185 mg respectively.

4.9.1 Structural Characterization

XRD analysis of CIS165, CIS175 and CIS185 proved the existence of single phase CIS preferentially oriented along (112) plane [Fig.4.32]. (220)/(204) and (312)/(116) planes were also identified from XRD, as in the earlier case.

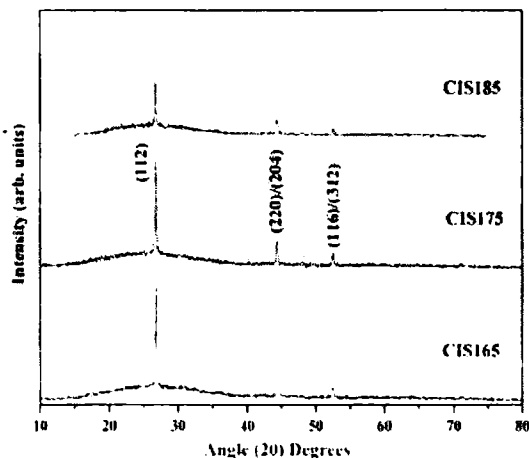


Fig. 4.32: X-ray diffractogram of the Se varied samples

Among these, crystallinity was high for Se concentration of 165mg and it decreased sharply for CIS 185. The grain sizes together with the quality factors are given in the Table 4.19. Maximum grain size and POQ were obtained for Se concentration of 165mg and it decreases with increase in Se concentration.

Table 4.19 Grain size and POQ variation

Sample name	POQ	Grain size (nm)
CIS165	4.6	54
CIS175	4.5	51
CIS185	3.8	45

4.9.2 EDAX measurements

Atomic concentration was determined using EDAX analysis. Table 4.20 gives the atomic concentration and deviation from molecularity and stoichiometry. CIS165 was In-rich, which had a suitable value for device fabrication. In CuInSe₂ based solar cells, the layer used near the junction has In concentration ~26%. Hence the layer of CIS165 can be used in solar cells. With the increase in mass of Se, the atomic percentage was also found to increase. For CIS175, the Se concentration reached 60.04%.

Table 4.20 Atomic concentration and deviation from molecularity and stoichiometry

Sample name	Atomic concentration in percentage			Δm	Δs
	Cu	In	Se		
CIS165	21.55	26.21	52.24	-0.18	0.043
CIS175	19.75	20.21	60.04	-0.022	0.5
CIS185	18.62	27.13	54.25	-0.34	0.085

On increasing Se concentration to 185mg, the EDAX results did not show the same trend. A reduction in Se concentration was observed in this case. Re-evaporation of Se may be

the reason for this reduced Se concentration. In all the cases, deviation from molecularity showed a negative value, since Cu concentration was less than the In concentration in these samples. Still, Δs was greater than zero for all the samples.

4.9.3 Optical characterization

The band gap of the film showed a slight variation with change in Se concentration. The band gap was found to be least for the Se-rich sample (0.93eV). [Table 4.21]

Table 4.21: Band gap variation with Se concentration

Sample name	Band gap eV
CIS165	0.95
CIS175	0.93
CIS185	0.95

The rest of the two samples showed same band gap of ~ 0.95 eV. In CIS165 and CIS185, In concentration was also high, which leads to the increase in band gap of the films. Figure 4.33 and Fig. 4.34 shows the absorption spectra of the Se varied samples. The absorbance was high for CIS185.

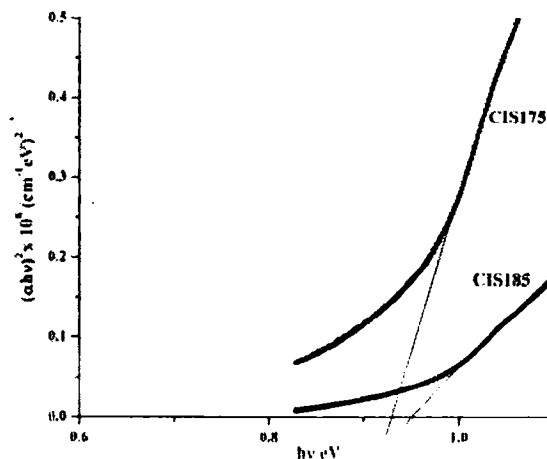


Fig. 4.33 Absorption spectra of CIS175 and CIS185

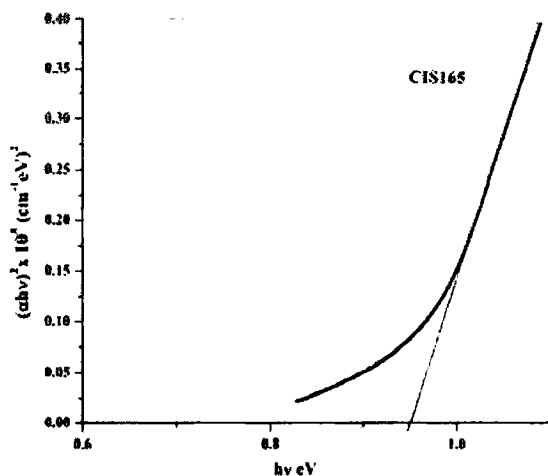


Fig. 4.34 Absorption spectra of CIS165

4.9.4 Electrical characterization

Hot probe measurement proved that all the samples were p-type. Electrical resistivity and photosensitivity are depicted in Table 4.22. With increase in Se concentration, the resistivity shows a decrease. Increase in Se will increase acceptor concentration making the conductivity also high. The photosensitivity increased to 7.7, on decreasing the Se concentration.

Table 4.22 Resistivity and photosensitivity variation in the samples

Sample name	Resistivity ρ (Ωcm)	Photosensitivity
CIS165	7916	7.7
CIS175	800	3.7
CIS185	720	2.8

From the above analysis, it could be concluded that CIS165 possessed suitable resistivity and photosensitivity for device fabrication and hence this layer could be used near the junction. The sample CIS165 was prepared repeatedly to ensure consistency in the properties.

4.10 Stoichiometric CuInSe₂ films

One of the advantages of this deposition technique was that highly stoichiometric films could be prepared without using ultra high vacuum. We could obtain typical concentrations as Cu: 24.92%, In: 24.98% and Se 50.10%. For this, the quantity of elements taken was Cu-25mg, In-105mg and Se-175mg respectively. XRD pattern (Fig. 4.35) shows the highly crystalline nature of this sample with grain size of 44 nm and POQ of 2.6.

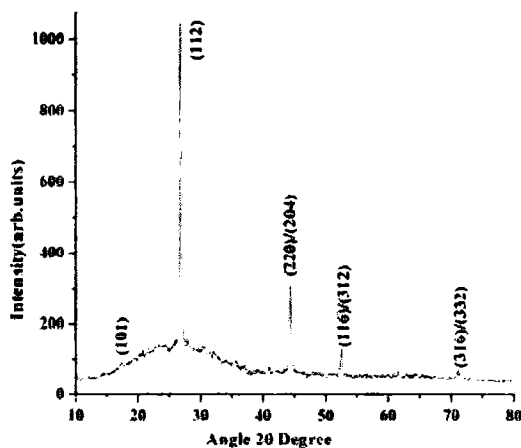


Fig. 4.35: X-ray diffraction pattern of stoichiometric sample

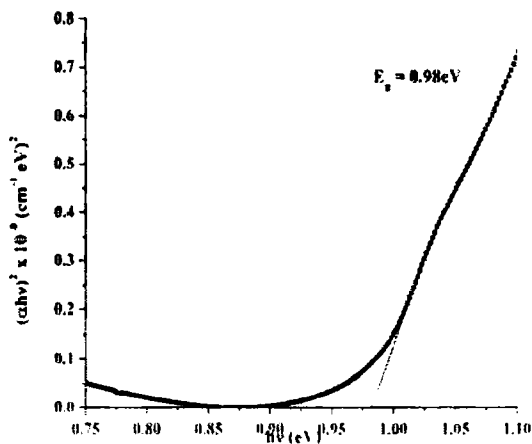


Fig. 4.36: Absorption spectra of stoichiometric sample

Band gap (Fig 4.36) of this ideal sample was 0.98 eV and thickness was 0.58 μm . The sample was p-type in nature and had a resistivity of 2 Ωcm . The sample exhibited very poor photosensitivity of 0.024, probably due to low resistivity of the sample.

PL spectra of this sample (Fig. 4.37(a)) showed very sharp emission, centered at 0.97 eV at very low temperature ($\sim 12\text{K}$). The intensity decreased with the increase in temperature and completely quenched above 90 K. This emission had a high energy shoulder at 0.976 eV. The FWHM of the emission at 0.971 eV [~ 2 meV] was the smallest among the samples studied in this work. The emission at 0.971 eV shifted to higher energy, as the temperature was increased, at the rate of 1.1×10^{-5} eV/K which was much smaller than the shift of 4×10^{-5} eV/K expected for a (e, A^0) free-to-bound transition. Hence this was classified as a 'bound exciton emission'.

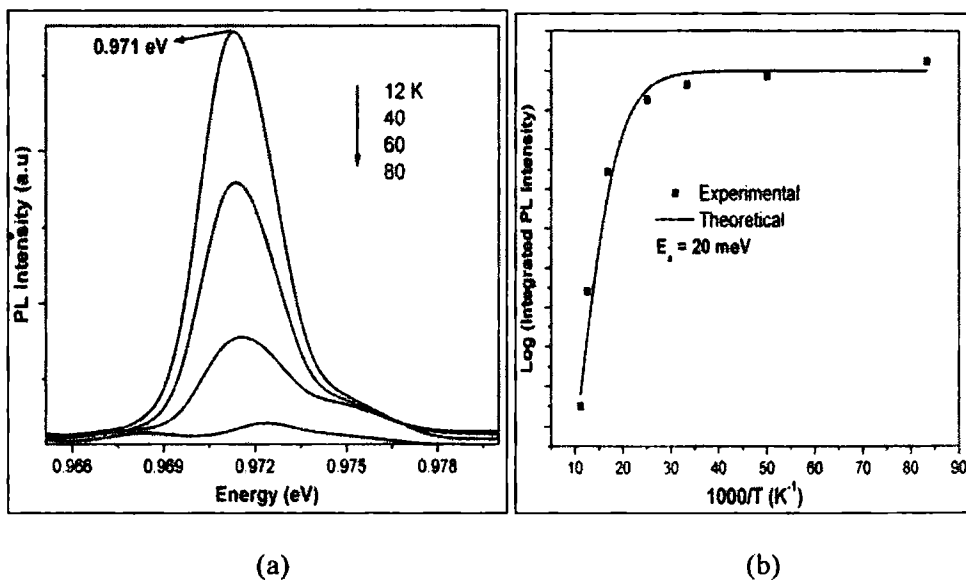


Fig. 4.37: (a) Variation of PL intensity with temperature and (b) Plot of $1000/T$ vs \log (Integrated PL intensity) fitted using equation (4.2)

When excitons are near the defects, the defects can either increase or decrease the binding energy of the exciton. When the defects reduce the total system energy of the exciton, excitons will be trapped in the defects, which lead to the formation of 'bound

excitons'. This gives rise to PL emission at lower energy than that of free excitons. This could be the reason to the absence of FE line was not observed in this sample. Bound exciton emission lines exhibit narrower line-widths than free exciton emissions due to increased localization. This supported our observation as to why the emission at 0.971 eV exhibited very low FWHM. Since most semiconducting materials contain significant amount of impurities and/or defects which can trap excitons, the identification of the bound exciton states provides an important characterization of impurities, which control the electro-optic properties of semiconductors. Neutral and ionized donors and acceptors can trap excitons and form bound excitons.

The bound exciton emission from the sample was quenched above 80 K. In order to calculate the PL quenching energy, a plot between logarithmic value of integrated PL intensity versus $1000/T$ was fitted (Fig. 4.37(b)) using the equation (4.2). The activation energy (ΔE) of the impurity was obtained to be 20 meV. This was in good agreement with the reported activation energy of the doubly ionized In_{Cu}^{++} donor level.^{42, 43} As temperature was raised, the localization decreased due to the thermal ionization of the defect center. This caused the bound exciton to become free, resulting in increase of FWHM and PL peak energy. Thus it could be concluded that this was the In_{Cu}^{++} donor bound exciton (BX:D2 (In_{Cu})) emission in this sample.

4.11 Double layer CuInSe₂

As the thickness of single layer was nearly 0.55 μm , a double layer CIS was prepared for cell fabrication. For this, a highly conductive bottom layer and highly resistive top layer were selected. From the above optimizations, CIS 0.3 with a resistivity of 0.08 Ωcm was ideal for the bottom layer and CIS165 with a resistivity of 7916 Ωcm was ideal as the top layer. The thickness of this double layer was 0.9 μm . X-ray diffractogram (Fig. 4.38) proved the existence of single phase CuInSe₂. Grain size was calculated to be 52 nm.

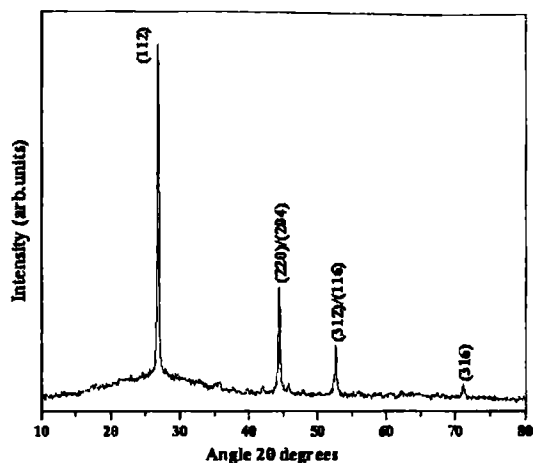


Fig. 4.38: X-ray diffractogram of double layer

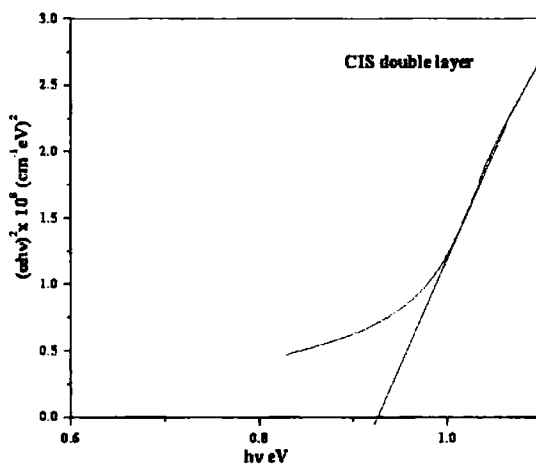


Fig. 4.39: Absorption spectra of CIS double layer

Fig 4.39 shows the absorption spectrum of the sample recorded in the wavelength range 500-1500nm. Band gap of this double layer was 0.93eV. The absorbance of this sample was greater as the thickness was also greater.

Figure 4.40 shows the cross-sectional image of double layer CuInSe_2 . The two layers were clearly distinguishable from the SEM image.

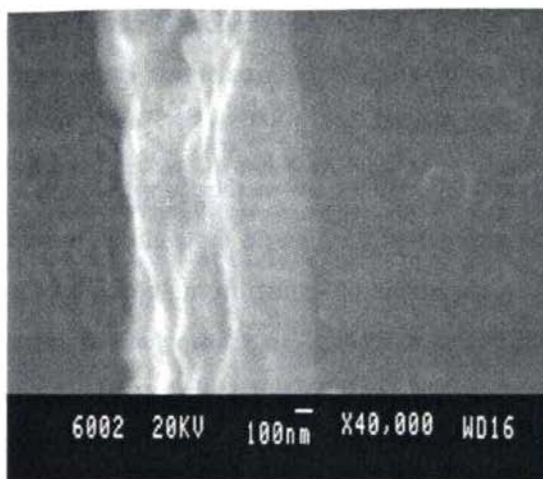


Fig 4.40 Cross-sectional SEM of the double layer

The double layer thickness was also verified using the SEM image and was in agreement to that obtained using stylus measurements.

4.12 Conclusions

CuInSe₂ thin films were prepared using sequential elemental evaporation at moderately low substrate temperature. Indium, Selenium and Copper were evaporated at a substrate temperature of 100°C, 50°C and room temperature respectively. Annealing this stacked layer at 400 °C resulted in the formation of CuInSe₂. Single layer thickness was 0.55 μm which could be increased up to 0.9 μm through double layer deposition, adopting similar steps. This technique was selected for further deposition.

The composition was widely varied to find the suitability in device fabrication. For this Cu and Se were varied, one at a time, keeping the others constant. Both p- and n-type films could be prepared using this technique. From the structural characterizations using XRD and Raman scattering, the structure of CuInSe₂ prepared using the present method, was identified as chalcopyrite which was the most suitable and favorable structure for solar cells. The grain size varied from 35 nm to 63 nm in these samples. However this grain size was still lower than the reported values, obtained through other techniques of CuInSe₂ fabrication. This lead to increase in the number of grain boundaries which, in

some cases, has beneficial effects on CuInSe₂ devices. Interestingly, the grain size of the samples prepared using this technique was three times larger than that prepared using CBD Se (as described in chapter 4).

The band gap varied from 0.93 to 0.99 eV in the samples with variation in elemental concentrations. The AFM analysis of the sample showed that the geometry of the sample changed from spherical to triangular on going from In-rich to Cu-rich. The resistivity varied in the range of 0.002 Ωcm to 7916 Ωcm, from which highly conductive and highly resistive samples could be selected for the device fabrication. The sample with resistivity of 0.08 Ωcm can be used as the conductive bottom layer and sample with a resistivity of 7916 Ωcm can be used as the resistive top layer for device fabrication. The photosensitivity of the highly resistive sample was 7.7. Highly stoichiometric film could be prepared without using ultra high vacuum which is still a major challenge for many researchers working in ternary chalcopyrites. Typical concentration of the stoichiometric sample is Cu: 24.92%, In: 24.98% and Se 50.10%. Hence this technique was proved to be useful for the fabrication of solar cells.

References

1. Markus Gloeckler and J.R.Sites, *J.Appl.Phys.***98** (2005) 103703
2. M.L.Chenene, V.Alberts, *J.Phys.D:Appl.Phys.***36**(2003)56
3. S.M. Firoz Hasan, M.A. Subhan, Kh.M. Mannan, *Optical Materials* **14** (2000) 329
4. A.H.Moharram, M.M.Hafiz, A.Salem, *Appl.Surf.Sci.***172**(2001) 61
5. Doo Youl Lee, Byung Tae Ahn, Kyung Hoon Yoon, Jin Soo Song, *Sol. Energy Mater. Sol. Cells* **75** (2003) 73
6. Yoshio Hachiuma, Atsushi Ashida, nobuyuki Yamamoto, Taichiro Ito, Yoshio Cho, *Sol. Energy Mater. Sol. Cells* **35**(1994) 247
7. NREL, S Baldwin, Office of Energy Efficiency & Renewable Energy , U.S. DOE, June2, 2005
8. X-ray methods, Clive Whiston, John Wiley and sons, New york, 1987
9. V.Alberts, S.Zweigaet and H.W.Schock, *Semicond.Scie. and Tech.* **12** (1997) 217
10. C.Guillen, J.Herrero, *Sol. Energy Mater. Sol. Cells* **73** (2002) 141
11. F. Paraguay D., J.Morales, W. Estrada L., E. Andrade, M. Miki-Yoshida
12. F.Moulder, W.F.Stickle, P.E.Sobol and K.D. Bomben: *Handbook of X-ray Photoelectron Spectroscopy*, Perkin-ElmerCo., Eden Praire, MN, 1992
13. S.M. Firoz Hasan, L. Quadir, Kh.S. Begum, M.A. Subhan,Kh.M. Mannan, *Sol. Energy Mater. Sol. Cells* **58** (1999) 349
14. J E Rowe, J L Shay, *Phys.Rev.B* **3**(2) (1971)
15. J Noolandi, *Physical Review B* **10**(6) (1974)
16. J E Jaffe, Alex Zunger, *Physical Review B* **29**(4) (1983)
17. S Chichibu, T Murakami, T Shioda, T Kurafuji, H Nakanishi, S Niki, P J Fons, A Yamada, *J. Appl. Phys.* **83** (7) (1998)
18. J. Schmidt, H. H. Roscher, R. Labusch, *Thin Solid Films* **251** (1994) 116
19. C.Rincon, R.Marquez, *Journal of Physics and Chemistry of Solids* **60** (1999) 1865
20. S.M.Wasim, *Solar Cells* **16** (1986) 289
21. David.J.Schroeder, Gene.D.Berry and Angus A.Rockett, *Appl.Phys.Lett.* **69**(26) (1996) 4068
22. P. M. Varghese, D. R. Clarke, *J. Mater. Res.* **14**(3) (1999) 1039
23. J.Muller, J.Nowoczin, H. Schmitt, *Thin Solid Films* **496** (2006)364

24. C.-S Jiang, R.noufi, K.Ramanathan, J.a.AbuShama, H.R.Moutinho and M.M.Al-Jassim, *Appl.Phys.Lett* **85**(13) (2004) 2625
25. Yanfa Yan, R.Noufi and M.M.Al Jasim, *Phys. Rev. Ltr.***96** (2006) 205501
26. Doron Azulay, Oded Millo, Isaac Balberg, Hans-Werner Schock,Iris Visoly-Fisher, David Cahen, *Sol. Energy Mater. Sol. Cells* **91** (2007) 85
27. A Rckett, R W Birkmire, *J. Appl. Phys.* **70**(7) (1991) R81
28. H Neumann, *Solar Cells*, **16**(1986) 317
29. J A Groenink, P H Janse, *Z.Phys.Chem.***110**(1978)17
30. J.Muller, J.Nowoczin, H. Schmitt, *Thin Solid Films* **496** (2006)364
31. Schön, J.H. Alberts, V. and Bucher, E. *J. Appl. Phys.* **81**(6) (1997) 2799
32. Ph D Thesis, R Jayakrishnan. Cochin University of Science and Technology, 2008
33. Schön, J. H.; Bucher, E. *Appl. Phys. Lett.*, **73**(2) (1998) 211
34. S. Niki, H. Shibata, P. J. Fons, A. Yamada, A. Obara, and Y. Makita, T. Kurafuji, S. Chichibu, and H. Nakanishi *Appl. Phys. Lett.* **67** (1995) 289
35. Zott, S. Leo, K. Ruckh, M. and Schock, H.-W. *Proceedings of the 25th PVSC*, (Washington, D.C. 1996), p.817
36. Rincón, C., Arsene, M. A., Wasim, S. M., Voillot, F., Peyrade, J. P., Bocaranda, P. and Albacete, A., *Mater. Lett.* **29** (1996) 87
37. C. Rincon, F. J. Ramirez, *J. Appl. Phys.*, **72**(9) (1992) 4321
38. C. Rincon, S.M.Waso, G.Martin, J.R.Huntzinger, A.Zwick, J.Galibert, *J. Appl. Phys.***85**(7) (1998) 3925
39. E.P. Zaretskaya, V.F. Greinenok, V.Riede, W.Schmitz, K.Bente, V.B.Zaleski, O.V.Ermakov, *J.Phys and Chem of solids* **64**(2003) 1989
40. Shigetaka Nomura, Kazuhiko Nishiyama, Kenji Tanaka, Motoya Sakakibara, Masatoshi Oshtsubo, Nobuyuki Furutani and Saburo Endo, *Jpn.J.Appl.Phys.***37**(1998) 3232
41. F.Moulder, W.F.Stickle, P.E.Sobol and K.D. Bomben: *Handbook of X-ray Photoelectron Spectroscopy*, Perkin-ElmerCo., Eden Praire, MN, (1992)
42. R Jayakrishnan. K G Deepa. C. Sudha Kartha., and K P Vijayakumar., *J.Appl.Phys.***100** (2006) 046104
43. C. Rincon, R Marquez, *Journal of Physics and Chemistry of Solids*, **60**(1999) 1865

5.1 Introduction

CuInSe_2 (CIS) based solar cells have now entered into production field with a module efficiency of 16.6% on 16cm^2 mini-modules¹ and 13% on $60\times 120\text{cm}^2$ modules.² The CIGS/CdS solar cell has demonstrated the highest efficiency [of 19.9%] among thin film solar cells (NREL, USA). The first commercial CIGS modules were available in 1998. Nowadays CIS solar cells on flexible substrates are also commercially available and this increases its suitability for space applications. The efforts are going on to produce CIGS solar cells on substrates like stainless steel, polyimide etc. The conversion efficiency has reached 15.2% for CIGS solar cell on light weight metal foil.³ CdS is known as the best counterpart of the CIS layer. As this material is highly toxic, work is going on for the last decade to replace CdS with some other non-toxic compounds.

As CIS based solar cells have now entered into the production phase, the next goal is to reduce the cost and processing time. On comparison with Silicon, the cost reduces from \$2.00/Wp to \$0.50/Wp for CIGS cell. The cells on the flexible substrates costs \$3.50/Wp for Silicon, while it is \$1.00/Wp for CIGS cell. Major CIGS module producers include Shell Solar, Wurth Solar and Global Solar.

5.2 Review of research work on CIS based solar cells

CIS was synthesized for the first time by Hahn in 1953, and its photovoltaic effect was disclosed in 1974 with a conversion efficiency of 12% for single crystal. In 1976,

Kazmerski et al. reported 5.7% efficient polycrystalline CIS/CdS junction.⁴ Tell and Bridenbaugh of Bell Telephone laboratories, studied the photovoltaic properties and junction formation between p and n-CIS (n-type conversion through annealing in Zn or Cd pressures).⁵ Russel et al. studied the Mo/CIS interface and identified the existence of a Schottky barrier at the interface.⁶ During 1983-84, Boeing Corp. reported efficiencies in excess of 10% for thin polycrystalline films obtained from 'three source co-evaporation' process. M.Eron and A.Rothwar presented a model for heterojunction solar cells in which interface recombination was detailed.⁷ EBIC measurement was conducted on CIS/Cd(ZnS) solar cells by R.K.Ahrenkiel and R.J.Matson.⁸ In 1985, Poola Raja Ram et al. fabricated 3% efficient all sprayed CIS/Cd(Zn)S solar cell.⁹ Rommel Noufi and John Dick performed compositional and electrical analysis of the multilayers of CIS/CdS solar cell, demonstrating a P-S-N configuration of the cell, where S stands for semi-insulating CIS layer.¹⁰ R Herms et al. analysed the capacitance of CIS/CdS heterojunctions.¹¹

In 1986, R.E.Hollingsworth and J.R.Sites studied the effect of annealing temperature on CIS/CdS and found that the cell efficiency improved by annealing up to 500K and degraded after that.¹² The role of oxygen in CIS thin films and CdS/CIS devices was the topic of study for R.Noufi et al. The oxygen incorporated into the CIS films increased the acceptor concentration.¹³ R.J.Matson et al. analyzed the CIS/CdS junction activity using EBIC and the role of oxygen in these devices.¹⁴ Allen Rothwarf performed solar cell modeling and analysis on CIS/Cd(ZnS) solar cells.¹⁵ R.W.Birkmire et al. fabricated CIS/CdS heterojunction with efficiencies ranging from 7 to 11.5% and studied the effects of air annealing and CdS thickness on the device performance¹⁶. J.D.Meakin et al. fabricated tandem solar cells based on CIS.¹⁷ J.M.Stewart analyzed health and safety problems in the production of CIS/Cd(Zn)S solar cells.¹⁸

In 1987, "Arco Solar" (now shell solar) achieved a long-standing record efficiency of 14.1% for CIS/CdS solar cell. David Cahen and Rommel Noufi (1989) explained the improvement in the CIS/CdS device performance on air annealing by introducing the role of defects.¹⁹ In 1989, N.Christoforou et al., studied the deep levels in 9% efficient CIS/CdS with the help of DLTS measurement on CIS/CdS solar cells and electron and

hole traps were identified.²⁰ Brian J Brown studied the effect of substrate temperature on the morphology of CIS thin films prepared using chemical spray pyrolysis.²¹ W.N.Shaferman et al.(1991) worked on the CIS/(CdZn)S solar cells for increasing the open circuit voltage of the cell²² while Ji-Beom Yoo et al. (1991) analyzed the effect of a thin intermediate Zinc Selenide layer on the properties of CIS solar cells.²³ Lars Stolt et al. (1992) reported the ZnO/CdS/CIS solar cell with improved performance. An active area efficiency of 14.8% was obtained in this work.²⁴ J.S.Chen et al.(1992) determined the microstructure of CIS/Cd(Zn)S heterojunction solar cells.²⁵ D.Schimdt et al. analysed in detail, the chalcopyrite/defect chalcopyrite heterojunction on the basis of CIS. This model predicted a p-n junction formed between CIS and ‘Ordered Vacancy chalcopyrite’ Compound (1993).²⁶ M.Nishitani et al. fabricated a homojunction CIS solar cell by nitrogen implantation(1993). n-type CIS was prepared for this work and the surface of this layer was converted to p-type by nitrogen implantation. Efficiency of 0.35% was obtained in this work .²⁷

Chung Yang et al. reported the effect of Cu-Mo contacts to CIS and devices using this $\text{Cu}_{0.3}\text{Mo}_{0.7}$ back contacts showed improved performance (1994).²⁸ Gabor et al., (1994), fabricated a 15.9% efficient CIGS solar cell made from $(\text{In}_x\text{Ga}_{1-x})_2\text{Se}_3$ precursor films. The precursors were then converted to CIGS by exposure to Cu and Se flux. The films had a grading of Ga content along the depth which helped in carrier transport, outside the depletion region.²⁹ G.E.Hassan et al. in 1994, analyzed the performance of CIS/CdS solar cells fabricated with sandwich structure. Great improvements were achieved after the device was subjected to a short heat treatment in an environment with a small quantity of oxygen. Conversion efficiency up to 5.2% was obtained.³⁰ M.Nishitani et al., (1994) fabricated substrate type CIS/CdS, CIS/ZnO and CIGS/CdS solar cells with 10.5%, 6% and 11.7% respectively.³¹ Tokio Nakada et al. (1994) prepared CIS based solar cells in which selenization was achieved using Se-vapor from Se containing precursors. Addition of Ga into CIS resulted in an efficiency of 12.6% for CIGS/CdS cell.³² W.N.Shafarman et al. (1996) characterized CIGS solar cells with increasing band gap. With a band gap of 1.3eV, V_{oc} increased to 788mV. ³³A.M.Fernandez et al. reported (1996) an 8% efficient

CIS/CdS solar cell formed from an electrodeposited precursor film. The electrodeposited films were selenized at 550°C.³⁴ Bulent M Basol fabricated CIS/CdS solar cells on flexible substrate for the first time. Substrate was polyimide sheet and the CIS was deposited using selenization of evaporated Cu-In alloy using H₂Se vapor. An active area efficiency of 9.3% was obtained for this cell³⁵

Katsumi Kushiya et al. (1997) fabricated a graded band gap CIGS thin film modules with a Zn(O,S,OH)_x buffer layer. A thin Cu(In,Ga)(SeS)₂ layer was formed at the CIGS surface. The module demonstrated an efficiency of 14.2% for the first time for this absorber –buffer combination.³⁶ S.N.Qui et al.(1997), fabricated CIS/CdS solar cells having an efficiency of 6.3%.³⁷ V.Alberts(1997) et al., analyzed the device characteristics of In-rich solar cells. Film with Cu/In ratio 0.5 was selected for device fabrication and conversion efficiency of 1.2% was obtained for this cell.³⁸ M. Topic et al (1997) examined the blocking current-voltage behaviour through defect chalcopyrite layer in CdS/CIGS solar cell. Acceptor-like defect states, either in a defect-chalcopyrite layer or at the CdS/defect-chalcopyrite interface, caused different trapping under red light or white light.³⁹ T.Nakada(1997) et al reported the improvements in CIGS solar cell after surface sulfur treatments. After sulfurization, sulfur atoms were substituted for Selenium atoms at the surface layer of CIGS films to form a Cu(In,Ga)(S,Se)₂ absorber layer. The cell efficiency in the range 8-11% before sulfurization was improved to 14.3%.⁴⁰ Nawalage F Cooray et al.(1997) optimized large area ZnO films for graded band-gap CIGS based thin film mini modules. CIGS solar cells of efficiency 14% were obtained for an active area of 3.2cm² and an efficiency of 11% for an aperture area of 50cm².⁴¹

In 1998, Siham A Al Kuhaimi calculated the electron affinity difference in CIS/CdS solar cells from the variation in Voc with temperature. This difference (in the range 0.2 and 0.3eV) was found to be independent of process of cell fabrication. The use of CdZnS in the place of CdS reduced the value to slightly less than 0.1eV.⁴² R.Herberholz et al., made a distinction between bulk and interface states in CIS/CdS/ZnO by space charge spectroscopy. A type inversion at the surface of the absorber, held responsible for the suppression of interface recombination in efficient chalcopyrite based solar cells, was

confirmed through this⁴³ Vidyadharan et al., fabricated a 3.1% efficient CIS/CdS cell. In this work, all the layers were prepared using chemical bath deposition. Flourine doped SnO₂ and In were used as bottom and top electrodes respectively⁴⁴. Y.Hashimoto et al. investigated the deposition CdS buffer layer for CIGS solar cells. The reaction leading to the formation of CdS was controlled by the pH of the solution and most stoichiometric films were obtained for a pH of 11.8 which showed best performance⁴⁵ M.C.Artaud et al., deposited CIS by MOCVD and fabricated the first solar cell using MOCVD CIS⁴⁶ Se Han Kwon et al. fabricated an In₂Se₃/CIS cell as an alternative to CdS/CIS cell. A thin layer of CuIn₃Se₅(ordered vacancy compound), which was intrinsic or slightly n-type, was deposited on the CIS to form a pseudojunction with largely p-type CIS. This improved the performance of CIS/In₂Se₃ cell to reach an efficiency of 8.46%⁴⁷ R.N.Battacharya et al. fabricated CIGS based solar cells from electrodeposited and chemical bath deposited precursors. The device fabricated from electrodeposition resulted in an efficiency of 13.7% and that from chemical bath deposition showed 7.27% efficiency⁴⁸

In 1998, Lam et al. investigated the trap properties of CIGS/CdS/ZnO cell using Deep Level Transient Spectroscopy (DLTS). No minority carrier traps were observed in the CIS/CdS/ZnO cell, but both majority and minority carrier traps were observed for the CIGS/CdS/ZnO cell⁴⁹. M. Nishitani et al. analysed the temperature and illumination dependencies of CIS cell performance. The J_{sc} and Voc were linearly changed with the temperature in the range of 10°C to 70°C and the J_{sc} was proportional to the illumination intensity⁵⁰ Y Hashimoto et al. fabricated CIGS/CdS solar cell having 17% efficiency. Stoichiometric CdS layer deposited through CBD was used in this cell⁵¹ Takeshi Kojima et al., performed the stability evaluation of CIGS/CdS solar cells using C-V characteristics. Under irradiation, the test samples showed a little increase in efficiency and open-circuit voltage which showed their electrical durability to light irradiation. But the diode quality factor and series resistance showed large changes in value. After 4SUN irradiation, two samples in the same fabrication-lot showed new light absorption in the lower-energy gap range than sun of CIGS⁵² Tokio Nakada et al. fabricated superstrate-

type CIS/In_xSe_y cells by a low temperature process using sodium compounds. Na₂S was incorporated during film growth at a substrate temperature of 350°C. Even at relatively low substrate temperature, sodium compounds enhanced the (112) preferred orientation of the chalcopyrite structure and improved the cell performance. Efficiency of 7.5% was obtained for this cell ⁵³ Yasunori Okano et al. analysed CdS/CIS heterojunction using XPS measurement. An In-excess layer, which may form an ordered vacancy compound (OVC), was present at the surface and it remained even after chemical bath deposition of a CdS layer. The CIS solar cells fabricated with n-OVC surface layer exhibited higher cell efficiencies (8.7%) than those fabricated with p-surface layer ⁵⁴ Allen M Hermann (1998) et al tried low cost preparation of CIS films for CdS/CIS solar cells, by depositing CIS layer using electrodeposition. The precursor films were then loaded into a physical evaporation chamber and additional In and Se were added to the film (at 550°C) to adjust the final composition to CIS. The efficiency of this cell was 12% ⁵⁵ Y Hashimoto et al. (1998) fabricated CIGS/CdS solar cell with an efficiency of 17%. CIGS was prepared using thermal evaporation and CdS using CBD ⁵⁶ R N Bhattacharya et al.(1998) fabricated 13.7% efficient CuIn_{1-x}Ga_xSe₂(CIGS) based devices from electrodeposited and chemical bath deposited pre-cursors⁵⁷ Takayuki Negami et al. fabricated large area CIGS/CdS on 10 x 10 cm² with efficiency over 14% ⁵⁸ K Ramanathan et al.(2003) fabricated the cell having the structure CdS/CuInGaSe₂ with world record efficiency of 19.2%. Here CIGS was fabricated using co-evaporation ⁵⁹

In 2005, C-S Jiang et al. carried out the electrical modification in CIGS thin films by chemical bath deposition process of CdS films. Kelvin probe microscopy analysis revealed that, the potential peak on the grain boundaries becomes sharper after the sample is rinsed in high purity water, and the height of the potential peak becomes smaller after chemical treatments in a solution similar to that used in CBD of CdS films. This is expected to benefit the device performance ⁶⁰D Abou-Ras carried out structural and chemical investigations of CBD and Physical Vapour Deposited (PVD) CdS buffer layers and interfaces in CIGS-based thin film solar cells. PVD-CdS layers show much larger grain sizes than CBD-CdS layers and also a higher defect density at the CIGS/PVD-CdS

interface, owing to a larger lattice mismatch. In CIGS-CBD-CdS layers, the Cu and In interdiffusion provide an indication of an inversion of the near-interface region from p-type CIGS to n-type. The probable absence of this inversion in solar cells with PVD-CdS buffer layers is a possible reason for their lower efficiencies compared with the solar cells with CBD-CdS buffer layer⁶¹

The key issue in CIS based solar cell is reducing the absorber layer thickness and replacement of CdS. Here an attempt was made to achieve this. In the present work, CIS films of thickness 0.85 μm were prepared by thermal evaporation. In_2S_3 prepared using chemical spray pyrolysis was used as the buffer layer.

5.3 Experimental

CIS thin films were prepared using sequential elemental evaporation and the structure was glass/In/Se/Cu. In and Se were evaporated at a substrate temperatures of 100°C and 50°C respectively. Cu was evaporated at room temperature. The sample was annealed at a temperature of 400°C in vacuum at a pressure of 2×10^{-5} mbar for one hour. Two layers of CIS were prepared; the bottom layer with a resistivity of 0.08 Ωcm and a top layer with a resistivity of 7916 Ωcm .

In_2S_3 thin films were prepared using chemical spray pyrolysis. In this, the films were deposited by spraying aqueous solutions of Indium chloride (InCl_3) and Thiourea ($\text{CS}(\text{NH}_2)_2$) using compressed air as carrier gas and the substrate temperature was 300°C \pm 5°. The substrate was kept at this temperature for one hour before the deposition for stabilization of the temperature. The volume of the solution was varied to get different thicknesses. The top electrode, Ag, was deposited using thermal evaporation at a pressure of 2×10^{-5} mbar. After deposition of electrode, all the samples were annealed at 100°C for 30 minutes at a pressure of 2×10^{-5} mbar. This annealing was to make the contact between electrode (Ag) and In_2S_3 smoother, by decreasing the contact resistance. The I-V characteristics of the cell were measured under AM1.5 condition. The I-V characteristics of the cell were measured using Keithley 236 Source Measure Unit interfaced by GPIB

card and ICS software. The junction analysis was performed by varying the thickness of the buffer layer, sample stoichiometry and post deposition treatment.

5.4 Layer properties for the device fabrication

5.4.1 Bottom electrode

(a) Molybdenum: Molybdenum was used as one of the bottom electrodes for the cell, as Mo has Ohmic contact with CIS. The Mo film in the present work had a thickness of $0.2\mu\text{m}$ and a sheet resistance of $1\Omega/\text{cm}^2$. Mo is known to be the best contact to CIS solar cells.

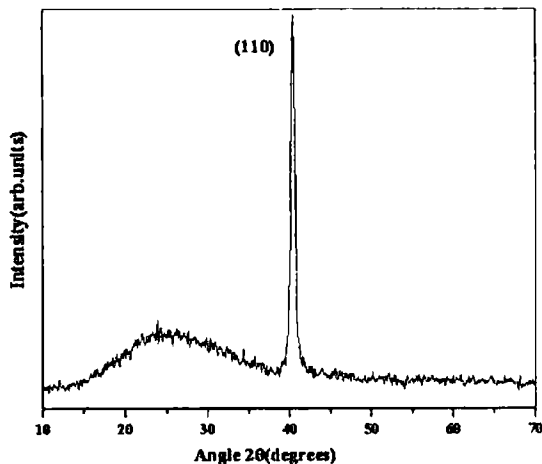


Fig 5.1: X-ray diffractogram of Molybdenum

(b) Indium Tin Oxide (ITO): ITO used in the present work had a thickness of $0.2\mu\text{m}$ and a sheet resistance of $10\Omega/\text{cm}^2$. Fig 5.2 shows the X-ray diffractogram of the ITO with preferred orientation along (222) plane.

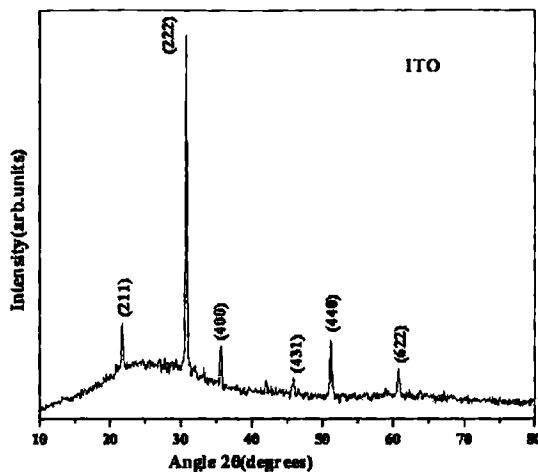


Fig 5.2: X-ray diffractogram of Indium Tin Oxide (ITO)

5.4.2 Absorber layer

CIS double layer of thickness $0.9\mu\text{m}$ was used as the absorber layer. A highly conductive layer of resistivity $0.08\Omega\text{cm}$ was deposited as the bottom layer to act as a p^+ layer thus reducing back surface recombination.

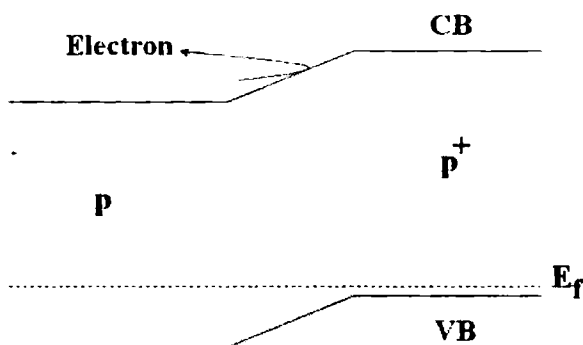


Fig.5.3: The p^+ layer acting as an electron reflector

The top layer was more resistive with a resistivity of $7916\Omega\text{cm}$. The cross-sectional SEM shows the layered structure of this double layer.

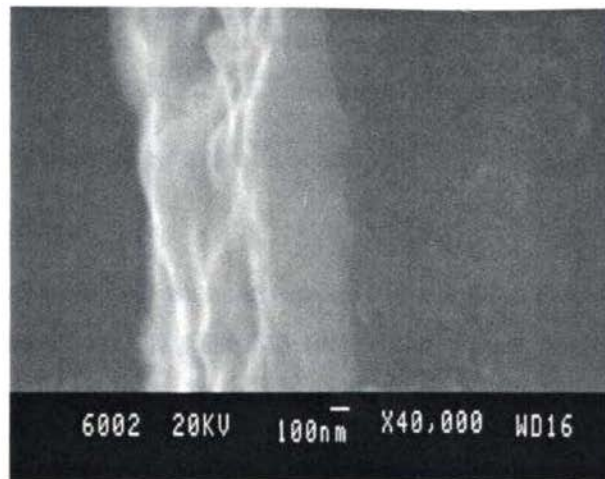


Fig 5.4: Cross-sectional SEM of the double layer

Detailed characterizations of the absorber layer using XRD, optical absorption, EDAX, XPS, Raman spectroscopy, Resistivity measurement, Photoluminescence and Stylus profiler are given in the last chapter.

5.4.3 Buffer layer

In_2S_3 was used as the buffer layer. The optimization of the sample was reported earlier by our group.⁵⁶ In the present work, In_2S_3 with In/S ratio of 2/8, 1.2/8 and 2/5 were mainly used for the junction fabrication.

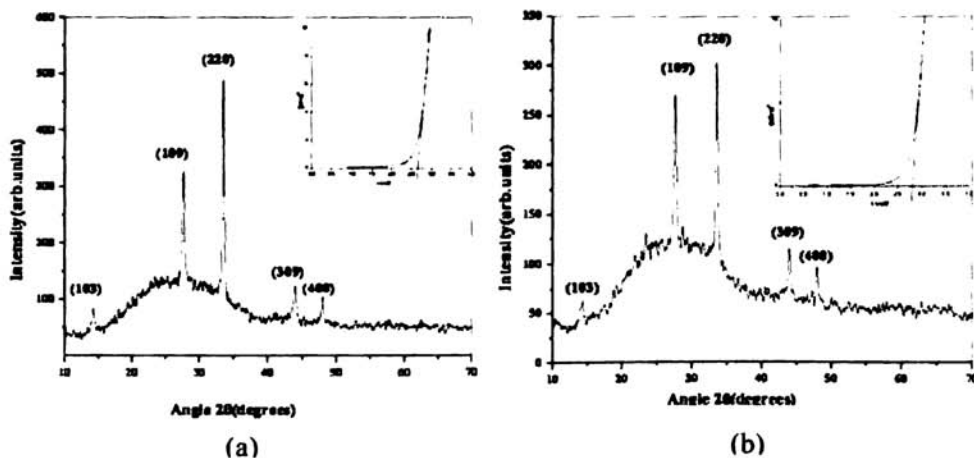


Fig 5.5: XRD of In_2S_3 with In/S ratio of (a) 2/8 (b) 1.2/8

Fig 5.5(a) and (b) show the X-ray diffractogram and absorption spectra of In_2S_3 with In/S ratios 2/8 and 1.2/8 respectively. The d values coincided with that of $\beta\text{-In}_2\text{S}_3$ in standard JCPDS data card (25-390) with preferential orientation along the (220) plane at $2\theta = 33.45^\circ$. The crystallinity was better for In_2S_3 with In/S ratio of 2/8. The grain size was 35nm for In_2S_3 with In/S ratio 2/8. The absorption spectra of the sample were shown in the inset of the XRD and the band gap of the sample was found to be 2.65eV. The grain size of the sample with In/S ratio 1.2/8 was 37nm and band gap 2.8eV.

5.4.4 Top electrode

For the junction with Mo as bottom electrode, Aluminium (Al) was used as the top electrode. Al electrode was made in the form of grids with 1mm spacing between them. Silver was used as the top electrode for the cells with ITO as the bottom electrode and this was made in the form of blocks. Al and Ag were deposited using thermal evaporation.

5.5 Structure of the cell

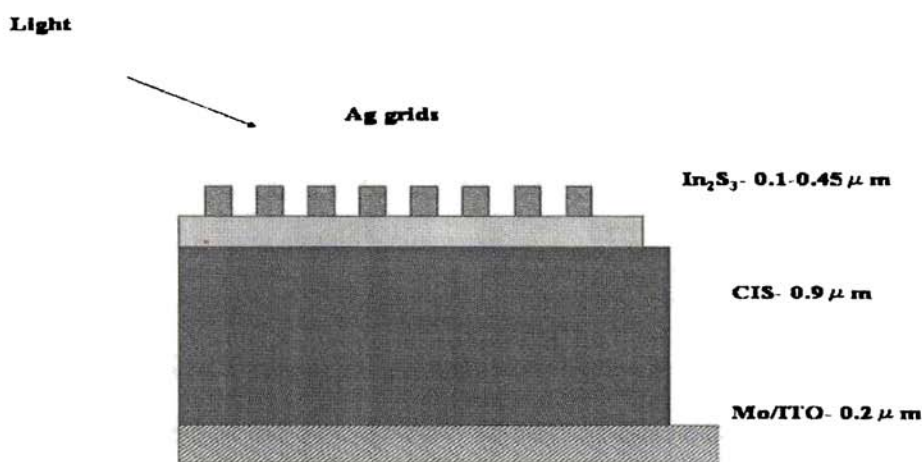


Fig 5.6: Structure of the cell

Fig 5.6 shows the structure of the cell. The structure consists of a $0.2\mu m$ thick Molybdenum/ITO as bottom electrode. CIS double layer with a thickness of $0.9\mu m$ was fabricated over this. The n-type In_2S_3 having different ratios of In/S (1.2/8, 2/8 and 5/8) layer was sprayed on top of the CIS layer to form the junction. The thickness of In_2S_3 was varied from $0.1\mu m$ to $0.45\mu m$. Ag/Al was used as the top electrode, in all the cases.

5.6 Variations on Window layer

The thickness and In/S ratio of the buffer layer was varied for optimization of the junction.

5.6.1. Effect of thickness of the buffer layer

To study the effect of variation of thickness, the In/S ratio was first fixed at 2/8. The volume of the In_2S_3 solution was varied to get different thicknesses. The variation in thickness with different volumes is given below.

Table 5.1: Variation of In_2S_3 thickness with volume of the solution

Volume of In_2S_3	Thickness (μm)
25	0.10
50	0.25
80	0.35
100	0.45

The CIS/ In_2S_3 junction was subjected to post deposition annealing treatment at $300^\circ C$ for 30 minutes in air. In all the cases the sample was etched by ion beam before depositing the top electrode. This process removed the impurities and dust particles over the film surface.

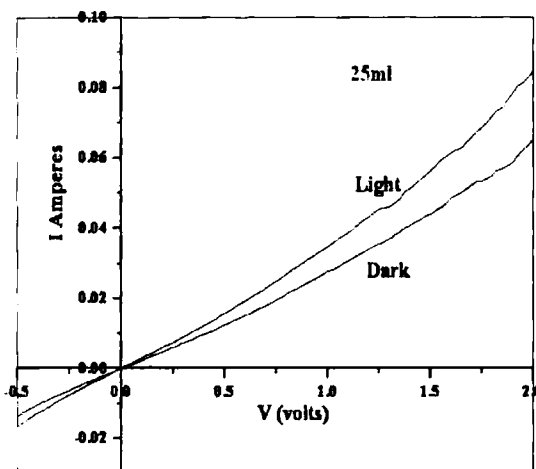
(i) In_2S_3 with a thickness of $0.1\mu\text{m}$ 

Fig 5.7: I-V Characteristics of the junction with In_2S_3 thickness of $0.10\mu\text{m}$

The I-V characteristics of the junction with In_2S_3 thickness of $0.10\mu\text{m}$ is shown in Fig. 5.7 under the dark and illuminated condition. The volume of the sprayed solution was 25 ml. The graph showed a pure resistive behaviour which indicated the absence of an active junction for this structure. The forward resistance of the structure was lowered upon illumination which indicated that the structure had some response to illumination. This kind of behaviour might be due to the diffusion of the In_2S_3 buffer layer fully into the CIS layer so that there was no free In_2S_3 layer in this cell. Hence it was concluded that the thickness of the buffer layer should be increased

(ii) In_2S_3 with a thickness of $0.25\mu\text{m}$

Thickness of the In_2S_3 layer was increased to $0.25\mu\text{m}$ by increasing the volume of the solution to 50ml and the deposition process was repeated.

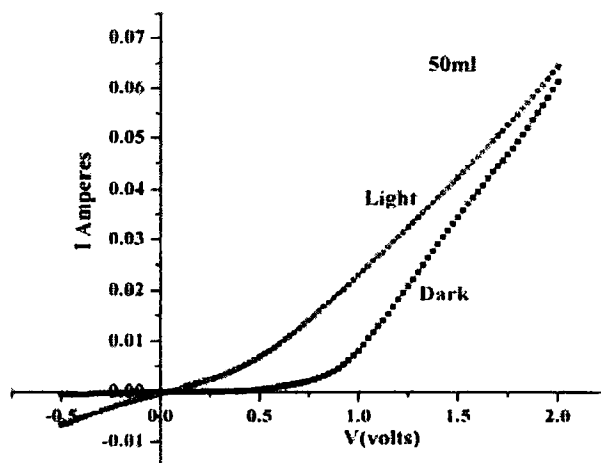


Fig 5.8: I-V Characteristics of the junction with In_2S_3 thickness of $0.25\mu\text{m}$

The I-V characteristics (fig 5.8) showed the nature of p-n junction diode, even though the junction was not perfect. The resistance and diode quality factors were calculated from the I-V characteristics in the first quadrant of the plot. The series resistance R_s of the cell is measured from the inverse of the slope of the dark I-V characteristics. This parameter is an indication of the quality of the bulk material. The series resistance arises from the resistance of the cell material to the current flow, particularly through the front surface to the contacts and from resistive contacts. Shunt resistance is obtained from the inverse of the slope of the I-V characteristics in the third quadrant of the plot. The shunt resistance (R_{shunt}) is a measure of leakage through the cell, around the edges of the device and between contacts. Very low shunt resistance reduces V_{oc} , but does not affect I_{sc} . The cell parameters obtained are given in the table 5.2.

Table 5.2: Cell parameters

Cell area	0.48 cm ²
J _{sc}	1.05 mA/cm ²
V _{oc}	36 mV
R _s	19 Ω
R _{sh}	1142 Ω
Diode quality factor, A	3.8

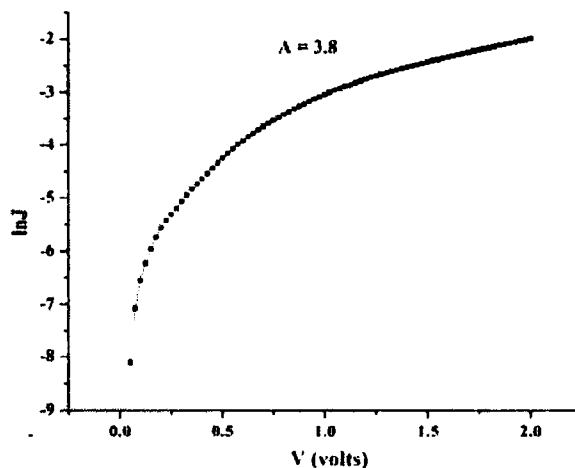
**Fig.5.9: $\ln J$ vs V graph**

Fig 5.9 shows $\ln J$ vs V graph, from the slope of which diode quality factor A was calculated. For a highly idealized junction, the series resistance will be < 0.5 and A between 1 and 1.5.⁵⁷ The increase of A from 1 to 2 is attributed to the increase in density of recombination centers. An ideality factor of 2 is an indicative of recombination, mainly in the depletion region; whereas an ideality factor close to 1 means that the recombination takes place mainly in the bulk. High values of $A > 2$ may be due to the

various phenomena such as shunt resistance effects or non-uniformities in the distribution of recombination centers.⁵⁸ In the present case we obtained a value of 3.8 for diode quality factor.

(iii) In₂S₃ with a thickness of 0.35μm

The thickness of the buffer layer was increased to 0.35μm by increasing the volume of the solution to 80ml. Fig 5.10 shows I-V characteristics of the junction.

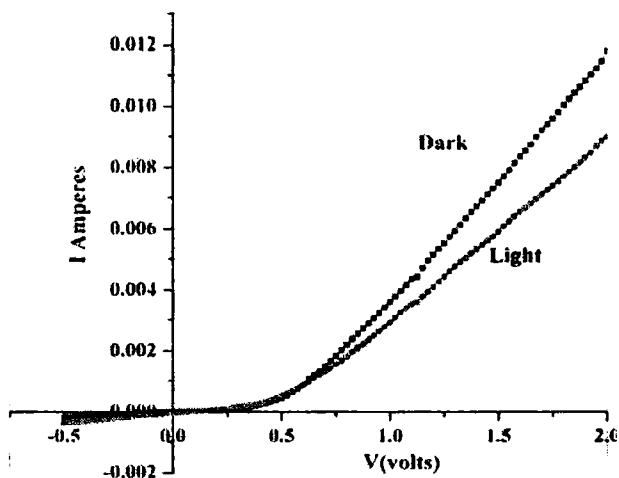


Fig 5.10: I-V Characteristics of the junction with In₂S₃ thickness of 0.35μm

Table 5.3 Cell parameters

Cell area	0.15 cm ²
J _{sc}	0.32 mA/cm ²
V _{oc}	80 mV
R _s	1276 Ω
R _{sh}	3222 Ω
Diode quality factor, A	4.3

The short circuit current decreased to $0.32\text{mA}/\text{cm}^2$ while the open circuit voltage increased to 80mV . This may be due to the increase in shunt resistance. As the thickness of the In_2S_3 layer was increased, the intensity of light reaching the junction may be low and this lead to the decreased J_{sc} .

(iv) In_2S_3 with a thickness of $0.45\mu\text{m}$

Thickness of the In_2S_3 layer was increased to $0.45\mu\text{m}$ by using 100ml solution. Fig 5.11 shows the I-V characteristics of the junction.

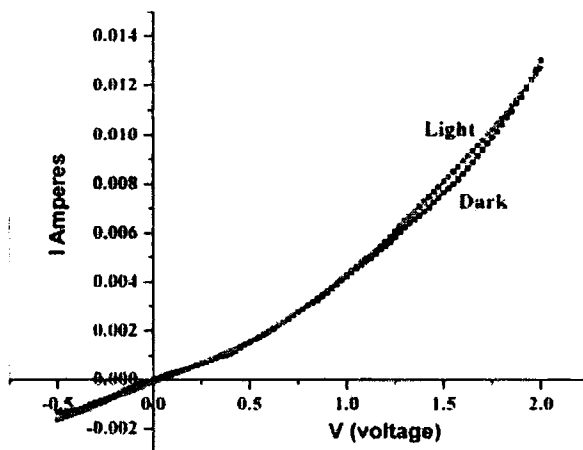


Fig 5.11: I-V Characteristics of the junction with In_2S_3 thickness of $0.45\mu\text{m}$

With increase in In_2S_3 thickness, the junction was getting deteriorated. The shunt resistance decreased drastically to 306 .

The cell parameters are given in the table 5.4. Both J_{sc} and V_{oc} decreased with the increase in thickness. The reduced intensity of the light reaching the junction and the decreased shunt resistance could have led to this decrease in cell parameters.

From the above analysis, it was found that the In_2S_3 layer with a thickness of $0.25\mu\text{m}$ was having better property

Table 5.4: Cell parameters

Cell area	1.2 cm ²
J _{sc}	0.06 mA/cm ²
V _{oc}	27 mV
R _s	148 Ω
R _{sh}	306 Ω
Diode quality factor, A	4.7

5.6.2 Effect of variation in In/S ratio

(i) In_2S_3 layer with In/S ratio of 1.2/8

The In/S ratio in In_2S_3 was changed from 2/8 to 1.2/8. The thickness of this sample was also varied from 0.10 μm to 0.450 μm, as in the earlier case. With In_2S_3 thickness of 100nm, the I-V plot was linear as in the case of In/S ratio of 2/8. The thickness was further increased to 0.25μm by increasing the volume of the solution. Fig 5.12 shows the I-V characteristics of this junction.

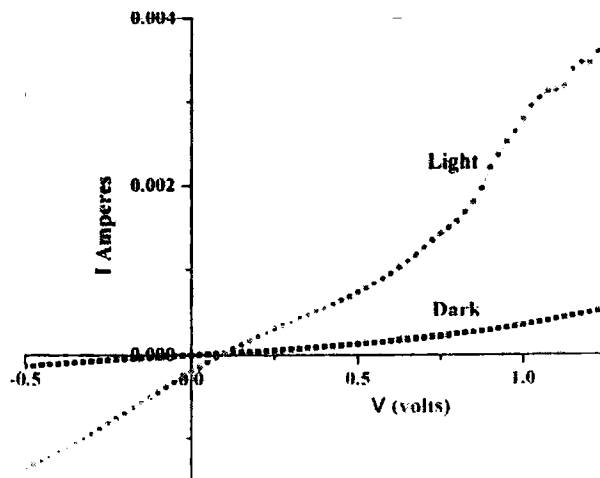
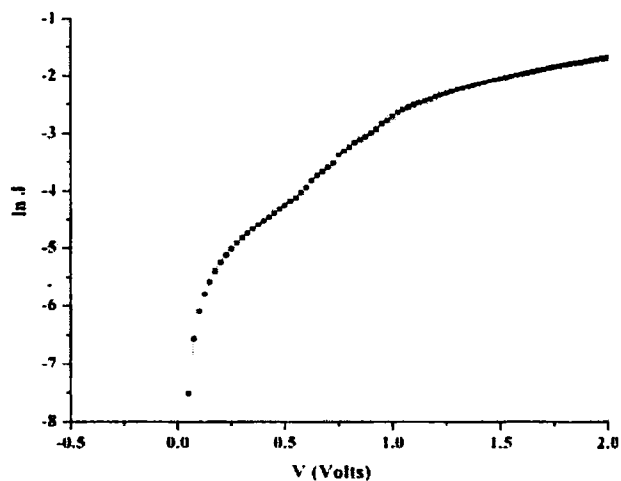
**Fig 5.12:** I-V Characteristics of the junction with In/S ratio of 1.2/8

Table 5.5: Cell parameters

Cell area	0.12 cm ²
J _{sc}	1.72 mA/cm ²
V _{oc}	90 mV
R _s	74 kΩ
R _{sh}	464 kΩ
Diode quality factor, A	5.7

The short circuit current increased to 1.72mA/cm². The V_{oc} also increased to 90mV. Both the series and shunt resistance increased. In₂S₃ with In/S ratio of 1.2/8 is more photosensitive than In/S 1.2/8 and this might have lead to the increased current. Figure 5.13 shows the lnJ vs V graph from which A was found to be 5.7.

**Fig.5.13:** lnJ vs V graph

On increasing the thickness beyond this, the device performance deteriorated as observed in the case of In₂S₃ with In/S ratio 2/8. The parameters obtained for this thickness are given below.

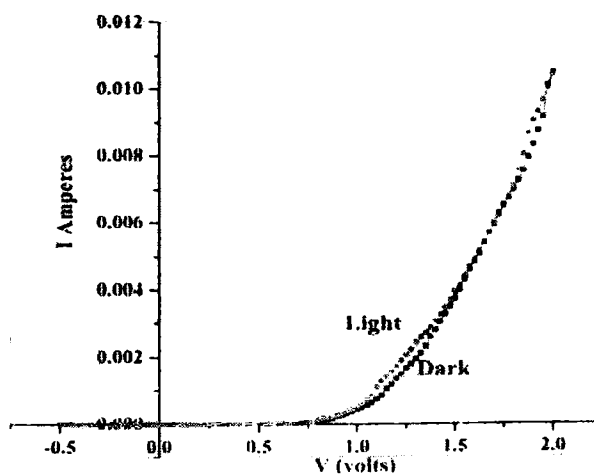
Table 5.6: Variation of V_{oc} and J_{sc} with thickness

In_2S_3 thickness (μm)	J_{sc} (mA/cm ²)	V_{oc} (mV)
0.10	0	0
0.25	1.72	90
0.35	0.02	24
0.45	0.06	27

From the above analysis, it is concluded that, the thickness of 0.25 μm was the optimum thickness for the present structure. The Molybdenum layer of some samples peeled off for which may be due to the heat treatments at 400°C (twice), 300°C (for In_2S_3 deposition) and 100°C (electrode annealing). Hence we changed the electrode material to Indium doped Tin Oxide (ITO).

(ii) In_2S_3 layer with In/S ratio of 2/5

In_2S_3 layer was made more conductive by making the In/S ratio of 2/5. The I-V characteristics is shown in fig.5.14 and the cell parameters are given in table 5.7

**Fig 5.14:** I-V Characteristics of the junction with In/S ratio of 2/5

Here the V_{oc} increased to 162 mV, probably due to the increase in shunt resistance. But short circuit current decreased to $0.93 \mu\text{A}/\text{cm}^2$.

Table 5.7: Cell parameters

Cell area	0.09 cm^2
J_{sc}	$0.93 \mu\text{A}/\text{cm}^2$
V_{oc}	162 mV
R_s	92 Ω
R_{sh}	119 k Ω
Diode quality factor, A	3.8

Table 5.8: Variation of cell parameters with variation in In/S ratio

In/S ratio	$J_{sc} \text{ mA}/\text{cm}^2$	$V_{oc} \text{ mV}$	A
2/8	1.05	36	3.8
1.2/8	1.72	90	3.44
.2/5	0.93×10^{-3}	162	6.95

Table 5.8, shows the variation in V_{oc} and J_{sc} with variation in In/S ratio. On analyzing the table, it can be concluded that 1.2/8 was best suited for device fabrication and hence this ratio was used in the further fabrication process.

5.7 In_2S_3 in the ratio 1.2/8 on ITO

ITO of thickness $0.2 \mu\text{m}$ and resistance of $10 \Omega\text{cm}^2$ was taken as the bottom electrode. ITO Thickness of the In_2S_3 which gave the best value for J_{sc} and V_{oc} was again selected for the cell prepared on ITO also and the characteristics showed nearly the same values of

J_{sc} and V_{oc} . Fig 5.15 shows the I-V characteristics of the junction and table 5.9 gives the parameters of this cell.

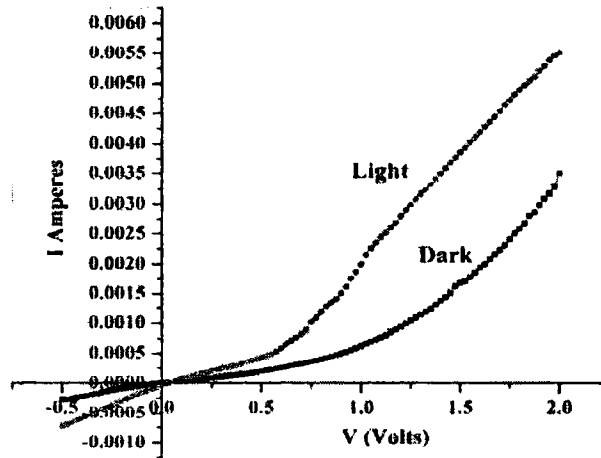


Fig 5.15: I-V Characteristics of the junction with In/S ratio of 1.2/8

Table 5.9: Cell parameters

Cell area	0.03cm ²
J_{sc}	1.28mA/cm ²
V_{oc}	35mV
R_s	320.5Ω
R_{sh}	1628 Ω
Diode quality factor, A	5.4

The fig 5.16 depicts the cross-sectional SEM of this $\text{CIS}/\text{In}_2\text{S}_3$ junction. The total thickness of the cell was $\sim 1\mu\text{m}$. The layered structure of CIS and In_2S_3 could be seen in the graph.

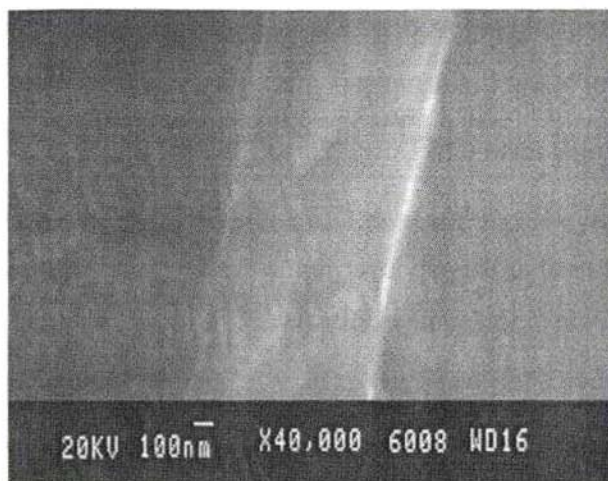


Fig 5.16: Cross-sectional SEM of CIS/In₂S₃ junction

5.8 Variation in the absorber layer

5.8.1 Junction with Stoichiometric CIS

The highly stoichiometric sample with resistivity 2 Ω cm was used as top layer. Fig 5.17 shows the I-V characteristics of this junction. In₂S₃ with In/S ratio of 1.2/8 was used as the buffer layer

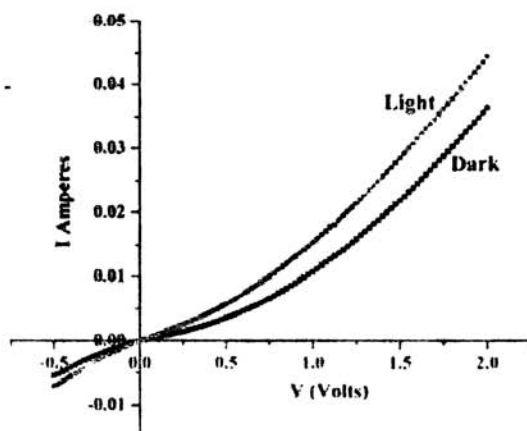


Fig 5.18: I-V characteristics of the junction fabricated using stoichiometric sample

From the fig, it is seen that the junction showed almost linear behaviour. This may be due to the high conductivity of the CIS sample.

5.8.2 Junction with single layer CIS

Junction was fabricated using single layer CIS with In_2S_3 . The layer having resistivity of $7916\Omega\text{cm}$, which was used as the top layer in the earlier cases, was used here. Fig.5.19. V_{oc} was 25mV and J_{sc} was $0.3\text{mA}/\text{cm}^2$ in this case.

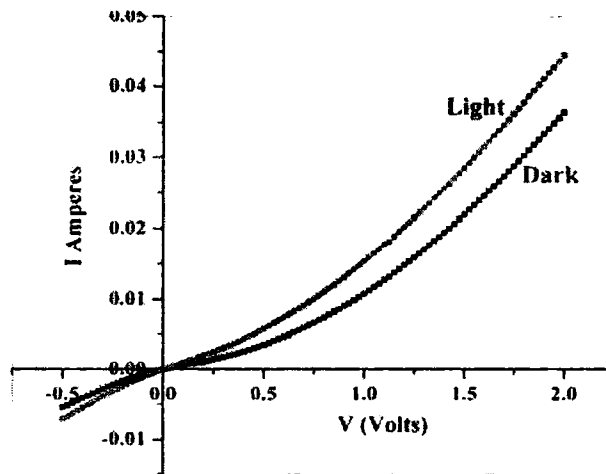


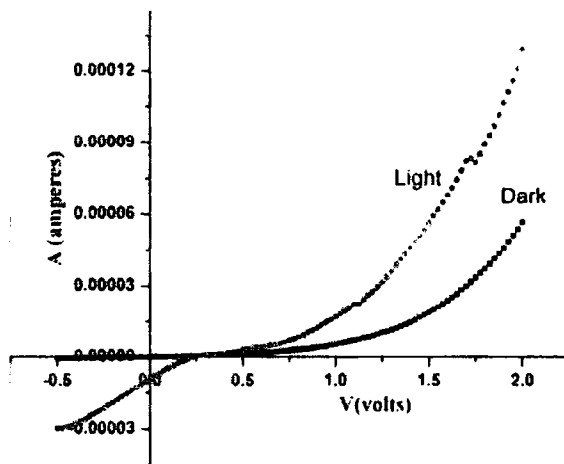
Fig 5.19: The I-V characteristics of the junction with single layer CIS

5.9 Effect of post deposition annealing

The analysis of the junction with variation in In_2S_3 stoichiometry showed that In/S ratio of 1.2/8 was found to be the better. The thickness was also optimized to be $0.25\mu\text{m}$ for the best performance. At this time, the effect of post deposition annealing was analyzed. The junction was analyzed by subjecting the sample to a post annealing of 30 min in air at a temperature of 300°C , without post annealing and by quickly removing from the hot plate after deposition. The cell parameters obtained are given in table 5.10.

Table 5.10: Variation of cell parameters with post deposition conditions

Post deposition treatments	V_{oc} (mV)	J_{sc} (mA/cm ²)
Quickly removed from the hot plate	104	0.03
No post deposition annealing, kept the samples on the hot plate	245	0.1
30 minutes annealed	35	1.28

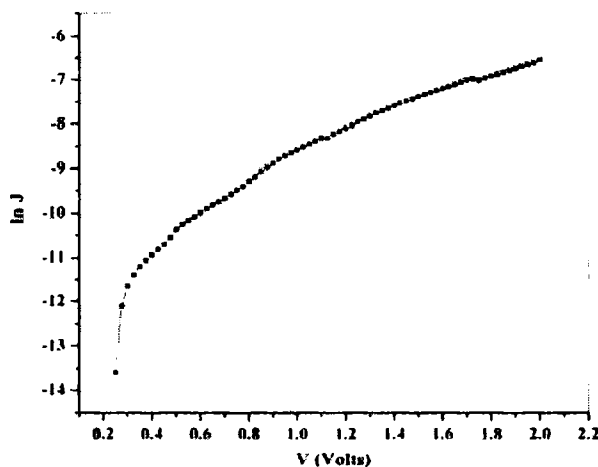
**Fig 5.20:** I-V Characteristics of the junction without post deposition annealing

Without post-deposition annealing, the voltage increased to 245 mV meanwhile current decreased to 0.1 mA/cm². The post deposition annealing caused the oxygen content in the film to increase, leading to an increase in the conductivity and hence a decrease in photosensitivity. Hence the film with less O content should have a better photosensitivity.

Table 5.11: Cell Parameters

Cell area	0.09 cm ²
J_{sc}	0.1 mA/cm ²
V_{oc}	245 mV
R_s	14 k Ω
R_{sh}	699 k Ω
Diode quality factor A	4.9

The diode quality factor was found to be 4.9. Both the series and shunt resistances increased in this case probably because of the decrease in oxygen concentration.

**Fig.5.21: lnJ vs V graph**

5.10 Conclusions

A trial for $\text{CIS}/\text{In}_2\text{S}_3$ was made with vacuum evaporated p-type CIS and spray pyrolysed n-type In_2S_3 . The thickness and composition of In_2S_3 were varied in the films. We could achieve an observable shift in the I-V characteristics on illumination under AM1.5 radiation. This can be improved with further studies.

References

1. J Kessler, J Wennerberg, M Bodegard, L Stolt, Sol. Energy Mater.Sol.Cells 75(2003)35
2. M Powalla, B Dimmler, R Schaeffler, G Voorwinden, U Stein, H D Mhring, F Kessler, D Hariskos, Proceedings 19th European Photovoltaic Solar Energy Conference, Paris, France 2004
3. Tuttle, J R, Szalaj A, Keane J, 2000, Proc.28th IEEE Photovoltaic Specialists Conf., Anchorage, p.1042
4. L.L. Kazmerski, F.R.White and G.K.Morgan, Appl.Phy.Lett. 29 (1976) 268
5. B.Tell and P.M.Bridenbaugh, Appl.Phy.Lett.48 (1977) 2477
6. P.E.Russel, O.Jamjoum, R.K.Ahrenkiel, L.L. Kazmerski, R.A.Mickelsen and W.S.Chen , Appl.Phy.Lett. 40, No.11, 1982(995M.Eron and A.Rothwar, J.Appl.Phys.57 (6), 1985(2275
7. R.K.Ahrenkiel and R.J.Matson, Appl.Phy.Lett 46 (1985) 877
8. Poola Raja Ram, R.Thangaraj, A.K.Sharma and O.P.Agnihotri, Solar Cells, 14(1985) 123
9. Rommel Noufi and John Dick, J.Appl.Phys.58 (10) (1985) 3884
10. A Herms, J.R.Morante, J.Millan, A.Cornet and E.Bertran, Thin Solid Films, 125(1985) 107
11. R.E.Hollingsworth and J.R.Sites, Solar Cells, 16(1986) 457
12. R.Noufi, R.J.Matson, R.C.Powell, C.Herrington, Solar Cells16(1986) 479
13. R.J.Matson, Rommel Noufi, R.C.Powell and D.Cahen, Solar Cells, 16(1986) 495
14. Allen Rothwarf, Solar Cells, 16(1986) 567
15. R.W.Birkmire, L.C.Dinetta, P.G.Lasswell, J.D.Meakin and J.E.Philips, Solar Cells, 16(1986) 419
16. J.D.Meakin, R.W.Birkmire, L.C.Dinetta, P.G.Lasswell, J.E.Phillips, Solar cells 16(1986) 447
17. J.M.Stewart, Solar Cells, 19(1986-1987) 237
18. David Cahen and Rommel Noufi, Appl.Phy.Lett.54 (1989)558
19. N.Christoforou, J.D.Leslie, S.Damaskinos, Solar Cells, 26(1989) 197
20. Brian.J.Brown, Clayton.W.Bates, J.Appl.Phys.68(5)(1990) 2517
21. W.N.Shaferman, R.W.Birkmire, P.E.McCandless, A.Mondal, J.E.Philips, R.D.Varrin, Solar Cells, 30(1991) 61
22. Ji-Beem Yoo, Alan L Fahrenbruch, Richard H Bube, Solar Cells, 31(1991) 171
23. Lars Stolt, Jonas Hedstrom, John Kessler, Martin Ruckh, Karl-Otto Velthaus, Hans-Werner Schock. Appl.Phys.Lett .62(6), 1993, 597
24. J.S.Chen, E.Kolwa, C.M.Garland. M.A.Nicolet, R.P.Ruiz, Thin Solid Films, 219(1992)183

25. D.Schmid, M.Ruckh, F.Grunwald, H.W.Schock, *J.Appl.Phys.* **73**(6) 1993
26. M Nishitani, T Negami, S Kohiki, M Terauchi, T Wada, T Hirao, *J.Appl.Phys.* **74**(3) 1993
27. L-Chung Yang, A.Rocket, *J.Appl.Phys.* **75**(2) 1994
28. Andrew M Gabor, John R Tuttle, David S Albin, M.A.Contreras, R.Noufi, A.M.Hermann, *Appl.Phys.Lett.* **65**(2) 1994
29. G E Hassan, M R I Ramadan, H El-Labani, M H Badawi, S Aboul-Enein, M J Carter, R Hill *Semicond.Sci.Technol.* **9**(1994)1261
30. M.Nishitani, M Ikeda, T Negami, S Kohiki, N Kohara, M Terauchi, H Wada, T Wada, *Sol. Energy Mater. Sol. Cells* **35**(1994) 203
31. Tokio Nakada, Ryoji Onishi, Akio Kunioka, *Sol. Energy Mater. Sol. Cells* **35**(1994) 209
32. W.N.Shaferman, Reiner Klenk, Brian E. McCandless, *J.Appl.Phys.* **79**(9), 1996
33. A.M.Fernandez, P.J.Sebastian, R.N.Battacharya, R.Noufi, M.Contreras, A.M.Hermann, *Semicond.Sci.Technol.* **11**(1996)964
34. Bulent M Basol, Vijay K Kapur, Craig R Leidholm, Arvind Halani, Kristen Gledhill, *J.Appl.Phys.* **43**(1996) 938
35. Katsumi Kushiya, Muneyori Tachiyuki, Takahisa Kase, Ichiro Sugiyama, Yoshinori Nagoyi, Daisuke Okumura, Masao Sato, Osamu Yamase, Hiroshi Takeshita, *Sol. Energy Mater. Sol. Cells* **49** (1997) 277
36. S.N.Qiu, W.W.Lam, C.X.Qui, I.Shih, *Applied Surface Science* **113/114**(1997) 764
37. V Alberts, R Herberholz, T Walter, H.W.Schock, *J.Phys.D:Appl.Phys.* **30**(1997) 2156
38. M Topic, F Smole, J Furlan, *Sol. Energy Mater. Sol. Cells* **49**(1997) 311
44. Tokio Nakada, Hiroki Ohbo, Takayuki Watanabe, Hidenobu Nakazawa, Maasahiro Matsui, Akio Kunioka, *Sol. Energy Mater. Sol. Cells* **49**(1997) 285
45. Nawalage F Cooray, Katsumi Kushiya, Atsushi Fujimaki, ichiro Sugiyama, Tadayuki Miura, Daisuke Okumura, Masao Sato, Mineo Ooshita, Osamu Yamase, *Sol. Energy Mater. Sol. Cells* **49**(1997) 291
39. Siham A Al Kuhaimi, *J.Appl.Phys.* **52**(1998) 69
40. R. Herberholz, M.Igalson, H.W.Schock, *J.Appl.Phys.* **83**(1) 1998
41. P.K.Vidyadharan Pillai and K.P.Vijayakumar, *Sol. Energy Mater. Sol. Cells* **51**(1998) 47
42. Y.Hashimoto, N.Kohara, T.Negami, N.Nishitani, T.Wada, *Sol. Energy Mater. Sol. Cells* **50**(1998)71
43. M C Artaud, F Ouchen, L Martin, S Duchemin, *Thin Solid Films* **324**(1998) 115

44. Se Han Kwon, Byung Tae Ahn, Seok Ki Kim, Kyung Hoon Yoon, Jinsoo Song, *Thin Solid Films* **323**(1998) 265
45. R N Bhattacharya, W Batchelor, J E Granata, F Hasoon, H Wiesner, K Ramanathan, J Keane, R. N Noufi, , *Sol. Energy Mater. Sol. Cells* **55**(1998) 83
46. W.W Lam, L S Yip, J E Greenspan, I Shih, *Sol. Energy Mater. Sol. Cells* **50**(1998) 57
47. M Nishitani, N Kohara, T Negami. T Wada, S Igari, R Shimokawa, *Sol. Energy Mater. Sol. Cells* **50**(1998) 63
48. Y Hashimoto, N Kohara, T Negami, N Nishitani, T Wada, *Sol. Energy Mater. Sol. Cells***50**(1998) 71
49. Takeshi Kojima, Tadamas koyanagi, Kuniomi Nakamura, Takeshi Yanagisawa, Kiyoshi Takahisa, Mikihiko Nishitani, Takahiro Wada, *Sol. Energy Mater. Sol. Cells***50** (1998) 87
50. Tokio Nakada, Tomoyuki Kume, Akio Kunioka, *Sol. Energy Mater. Sol. Cells***50** (1998) 97Yasunori Okano, Tokio Nakada, Akio Kunioka, *Sol. Energy Mater. Sol. Cells***50**(1998) 105Allen M Hermann, Richard Westfall, Rikard Wind, *Sol. Energy Mater. Sol. Cells* **52**(1998) 355
51. Y Hashimoto, N Kohara, T Negami, N Nishitani, T Wada, *Sol. Energy Mater. Sol. Cells* **50**(1998) 71
52. R N Bhattacharya, W Batchelor, J E Granata, F Hasoon, H Weisner, K Ramanathan, J Keane, R N Noufi, *Sol. Energy Mater. Sol. Cells* **55**(1998) 83
53. Takayuki Negami, Takuya Satoh, Yasuhiro Hashimoto, Shiro Nishiwaki, Shin-ichi Shimakawa, Shigeo Hayashi, *Sol. Energy Mater. Sol. Cells* **67**(2001) 1
54. Kannan Ramanathan, Miguel.A.Contreras, Craig L.Perkins, Sally Asher, Falah S. Hasoon, James Keane, David Young, Manuel Romero, Wyatt Metzger, Rommel Noufi, James Ward and Anna Duda, *Prog. Photovolt: Res.Appl.*2003; 11; 225-230 (DOI: 10.1002/pip, 494)
55. C-S Jiang, R Noufi, K Ramanathan, H R Moutinho, M M Al-Jassim, *J.Appl.Phys.***97**(2005), 053701
56. D Abou-Ras, G Kostorz, A Romeo, D Rudmann, A N Tiwari, *Thin Solid Films* **480-481**(2005) 118
57. Teny Theresa John, S.Bini, Y Kasiwaba, T Abe. Y Yasuhiro, C Sudha kartha, K P Vijayakumar, *Semicond.Sci.Technol.***18**(2003) 491
58. R N Battacharya. W Batchelor, J E Granata. F Hasoon. H Wiesner. K Ramanathan. J Keane, R N Noufi. *Sol.Energy Mater.Sol.Cells* **55**(1998)83
59. P Mialhe. J P Charles. A Khoury. G Bordure. *J. Phys.D:Appl.Phys.***19**(1986) 483

Chapter 6

Summary and Conclusions

The mass consumption of fossil fuels, which is getting depleted and also leading to pollution, has led to an energy crisis. 'Solar Photovoltaics' has emerged as one of the leading solutions to the energy crisis. Photovoltaic is an almost maintenance free clean energy technology. This era started with first generation (Si) technology which does not satisfy the economical requirements. With the idea of fabricating cheaper solar cells, the second generation –'Thin Film' technology was developed.

Among the candidates for thin film solar cells, CuInSe_2 emerged to be one of the ideal absorber layers. Now, the key issues in the field of CIS solar cells are the reduction of thickness of the absorber layer and replacement of CdS with another non-toxic buffer layer for this absorber. The main focus of this thesis is on some aspect of these issues.

In the present work, Sub-micrometre thick CuInSe_2 films were prepared using different techniques viz, selenization through chemically deposited Selenium and Sequential Elemental Evaporation. Among these two the first technique was economically viable and eco-friendly method; in deposited this, CuInSe_2 thin films were prepared using chemical bath deposited Selenium films. However, in this technique, the stoichiometry of the films could not be controlled critically and the repeatability of the samples was poor. CuInSe_2 films were then prepared through two different techniques (viz, Stacked Elemental Layer technique and Thermal diffusion of Copper into In_2Se_3 bilayer) using Se films deposited with the help of chemical bath deposition technique, as the bottom layer. Stoichiometry of the sample was varied over a wide range by varying Cu and/or In content and a comparison of the properties of the samples prepared using these different

techniques were made. Even though both sets of films showed same variation in crystallinity, grain size and band gap with Cu to In ratio, photosensitivity was found to be more for those prepared using thermal diffusion of Cu into In_2Se_3 . Photosensitivity, being a measure of minority carrier generation, the method of thermal diffusion was found to be more suitable growth process for CuInSe_2 thin films for solar cell applications. The films showed good crystallinity with sphalerite structure which could be confirmed from XRD and Raman studies. These CuInSe_2 films were found to be free from voids and pinholes. Defect analysis was performed using temperature dependant photoluminescence and conductivity studies.

The main advantage of this technique was that, highly toxic Se vapor or H_2Se could be completely avoided. An attempt to device fabrication was also made using vacuum evaporated CdS as buffer layer. But photovoltaic effect could not be observed at the junction. Even though this preparation technique was eco-friendly, it had the disadvantage that, the thickness of Se layer could not be increased over $0.25\mu\text{m}$ and hence the overall absorber thickness was limited to $<0.5\mu\text{m}$. The problems with this lower thickness are reduced absorption of incoming photons and higher back surface recombination. As techniques like light trapping and back reflectors were not employed in this configuration, slightly increased thickness ($0.5\text{-}1\mu\text{m}$) should be used. In this technique, the overall absorber layer thickness was lower for getting considerable absorption of the photons.

With the aim of fabrication of CuInSe_2 based solar cells, a modified technique of vacuum evaporation was developed in which CIS thin films were prepared using sequential elemental evaporation at moderately low substrate temperature. Indium, Selenium and Copper were evaporated at substrate temperature of 100°C , 50°C and room temperature respectively. Annealing this stacked layer at 400°C resulted in the formation of CuInSe_2 . Single layer thickness was $0.55\mu\text{m}$ which could be increased up to $0.85\mu\text{m}$ through double layer deposition. adopting similar steps. This technique was selected for further deposition.

The composition was widely varied to find suitability in device fabrication. For this Cu and Se were varied, one at a time, keeping the other concentration constant. Both p- and n-type films could be prepared using this technique. From the structural characterizations using XRD and Raman scattering, structure of CuInSe₂ prepared using this method, was identified as chalcopyrite which is universally accepted as the most suitable and favorable structure for solar cells. [In the earlier method, we could obtain only sphalerite structure]. The grain size varied from 35 nm to 63 nm in these samples. However this grain size was still lower than the reported values, obtained through other techniques of CuInSe₂ fabrication. This lead to increase in the number of grain boundaries which, in some cases, has beneficial effects on CuInSe₂ devices. Interestingly, the crystallinity of these samples were better than that prepared using chemical bath deposited Se and grain size was three times larger than that prepared using CBD Se.

The band gap varied from 0.93 to 0.99 eV with variation in elemental concentrations. The AFM analysis of the sample showed that the geometry of the sample changed from spherical to pyramidal on going from In-rich to Cu-rich. The resistivity varied in the range of 0.002 Ωcm to 7916 Ωcm, and hence, highly conductive and highly resistive samples could be selected for the device fabrication. The sample with resistivity of 0.08 Ωcm can be used as the conductive bottom layer and sample with a resistivity of 7916 Ωcm can be used as the resistive top layer for device fabrication. The photosensitivity of the highly resistive sample was 7.7. Highly stoichiometric film could be prepared without using ultra high vacuum which is still a major challenge for many researchers working in ternary chalcopyrites. Typical concentration of the stoichiometric sample was Cu: 24.92%, In: 24.98% and Se 50.10%. Hence this technique proved to be useful for the fabrication of highly stoichiometric CuInSe₂ thin films.

A trial for CIS/In₂S₃ was made with spray pyrolysed In₂S₃ as the n-type layer. Thickness and composition of In₂S₃ were varied in the films. We could achieve an observable shift in the I-V characteristics on illumination under AM1.5 radiation which can be improved with further studies.

Future outlook

CuInSe₂ has been recognized as an important alternative to Si for solar cells and commercialization of this technology is being done in different parts of the world. CdS, which is known to be a good counterpart to CuInSe₂ for solar cell fabrication, is very toxic and is banned in several countries. In₂S₃ is a promising material as a non-toxic buffer layer in the place of CdS. There is a lot of work yet to be done for the optimization of the spray procedure (for In₂S₃ deposition) to obtain a CuInSe₂/In₂S₃ junction. The initial experiments just show that, it can successfully replace CuInSe₂/CdS solar cells provided a systematic study is carried out on the spray parameters. The CuInSe₂ layer has been optimized here and with future work on In₂S₃ deposition, an efficient junction can be fabricated. Solar cell fabrication by the combination of these two techniques will make future thin film solar cells more economic and easy to fabricate.